nature photonics

Metamaterials with a twist

nature photonics

ORIGINAL RESEARCH TYPESET BY Techset Composition Ltd, www.techset.co.uk
PRINTED BY Wyndeham Grange, www.wyndeham.co.uk

MARCH 2009 VOL 3 ISSUE 3

nature photonics

COVER IMAGE

By changing the twist angle of unit cells in a metamaterial, Harald Giessen and co-workers have shown that it is possible to independently control, and thus optimize, the electronic and magnetic coupling in the material. Their so-called 'stereometamaterials' may have applications for creating ultra-thin elements for controlling polarization or creating sophisticated sensors.

Article p157; Interview p176

ON THE COVER

Terahertz optics
Solid-state phase modulator
Letter p148; News & Views p130

Signal processing
Analyser on a chip
Letter p139; News & Views p136

Subwavelength imaging
Observing colour centres
Letter p144; News & Views p133

EDITORIAL

CORRESPONDENCE

INTERVIEW

OUT OF THE LAB

RESEARCH HIGHLIGHTS

NEWS & VIEWS

LETTERS

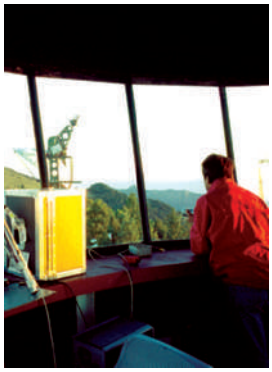

Could lasers ultimately give mankind control over when and where lightning strikes? This attractive scenario could become a reality once researchers have a laser that is powerful enough to create electrically conducting plasma channels with sufficient duration and length.
Interview p120

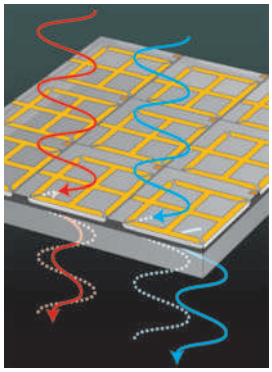

A solid-state phase modulator for terahertz waves has now been built by researchers in the United States. The attraction of the approach is that it is not only able to operate at much faster speeds than competing technologies but is also small, compatible with large-scale semiconductor fabrication technology and potentially suited to integration with electronics.
Letter p148; News & Views p130

ARTICLES

PRODUCT FOCUS

INTERVIEW

nature publishing group

Nature Photonics (ISSN 1749-4885) is published monthly by Nature Publishing Group (Porters South, 4 Crinan Street, London N1 9XW, UK). Editorial Office: Chiyoda Building, 5-6th Floor, 2-37 Ichigaya Tamachi, Shinjuku-ku, Tokyo, 162-0843, Japan. Telephone: +81 (0)3 3267 8751. Fax: +81 (0)3 3267 8754. Email: naturephoton@nature.com. North American Advertising: *Nature Photonics*, 75 Varick Street, 9th Floor, New York, NY, 10013-1917, US. Telephone: +1 212 726 9200. Fax: +1 212 696 9006. European Advertising: *Nature Photonics*, Porters South, 4 Crinan Street, London N1 9XW, UK. Telephone: +44 (0)20 7833 4000. Fax: +44 (0)20 7843 4596. Asia-Pacific Advertising: *Nature Photonics*, Chiyoda Building, 5-6th Floor, 2-37 Ichigaya Tamachi, Shinjuku-ku, Tokyo, 162-0843, Japan. Telephone: +81 (0)3 3267 8754. Fax: +81 (0)3 3267 8746. New subscriptions/renewals/changes of address/back issues and all other customer service questions should be addressed to - North America: *Nature Photonics*, Subscriptions Department, PO Box 5054, Brentwood, TN 37024-5054, USA. Outside North America: Subscriptions Department, Brunel Road, Basingstoke, Hants. RG21 6XS, UK. Telephone: +44 (0)1256 329242; Fax: +44 (0)1256 812358: Nature Asia-Pacific, Chiyoda Building, 5-6th Floor, 2-37 Ichigaya Tamachi, Shinjuku-ku, Tokyo, 162-0843, Japan. Telephone +81 (0)3 3267 8751. Annual subscription rates: US/Canada US$3060, Canada add 5% GST (institutional/corporate), US$152, Canada add 5% GST (individual making personal payment); UK/Rest of World (excluding Europe and Japan) £1570 (institutional/corporate), £78 (individual making personal payment); Europe €2430 (institutional/corporate), €121 (individual making personal payment). Back issues: US/Canada $45, Canada add 5% GST; Rest of World: surface mail US$43, air mail US$45. *Nature Photonics* (ISSN 1749-4885) is published monthly by Nature Publishing Group, c/o Mercury Airfreight International Ltd, 365 Blair Road, Avenel, NJ 07001, USA. Periodicals postage is paid at Rahway NJ. Postmaster: send address changes to *Nature Photonics*, c/o Mercury Airfreight International, 365 Blair Road, Avenel, NJ 07001, USA. Reprints: *Nature Photonics* Reprints Department, Porters South, 4 Crinan Street, London N1 9XW, UK. Subscription information is available at the *Nature Photonics* homepage at http://www.nature.com/naturephotonics. Postmaster: send address changes to *Nature Photonics* Subscriptions Department, Brunel Road, Basingstoke, Hants. RG21 6XS, UK or *Nature Photonics* Subscriptions Department PO Box 5054, Brentwood, TN 37024-5054, USA.

© 2009 Macmillan Publishers Limited. All rights reserved

Handle with care

Given that universities and companies have such different needs, is it appropriate for them to have partnerships, and if so, is some form of regulation required?

The level of interaction and cooperation that it is healthy for universities to have with industry is a somewhat controversial point, and an especially relevant one for photonics research. The topic was discussed in detail at the recent fifth annual meeting of the STS forum[1] in Kyoto, Japan, in October. Put simply, opinion tends to fall into two strongly opposing camps.

On the one side there are those who believe that universities should be dedicated to education and conducting fundamental, curiosity-driven research, and that this position should not be threatened or steered by commercial interests or pressure from industry. Fears are sometimes expressed that if industry-sponsored research is too dominant then universities run the danger of becoming nothing more than an outsourced company R&D lab and the companies will 'buy' excessive control of a university's research directions.

Such opinions hit the headlines when the energy company British Petroleum (BP) announced plans in February 2007 to fund, by means of a $500 million 10-year grant, a research centre called the "Energy Biosciences Institute"[2] at the University of California, Berkeley, in the United States.

The deal has now gone ahead but is still highly controversial. At the time it provoked uproar at UC Berkeley, resulting in student demonstrations and a campaign to block the deal[3] with cries of "We don't want the blood money," and "Stop the Trojan horse gift," regarding the perceived threats on the university's independence and reputation.

On the other side there are those who believe that close interaction between universities and industry is essential for giving a country a strong and thriving science and technology base, especially in developing nations. They comment that there are many benefits to gain from a close collaboration or partnership between the two parties. For example, they cite more rapid commercialization of technology, access to funding and equipment that the universities would not otherwise have, and the opportunity for companies to investigate high-risk or blue-sky research that they would not otherwise undertake.

Indeed, one of the strong messages to come from our interview with Gustav Kalbe, the head of the European Commission's Photonics Unit, in January[4] is that the Commission, through its 7th Framework Programme (FP7), is keen to foster and improve the relationship between small-to-medium enterprises (SMEs) and universities in Europe.

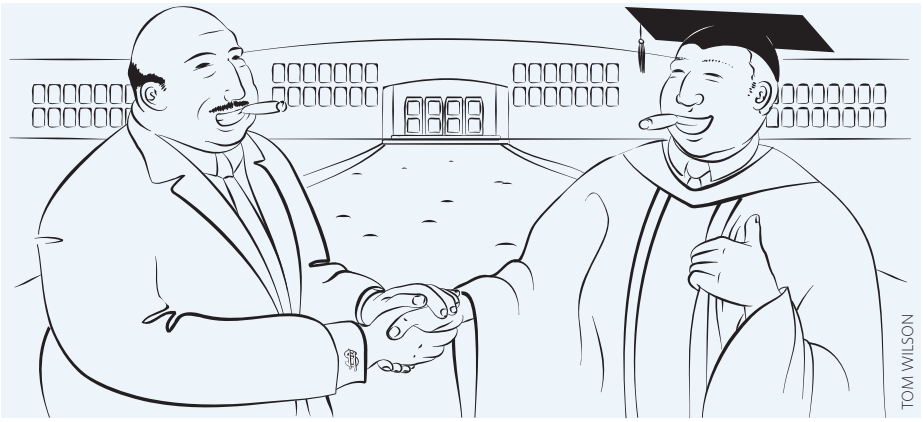

"Partnerships between universities and industry need to be handled carefully"

"We see the link between universities and SMEs as being vital for innovation," he stated in our January issue. "Considering the strong application and orientation of photonics, a project [within FP7] is more credible if it has an industrial or private company in the consortium."

Certainly, in photonics the level of interaction between industry and universities is already extremely active, given that so much of the research, even at a fundamental level, has such strong potential applications and opportunities for commercialization. Indeed, it is hard to find an optics group at a European university that does not already have some kind of strong connection to industry, through either a sponsored research programme or a cluster of spin-off or start-up companies.

Regardless of whether you feel that such collaborations are a threat to independence or a benefit to innovation, most would agree that before such partnerships are undertaken it is vital that important issues are discussed, such as how intellectual property and the publication of research findings will be handled. After all, each party needs to be satisfied that it will benefit.

And this perhaps is ultimately where the difficulty lies in making things work. At a fundamental level, universities and industry want different things and have different criteria for measuring success. Whereas a university is likely to be happy if the research results in a series of published papers, a company is more likely to want patents and a route towards commercialization. The problem is that there is often a conflict between these needs, especially in terms of how or whether results are disclosed.

The difficult task for governments and universities is to find the best model that somehow allows all the benefits of collaboration to flourish without jeopardizing some of the core values of a university or the attractiveness to companies.

The truth is that it is a difficult situation to handle, but we are certainly of the opinion that universities should not be pushed into a corner in terms of having targets for industry funding or being penalized for not having it. We also believe that it is important that universities continue to have independent funding that can be spent on research efforts with no obvious industrial applications. After all, we shouldn't forget that the laser itself has often been called an invention looking for an application, and such curiosity-driven research is vital for science. We welcome your comments on the matter. ❐

References

1. www.stsforum.org
2. http://www.energybiosciencesinstitute.org
3. http://stopbp-berkeley.org
4. Gevaux, D. *Nature Photon.* **3,** 2–3 (2009).

The long march of slow photonics

To the Editor — It is only in the past decade that the concept of slow wave propagation has penetrated the optical domain. Slow light has already been described by many researchers as a key to advances in optical signal processing, but in this new area many puzzles still have to be solved.

A first enigma concerns the most promising approach for generating slow light. In the arena of photonic devices, ring resonators (RRs) and photonic crystals (PhCs) are duelling to become the preferred scheme. However, as the rules of this match are far from obvious, we would like to clarify for readers the issues that must be taken into account when comparing the performance of slow-light devices.

Too often the group velocity reduction (that is, the slow-down factor) is assumed to be the most important criterion, but using this alone can drive non-specialists to misleading conclusions. A large slow-down factor is not synonymous with a large absolute delay. As far as linear devices (such as delay lines) are concerned, the only benefit of the slow down is a footprint reduction: in other words, the ability of a chip-scale waveguide device to replace a long length of optical fibre. Since the origin of research into slow light, this feature has inspired dreams of large-scale optical integration, but only recently have scientists started to consider the price to be paid. Pioneering experiments have since demonstrated that a high slow down imposes severe fabrication challenges, increases sensitivity to disorder[1], and makes tunability and device control more difficult. This general result suggests that slow-light devices should be evaluated by considering a variety of figures of merit, rather than simply the slow-down factor.

First of all, the quality of the signal being slowed must be preserved. Although chromatic dispersion was initially addressed as the theoretical Achilles heel of slow light, the maximum achievable delay in state-of-the-art integrated devices is limited mainly by loss[2]. A well-known rule says that the slower the light, the higher the propagation loss[3]. However, for a generic delay line (not only a slow-light one), the key figure of merit is not the loss per unit length but the fractional loss per bit, $L_f = c\alpha/n_g B_b$, c being the speed of light, α and n_g the attenuation and the group index of the structure, and B_b the pulse (bit) bandwidth. This relation does not depend on the device's dimensions and type, or on the slow-down factor. The guiding structure with the highest ratio n_g/α will prevail.

Furthermore, to be of practical use in many applications, slow-light schemes must allow the delay to be controlled continuously, easily and reliably. It has recently been demonstrated that these requirements are all fulfilled by a reconfigurable coupled resonator optical waveguide (CROW)[2]. In a CROW, the higher the storage efficiency η_s (how many bits are delayed by each resonator), the simpler is the reconfiguration. This allows a minimum number of resonators to control the delay. The unitary time delay induced by every resonator is simply $1/\pi B$, with B the CROW bandwidth: as a result, η_s depends only on the ratio B_b/B and not on either the resonator dimensions and type, or the slow-down factor.

On paper, a reconfigurable CROW may be realized by using either RRs or PhCs. At signal rates of tens of gigabits per second, the best results have been achieved in RR CROWs, and recently an optical delay line has been described[2] that is capable of delaying continuously an entire byte (eight bits), while preserving signal quality. The device, made of eight RRs in medium-index-contrast glass, introduces 0.5 dB attenuation per bit delay and can be easily controlled thanks to the high storage efficiency ($\eta_s = 1$ bit per RR) and its moderate slow-down factor (about 5). State-of-the-art PhC CROWs have larger bandwidths and smaller absolute delays, even in case of impressive slow-down factors (>100)[4], and seem to be more suitable for applications at higher bit-rates. For instance, Notomi *et al.*[4] recently used a PhC CROW with 60 cavities to delay a 12.5 Gbit s^{-1} data stream by 80 ps (1 bit delay) and, more effectively, a PhC CROW with 150 cavities to delay a 21-ps-long pulse by 125.3 ps (5.8 bits). Owing to the small storage efficiency of these structures ($\eta_s << 1$ bit per resonator), every pulse spreads over several tens of cavities, thus making the dynamical control of the delay still an open question. By following a different approach, Baba and co-workers have demonstrated that a chirped PhC waveguide can be used to tune the delay of 1.2-ps-long pulses over nearly seven pulse lengths[5]. This confirms the feeling that slow light in PhC structures is especially promising for ultra-wideband applications (terabits per second or more), where small absolute delays are of interest.

Manipulation of a single byte is a fundamental milestone in the long march of slow light towards the advanced processing of optical information[6]. Although RRs and PhCs have been walking along parallel roads, the hope is that this competition will soon converge into cooperation. From this point of view, silicon-on-insulator technology could offer a common platform for the integration of compact RRs[7] and PhC structures. Could PhCs embedded in RRs be the new frontier of slow photonics? ❐

References

1. Mookherjea, S., Park, J. S., Yang, S.-H. & Bandaru, P. R. Localization in silicon nanophotonic slow-light waveguides. *Nature Photon.* **2,** 90–93 (2008).
2. Melloni, A., Morichetti, F., Ferrari, C. & Martinelli, M. Continuously tunable 1 byte delay in coupled-resonator optical waveguides. *Opt. Lett.* **33,** 2389–2391 (2008).
3. Hughes, S., Ramunno, L., Young, J. F. & Sipe, J. E. Extrinsic optical scattering loss in photonic crystal waveguides: role of fabrication disorder and photon group velocity. *Phys. Rev. Lett.* **94,** 033903 (2005).
4. Notomi, M., Kuramochi, E. & Tanabe, T. Large-scale arrays of ultrahigh-Q coupled nanocavities. *Nature Photon.* **2,** 741–747 (2008).
5. Baba, T. Slow light in photonic crystals. *Nature Photon.* **2,** 465–473 (2008).
6. De La Rue, R. M. Optical delays: Slower for longer. *Nature Photon.* **2,** 715–716 (2007).
7. Xia, F., Sekaric, L. & Vlasov, Y. Ultracompact optical buffers on a silicon chip. *Nature Photon.* **1,** 65–71 (2006).

Andrea Melloni[1] and Francesco Morichetti[2]
[1]Politecnico di Milano, Department of Electronics and Information, Via Ponzio 34/5, Milano 20133, Italy
e-mail: melloni@elet.polimi.it
[2]POLICOM, Via G. Colombo, Milano 20133, Italy
e-mail: francesco.morichetti@polimi.it

Lightning control by lasers

Powerful lightning strikes pose a significant threat to buildings and people, but imagine if it were possible to control and direct them with a laser beam. *Nature Photonics* spoke to Jérôme Kasparian, a researcher from the University of Geneva and co-ordinator of the Teramobile project, about the idea.

The idea of firing an intense laser beam into a thundercloud to induce lightning and guide it back to a preferred location on the ground may sound far-fetched, but such a practice could one day be commonplace for protecting important buildings such as power plants or airports. In recent years, European scientists working on the Teramobile project (see Box 1) have demonstrated that intense, ultrashort laser pulses can ionize the air to create a virtual conductive path for guiding an electrical discharge along a straight line of several metres in a laboratory. The next stage is to build a laser 10 times as powerful, 'Teramobile 2', which, it is hoped, will allow a similar effect high in the sky. *Nature Photonics* spoke to Jérôme Kasparian about progress so far.

How did the idea for using lasers for controlling lightning come to mind?

This idea of triggering lightning using lasers is almost as old at the laser itself. Before long there were laser powers sufficient to ionize the air, and early on people realized that this would create a conducting path for electrical charge which could assist the triggering of lightning.

The first attempts took place as early as the 1970s in Russia and Japan, using huge CO_2 lasers, strongly focused, which generated a plasma spark but were not very successful. The problem was that the plasma was very localized and strongly absorbed the laser energy, thus preventing further propagation and the creation of a long ionization channel. There were a lot of laboratory experiments; in addition a Japanese team tried an experiment in the atmosphere in real conditions with three huge lasers focused near the top of a lightning tower. However, this was a huge system and not very effective.

What helped the idea to become more realistic?

What has happened between the early studies and now is the advent of CPA [chirped pulsed amplification] lasers, which allow the creation of ultrashort and high-power pulses beyond the terawatt level. They allow a self-guiding propagation regime known as filamentation. In this regime there is a dynamic balance between the nonlinear Kerr effect (self-focusing) and the effect of free electrons, which have a negative contribution on the refractive index and tend to defocus the beam. This gives a balance between the self-focusing and defocusing of the beam, resulting in self-guiding. With a sub-joule laser it is possible to make filaments tens or even hundreds of metres long with an electron density of 10^{15} or even 10^{16} electrons per cubic centimetre. Today, there are several groups working on similar ideas using different configurations, including the group of Pépin and Mercure in Quebec, the group of Diels at the University of New Mexico, and our Teramobile group, which is a European collaboration. Everyone is working on the idea of having a long ionized channel that can trigger and guide discharges. Several groups have been doing small-scale experiments over a few centimetres or few tens of centimetres, and then there have been very impressive experiments by the group in Quebec. We have also done some experiments in the lab using real filaments over a few metres at a few megavolts, as well as conducting field trials.

In the future, intense lasers may be able to provide control of electrical activity inside thunderclouds. Experiments in the laboratory and field trials have shown in principle that this is feasible, but more powerful lasers are needed to actually trigger and guide lightning.

My understanding is that the principle of using lasers for lightning control has been well demonstrated in the lab, but what about field trials?

It is not really straightforward going from the lab to the field. A big issue is with the lifetime of the plasma you generate. It is limited to the microsecond range. The discharge establishes at a speed of typically a few metres per microsecond, which means that after the discharge has propagated a few metres the track has disappeared. As a consequence, the pulse duration limits the effective length of the channel. We took our laser and went to the Langmuir Laboratory of New Mexico Tech, which is a permanent station for lightning studies. The visual observation did not give any results because we were at pretty high altitude at 3,000 metres and in the clouds at that time, and the camera could not see anything, but we could use the lightning

mapping array of Langmuir Laboratory, a network of radiofrequency detectors. Any discharge radiates a broad spectrum of radiofrequency radiation which can be detected. There were thirteen detectors spread over the region and we used the five closest to our lasers. These detectors detect precisely the time of arrival of each laser pulse and by triangulation you can reconstruct the three-dimensional position of each event. You have to remember that this detection technique detects not only the lightning strike but all of the electric activity in the cloud. What we did was to correlate the electric activity with the position of the laser beam and the time when the laser was pulsed with a precise repetition rate of 10 times per second. We were able to correlate an excess of electrical activity with the location and time of the laser pulses. These events correlated with the laser are quite faint events; they are not actually lightning strikes.

So what's next?

The main limitation to overcome is the limited lifetime of the plasma channel. We need to get an effective channel length of a few tens of metres to trigger the lightning. This length scale has been confirmed by experiments using rockets with conductive wire tails of various lengths. Such a short channel would also be better for us because we don't want to have the channel come all the way down to the laser from the point of view of the damage to the equipment or us — we are sitting underneath in the laser control room. To create plasma channels with a length of a few tens of metres, we need a more powerful laser. We are working on Teramobile 2, which will be a 10 times more powerful laser. However, it is not only a matter of brute force; we are also trying to be cleverer and not just shoot 10 times more power but organize this power in a train of 10 pulses, sharing the full power of the laser. The idea is that the first pulse would better establish the channel and the subsequent ones would maintain it. The burst mode will be something very innovative, as will a mobile laser providing 30 TW pulses. We will benefit from the fact that CPA technology has improved a lot in the past 10 years, so we can simply get more power from the current CPA technology. The technology is evolving towards smaller systems, especially with diode-pumped lasers. Most of the size of the systems is due to the pump lasers. From the energy point of view it is pretty inefficient. Eventually, I guess that there will be directly diode-pumped femtosecond systems. You can really imagine that in a few years the laser technology will allow us to have such a mobile terawatt laser in a van. It is hard to say exactly when Teramobile 2 will be ready, but I guess it is a matter of a few years.

Jérôme Kasparian, leader of the Teramobile team, adjusts the beam path of the Teramobile laser.

CNRS PHOTOTHÈQUE / CLAUDE DELAHAYE

Image of a high-voltage electrical discharge, that is, artificial lightning, over a distance of 3 m with (straight path) and without (erratic path) the assistance of a guiding laser filament.

How could you ensure that the discharge doesn't come directly back to the laser itself?

In fact this is not a big problem because you can control the distance from which the conducting channel begins. If you insert a grounded conductor in the laser path before it gets back to the laser, the discharge will go to this component. There are two variants. One is to use a grounded metallic mirror to reflect the beam and the discharge will go to the ground through the mirror; or you aim with the laser via the top of a classical lightning rod so that the discharge will go to the rod instead of following the conducting beam.

What are the benefits of using lasers for controlling lightning over schemes such as using rockets with conducting tail wires?

The rockets work pretty well — every second shot can be effective. However, you have a limited number of rockets and you cannot easily aim at the place in the clouds that you want to activate. With a laser, you can aim it and work it continuously so it would provide much more flexibility. Although a laser scheme might be too expensive for individual homes, for critical facilities such as power plants or airports it could be used to direct a laser strike away to a preferred location. Of course this is in the longer term.

INTERVIEW BY OLIVER GRAYDON

Box 1 | The Teramobile project

The Teramobile laser project was launched in 1999 and became operational in 2001. It is a very powerful mobile terawatt-class Ti:sapphire laser which uses chirped pulse amplification to generate intense ultrashort pulses (see specifications below) for atmospheric studies. The laser comprises a Ti:sapphire oscillator and a Nd:YAG pumped Ti:sapphire amplification chain made of a regenerative amplifier and two four-pass amplifiers. It concentrates the state-of-the-art laser technology in a 20-foot standard freight container, allowing field measurement campaigns. It is an international project initiated jointly by a French–German collaboration of CNRS (France) and DFG (Germany). Switzerland has now joined the consortium. It is now funded by ANR and the Swiss FNS and involves five research institutes in Berlin, Dresden, Lyon, Palaiseau and Geneva. The laser system itself was built by Thales Laser of France. The Teramobile laser is used for investigating nonlinear propagation of femtosecond-terawatt laser pulses over long distances in the atmosphere, and their applications to atmospheric research. This includes Lidar remote sensing of atmospheric pollutants as well as lightning protection and triggering by a mobile terawatt laser system.

Teramobile specifications

Centre wavelength: 800 nm
Pulse energy: 350 mJ
Peak power: 5 TW
Pulse duration: 70 fs to 2 ps
Repetition rate: 10 Hz
Output beam diameter: 50 mm
Size: 3.5 m × 2.2 m
Weight: 10 tonnes

Sounding out photons

Photoacoustic imaging, using laser light to stimulate the emission of ultrasonic waves from tissue inside the human body, potentially offers a route to far deeper imaging than possible with conventional optical techniques, reports *Duncan Graham-Rowe.*

Bouncing light off biological tissue has become a mainstay of modern medical imaging and microscopy. But most existing techniques are limited in their ability to penetrate the body by more than just a few millimetres. However, a technique called photoacoustics, a marriage of optical and ultrasonic technologies, could be about to change the situation.

The idea behind photoacoustics, which is also known as optoacoustics, is simple: use light to stimulate interior tissue so that it gives off acoustic waves in the ultrasonic range. These waves can be then be detected using wide-band ultrasonic transducers and used to build up high-resolution images of subsurface tissue structure (Fig. 1).

"We want to reach what's called super depth," says Lihong Wang, at Washington University in St Louis, Missouri, USA, and one of the most active researchers in the field of photoacoustics. The hope, he says, is that by using photoacoustics clinicians will be able to carry out safe, high-resolution three-dimensional imaging and microscopy at depths of centimetres rather than millimetres, and without the use of potentially harmful ionizing radiation, such as X-rays.

In addition, photoacoustics should open up new opportunities for diagnosing, monitoring and treating diseases. For example, it could help to guide biopsy needles deep beneath the skin, assist endoscopic techniques for diagnosing gastrointestinal cancer, measure oxygen saturation levels in haemoglobin and study subsurface vascular and lymph nodes to visualize and quantify malignant tumours. It can even be used to probe the brain and to monitor gene expression.

Although the latest photoacoustic apparatus make use of state-of-the-art laser technology, the first examples of using light to stimulate acoustic waves date back to the nineteenth century. As far back as 1880, Alexander Graham Bell discovered that it was possible to make a thin disk emit sound when exposed to a beam of pulsing sunlight. Initially Bell sought to use the effect as a means of communication, converting sound into the light, sending it through free space and then converting it back into sound again. "He called it the photophone," says Wang. Needless to say, his other idea, the telephone, proved a more popular invention, not least because it didn't have issues with line-of-sight.

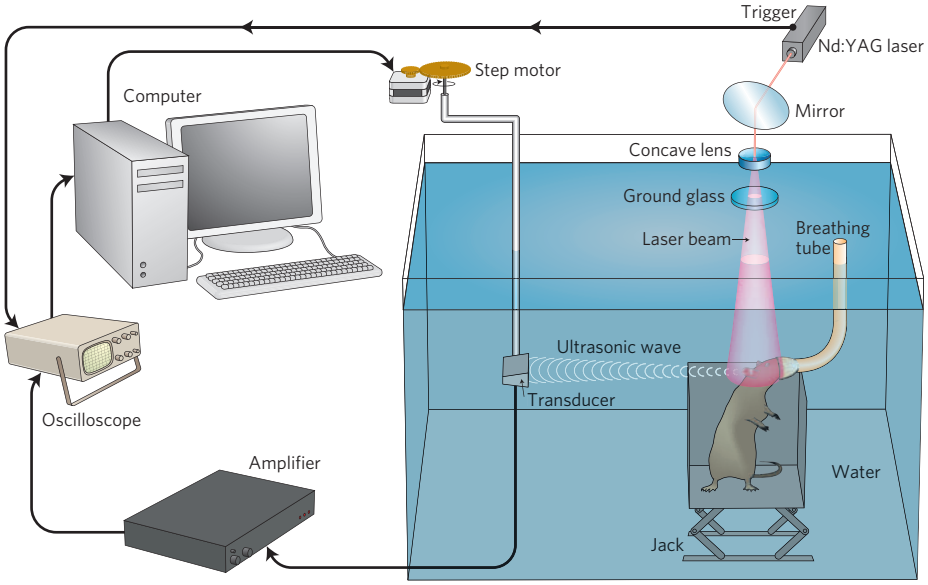

Figure 1 | Schematic of a photoacoustic system for imaging the brain of small animals. Systems can also be equipped with a microscope to allow imaging of smaller target areas. The sample is immersed in water to allow high-quality collection of the ultrasonic acoustic waves. Adapted from ref. 1. © 2003 NPG.

After that, photoacoustics was largely ignored until the 1970s when the development and availability of lasers triggered an interest in its use for non-destructive testing. But it wasn't until the late 1980s that its medical applications started to become apparent. Initially interested in the effects of laser absorption on tissue, Alexander Oraevsky, then at the USSR Academy of Sciences, Moscow, started to look at how the interaction could be used for imaging — a technique he dubbed optoacoustics.

His initial experiments showed that cells produced pulses of ultrasound in response to the pulses of laser light. Oraevsky left Moscow in 1991 to continue his work at the University of Texas, and has since become vice president of research and development with Fairway Medical Technologies, in Houston, Texas.

Fairway, with its commercialization partner, Seno Medical Instruments of San Antonio, Texas, is one of a handful of companies now developing the technology for real-life applications.

Oraevsky explains that as light passes through the tissue certain wavelengths are preferentially absorbed by cells. The absorbed energy causes a very small amount of heating that makes the cell swell. This so-called thermoelastic expansion produces acoustic pressure waves that can then be detected by placing ultrasonic transducers on the skin.

But to get really useful high-resolution imagery requires lasers capable of emitting nanosecond pulses, says Oraevsky. "You have to use a short enough pulse to ensure that the energy is delivered before it can escape as pressure," he says. Wang agrees. Nanosecond pulsing, along with lasers capable of high spectral purity, is really necessary if you want to obtain very high spatial resolution, says Wang.

What makes photoacoustics different from other three-dimensional imaging techniques — such as optical coherence

Table 1 | Comparison of various forms of medical imaging techniques

Technique	Contrast mechanism	Spatial resolution	Maximum depth penetration
Confocal microscopy	Scatter, fluorescence	~0.2 μm	~0.5 mm
Two-photon microscopy	Fluorescence	~0.2 μm	~0.5 mm
Optical coherence tomography	Scatter, polarization	~10 μm	~1 mm
Magnetic resonance imaging	Proton density	~1 mm	~200 mm
X-ray computed tomography	Electron density	~0.1 mm	~200 mm
Ultrasound	Scatter	~1 mm	~100 mm
Photoacoustic microscopy	Absorption	~2–200 μm	~1–30 mm
Photoacoustic computed tomography	Absorption	~0.8 mm	~50 mm

DATA COURTESY OF LIHONG WANG

tomography (OCT), two-photon microscopy and confocal microscopy (see Table 1) — is that it relies on light being absorbed rather scattered. One of the reasons that these other techniques are so limited in how deep they can delve is that back-scattered light is diffused by the tissue, making it difficult to detect in any meaningful way.

"They rely upon ballistic photonics," says Wang. But typically a photon can only pass through about 0.1 millimetres of tissue before it will be scattered, making it difficult to go much deeper than a millimetre, he says.

The problem is not the source laser, says Wang. If the wavelength is carefully chosen, the laser light has no problem penetrating deep into the tissue; the challenge is getting a signal out without scattering. But for ultrasound waves this is not a problem, he says. "When we convert light into sound we get minimal scattering, so we can penetrate deeper," says Wang. "The deepest we have demonstrated is 5 centimetres, but some colleagues claim to have gone deeper, up to 7 centimetres."

Besides going deeper, it is also much safer than other forms of imaging such as X-rays because it doesn't involve using ionizing radiation, says Wang. And only a minimal and quite safe amount of heating of cells is necessary. For every millidegree Celsius rise in temperature you get around 8 millibars of pressure, he says. Ultrasonic transducers are sensitive down to about 1 millibar or better, so by raising the temperature of tissue by about 100 millidegrees Celsius you can receive a strong signal.

For imaging applications, detection is usually carried out using an array of wide-band ultrasonic transducers. The process of pinpointing the source (origin) of the acoustic wavefronts is performed by measuring the travel time of the ultrasonic waves at multiple positions and then using triangulation.

"But we don't have a single point source, we have a continuous volumetric source, because there is more than one point absorbing the light," says Wang. So within the array are sets of transducers capable of detecting different ranges of acoustic wavelengths. Each transducer typically measures just a few millimetres in size, and 128 or 256 transducers are typically used in total.

The type of tissue molecules from which the acoustic signals can be detected depends strongly on the wavelength of the source laser, so for this reason tunable lasers are commonly used. Different tissue types will absorb different wavelengths of light, making them act like endogenous (natural) contrast agents, says Michael Thornton, Chief Operating Officer of Endra. The firm was set up in 2007 by Boston-based life science research technology company Pure Venture to develop photoacoustic imaging technology and is in the process of moving to Ann Arbor, in Michigan.

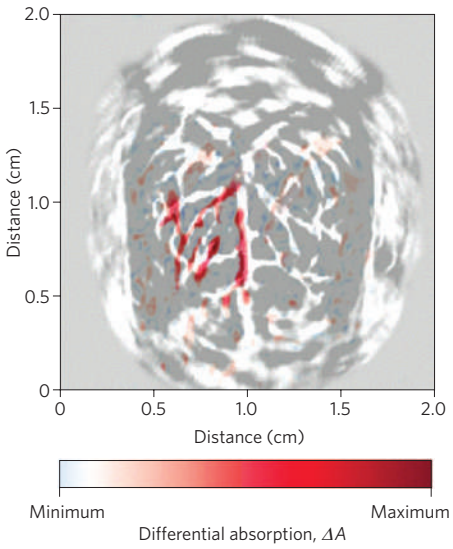

Figure 2 | *In vivo* functional photoacoustic image of the cerebral haemodynamic changes (shown in colour) in response to whisker stimulations acquired non-invasively in a small animal, where the morphology of blood vessels is shown in grey scale. Reproduced with permission from ref. 1. © 2003 NPG.

Examples of a natural contrast agent are oxygenated and deoxygenated haemoglobin, says Wang. By using photoacoustic tomography to target these chromophores it is possible to quantify and image oxygen saturation of haemoglobin and its levels of concentration (Fig. 2). This is important because it enables a high-contrast picture containing functional information to be built up showing, for example, the formation of new blood vessels (Fig. 3) and metabolic levels. "These two physical parameters are really important because they are hallmarks for cancer," says Wang.

Because blood is so good at absorbing certain wavelengths it produces correspondingly strong acoustic waves, says Oraevsky. As a result the optical contrast between normal and cancerous tissue (Fig. 4) is substantially greater than with conventional imaging methods, he says.

Indeed, Oraevsky's team have been able to image whole mouse bodies to study blood flow and tumours. They have also performed preliminary clinical work to assess the technology's ability to distinguish between malignant and benign breast cancers, with resolutions down to about 500 micrometres. The kind of laser used depends very much upon what you are imaging, he says. To image breast tissue a 757-nm Alexandrite laser is used with 50-ns pulses, whereas to image the small blood vessels of mice a 1,064-nm Nd:YAG laser emitting 10-ns pulses is needed, he says. Because these pulses are repeated at a rate of 10 a second it is possible to get real-time images that can be played like a movie, says Oraevsky.

Another application being explored for photoacoustic imaging is to detect contrast

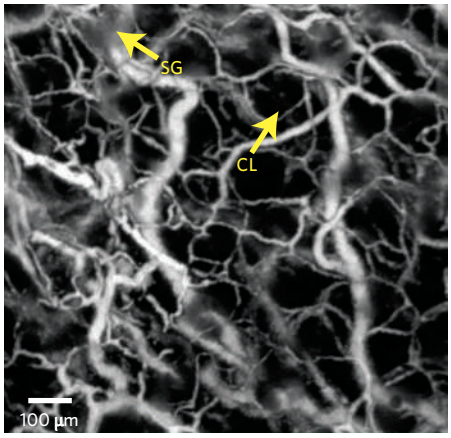

Figure 3 | *In vivo* photoacoustic image of blood vessels including single capillaries in a small animal, acquired non-invasively with an optical-resolution photoacoustic microscope. CL: capillary; SG: sebaceous gland. Reproduced with permission from ref. 2. © 2008 OSA.

agents that are designed to target specific biomarkers, such as for cancer cells. This is one area that Endra is looking at as a means of developing new pharmaceuticals, says Thornton.

Similarly VisualSonics, a leading ultrasonic imaging company based in Toronto, Canada, has been evaluating the technology for detecting cancer targeting contrast agents, says Stuart Foster, founder and Chief Scientific Officer of the company, and professor of medical biophysics at the University of Toronto. Ultrasound is already being used to detect such agents, but there are limitations, he says. Normally these agents are confined to the blood vessels. But VisualSonics is now looking at using the high-contrast properties of photoacoustics to target gold nanorod agents which have the potential to pass through the epithelium of the vessels and bind to specific targets on cells. "We're using this optical approach to get a bit further into the tissue," he says. "It's a natural progression for us, and a way for us to report on a much larger range of molecules."

Indeed, according to Wang a variant of this approach even has great potential to monitor the genetic activity of cells. "We can image gene expression for reporter genes," he says.

But despite its merits photoacoustics is no magic bullet, says David Steinberg, Endra's CEO. Although it is possible to do whole body imaging of mice, for humans this is a bit more challenging. "As the light propagates deeper you get less and less light, and so less pressure," says Wang. Also, the lungs and airways can play havoc with the ultrasound, he says. "Air cavities will give you almost insurmountable problems."

Figure 4 | *In vivo* photoacoustic image of a melanoma and the surrounding blood vessels in a small animal acquired non-invasively with a 50-MHz photoacoustic microscope. Reproduced with permission from ref. 3. © 2007 NPG.

Bone presents similar difficulties, but despite this there is great interest in using photoacoustics for neuro-imaging, says Foster. "The light will pass through the skull," he says. The problem is that the ultrasound becomes aberrated as it passes back out. This is not an insurmountable problem, says Wang, who is now working on a technique to 'de-aberrate' these signals by modelling the skull's properties.

Currently there are no products on the market yet, although Endra plans to make its platform commercially available for clinical research laboratories possibly later this year. But photoacoustic imaging is potentially so cheap and easy to use that eventually it is likely to find its way into clinics.

"It's not a proven technology but it's a technology with phenomenal potential, and that's why it needs to be explored," concludes Foster. ❐

Duncan Graham-Rowe is a freelance science and technology journalist based in Brighton, UK. e-mail: duncangr@gmail.com

References

1. Wang, X. D. *et al. Nature Biotechnol.* **21,** 803–806 (2003).
2. Maslov, K., Zhang, H. F., Hu, S. & Wang, L. V. *Opt. Lett.* **33,** 929–931 (2008).
3. Zhang, H. F., Maslov, K., Stoica, G. & Wang, L. V. *Nature Biotechnol.* **24,** 848–851 (2006).

OPTICAL SENSING

Brain waves

Nano Lett. ASAP (2009) doi: 10.1021/nl801891q

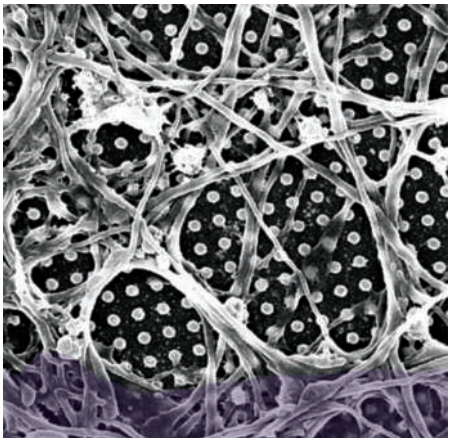

Researchers have successfully used plasmonic gold nanoparticles to detect brain cell activity. The work, performed by Jiayi Zhang, Tolga Atay and Arto Nurmikko of Brown University, could point the way towards reading local brain waves on a submicrometre scale.

Neuroscientists typically record brain activity using electrodes that are inserted into the cellular tissue, a method that is invasive and electronically noisy. Non-invasive approaches have been tried, but they usually involve dyes and staining techniques that are toxic or have other drawbacks. Localized surface plasmons (LSPs), which are confined to subwavelength-size metal nanoparticles, offer a potential way forward because they can perform non-invasive optical sensing on the micro- and nanoscale.

Zhang and colleagues started by growing mammalian hippocampal brain cells on a gold nanoparticle template. They then used the surface plasmon resonance of the nanoparticle array as a marker of brain activity: when a neuron fires and switches its potential, the resonance wavelength of the nanoparticle shifts, and neural activity can be mapped in real time.

Although previous research has used LSP resonances to detect nerve signals in rats, this is the first time that they have been used to detect the firing of a single brain cell. The question of how to deliver plasmonic nanoparticles into deep brain tissue remains unanswered, but could possibly involve colloidal nanoparticles or optical fibre implantation into the brain.

LASERS

High-performance QCLs

Appl. Phys. Lett. **94,** 011103 (2009)

Tremendous progress has been made in improving the performance of quantum cascade lasers (QCLs) in recent years. They now emit light in the entire mid-infrared range (3–25 μm), and are used in sensing, military applications and free-space communications. Qi Jie Wang and colleagues have unveiled a new high-performance QCL that is based on a three-phonon resonance design.

For optimal performance the QCL must maintain a large population inversion, which requires the efficient injection of electrons into the upper laser level and fast depletion of the lower level. Wang *et al.* focus on improving the depletion scheme using an effect known as longitudinal optical phonon scattering, which is the fastest intersubband relaxation process available. It ensures fast depletion and helps to maintain the required population inversion.

In their three-phonon scheme, four energy states in the laser's active region are separated from one another by the energy of an optical phonon. With so many energy levels, depletion is improved and thermal backfilling of the electrons from the active region ground state is greatly decreased. The resulting QCL emits light at 9 μm with a peak output power of 1.2 W. The authors also produce a smaller heterostructure device that offers continuous-wave power as high as 65 mW from a single facet at 300 K.

IMAGING

Acoustic world

Appl. Phys. Lett. **93,** 261101 (2008)

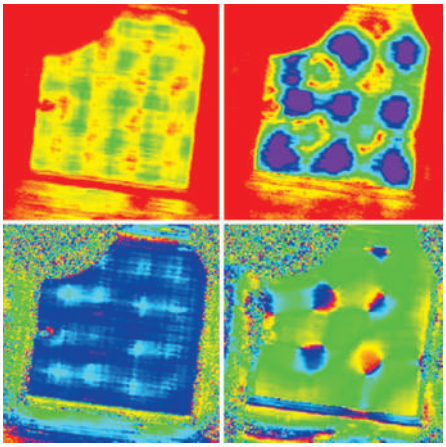

Bulk acoustic wave (BAW) and surface acoustic wave (SAW) piezoelectric resonators are used in the communications industry to filter electromagnetic waves with frequencies ranging from 1 to 10 GHz. Thanks to their high *Q* factors (over 1,000), small volumes and relatively low price tags, they have the potential to be extremely useful in modern wireless communication systems. Compared with SAW resonators, BAW resonators are easier to couple to standard integrated circuit technology, handle power better and are generally more stable with temperature fluctuations.

The bandwidth of these devices depends on the acoustic loss, and optical imaging has proved invaluable for monitoring resonator operation and acoustic wave leakage. Takashi Fujikura and colleagues have now used an ultrafast interferometric technique to image acoustic waves coming from a thin-film BAW resonator in real time.

They use ultrashort optical pulses (with a near-infrared wavelength of 830 nm) both to generate synchronized electrical pulses that excite the BAW resonator, and to detect the resulting surface vibrations. The technique can successfully image the amplitude and phase of waves with

OPTICAL MICROSCOPY

To new depths

Proc. Natl Acad. Sci. **105,** 20221–20226 (2009)

Three-dimensional biological imaging is the focus of new research from Alipasha Vaziri and colleagues in the United States. They manage to image protein distributions in cells with a resolution better than 50 nm at multiple imaging planes up to 10 μm deep in a sample.

Most of the microscopy techniques currently available are limited to imaging depths that are a fraction of the optical wavelength. Biologists would like to study whole cells or organelles that typically appear up to 15 μm deep into the cell. Vaziri *et al.* combine a technique known as photoactivated localization microscopy (PALM) — whereby emissions from molecules are used to discriminate signal from background — with a method known as temporal focusing, which can be used to selectively excite a thin layer of molecules in a biological sample.

The combination of these two methods is used to excite and image a thin layer of fluorescent proteins several micrometres deep in a cell sample. The generated images, taken from mitochondrially labelled cells and the membranes of living *Drosophila* cells, show super-resolution over an axial range of about 10 μm, overcoming the depth limitation of more conventional techniques.

frequencies up to 2.2 GHz and measure both longitudinal and surface acoustic modes. By improving the response of the photodetector used, higher-frequency BAW devices could be probed, potentially up to >100 GHz.

QUANTUM OPTICS

Entanglement purification

Science **23,** 483 (2009)

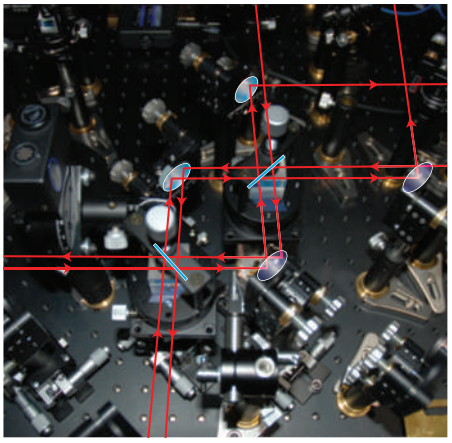

HOKKAIDO UNIVERSITY

Distinguishing and sorting photons that possess desired features from those that do not is an important task in many optical applications. One example is the polarization filter that passes a photon only if it has a certain polarization.

For quantum information science, arguably the most important feature is the entanglement — a quantum mechanical coupling — of multiple photon states. If two states, such as the polarization of two photons, are entangled, it is not possible to describe one state without its counterpart. This feature is important for quantum information processing.

A Japanese–UK collaboration has now realized a non-destructive entanglement filter that transmits entangled photon pairs only if they share the same polarization. The two possible transmitted photon states are automatically sorted to separate output ports.

The entanglement filter is likely to be a key element for controlling multiphoton quantum states with a host of foreseeable applications in quantum communication and computing.

The team creates the photon pairs by passing pulses through a beta-barium borate crystal and filters them with an optical circuit made from an ultra-stable Sagnac interferometer featuring partially polarizing beam splitters. The sorting relies on the fact that photon pairs of different polarization combinations experience distinct path lengths. The measurement of an ancillary photon pair ensures that non-destructive successful filtering of a signal pair took place.

SOLAR TECHNOLOGY

Designer modules

Appl. Phys. Lett. **94,** 013305 (2009)

Scientists working for Sharp Corporation in Japan have produced a dye-sensitized solar cell (DSC) module with a record-breaking efficiency of 8.2%. Their work comes on the heels of other studies that have endeavoured to boost DSC sizes while maintaining reasonable efficiencies.

Liyuan Han and co-workers studied a DSC module made up of several rectangular cells connected in series. Because neighbouring cells are processed in reverse, the module is known as a W-contact module. By eliminating the amount of interconnection between neighbouring cells, the module can offer a larger active area — 25.5 cm^2 in this case. In an effort to increase the size of DSCs in recent years, researchers have tried connecting many single cells in series in various configurations.

The W-contact design increases the active area and produces neighbouring cells of alternate bias. However, the challenge is to maintain a uniform short-circuit current density across the entire module. Han *et al.* achieve this by optimizing the composition of the platinum counterelectrode, the electrolyte, the thickness of the titanium dioxide film used, and the uniformity of the unit cells. The result is the highest recorded module efficiency of 8.2%. With an active area of 85%, this equates to a 9.3% active area efficiency.

NONLINEAR OPTICS

Discrete phase jump

Phys. Rev. Lett. **102,** 013902 (2008)

The ability to change the phase of one light beam using another by means of a nonlinear interaction (cross-phase modulation) between the two has applications in fields such as quantum information, high-precision sensors and low-power optical switching. Schemes for cross-phase modulation, including electromagnetically induced transparency, typically allow the phase of the signal to be varied between 0 and 2π.

Ryan Camacho and US collaborators have now demonstrated all-optical modulation in which the phase change is either zero or π radians, with no possibility of the values in between. The discrete phase-jump scheme relies on an interferometer, in which a nonlinear interaction between control (852 nm wavelength) and signal (895 nm wavelength) fields is mediated by a 10-cm-long cell of warm (70 °C) caesium vapour. A solenoid in the gas chamber applies a magnetic field allowing magneto-optical Faraday rotation of the polarization.

The scheme works by flipping the phase to either 0 or π, depending on a threshold value for the phase of the signal that is significantly smaller than π. The discrete phase modulation may open new avenues for effective amplification and sensing of very weak interactions.

NANOPLASMONICS

Remote control genes

Nano Lett. ASAP (2009) doi: 10.1021/nl802689k

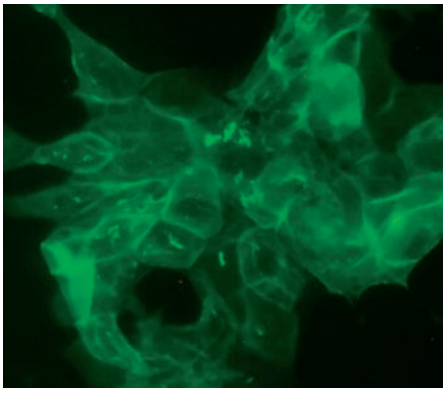

Scientists based in the United States have come up with a new way of controlling gene interference in living cells: using light-absorbing nanoparticles and an optical remote control. Precise control of gene interference is important for studying cellular signalling pathways, quantitative cell biology and molecular biology.

The team's optical switches consist of double-stranded oligonucleotides attached to gold nanoparticles (GNPs), which are tuned to absorb in the near-infrared wavelength range, where cells are essentially transparent and undamaged by light. At specific times and cellular locations, a near-infrared laser is used to activate the GNP remotely (through a photothermal heating mechanism), which then releases about 250 molecules of oligonucleotides. These nucleotides bind to mRNA within the cell and silence the gene of interest at the translational step. This halts protein translation and expression in the cell.

Compared with conventional gene interference methods, the technique ushered in by Lee *et al.* has the advantage of offering both spatial and temporal control, minimal photodamage to cells, and the ability to couple the optical transmission frequency selectively to different nanoscale transmitters.

LIGHT-EMITTING DIODES

Photonic crystal efficiency boost

LEDs are receiving great interest as candidates for next-generation lighting because they promise to reduce energy consumption enormously. However, to be a feasible solution their quantum efficiency needs to improve. Now, it seems that the incorporation of photonic crystals may be an answer.

Susumu Noda and Masayuki Fujita

LEDs directly convert electric energy into light, and over the years their efficiency has rapidly increased to become comparable to that of fluorescent lamps[1]. But to harness their full potential for next-generation lighting, further increases in their quantum efficiency are required. The efficiency of LEDs is determined by two factors: the internal quantum efficiency, which is defined as the ratio of the number of injected electron–hole pairs to that of generated photons; and the light-extraction efficiency, which is defined as the ratio of the number of generated photons to the number extracted from the device. For ultimate LED efficiency (close to 100%), enhancement of the light-extraction efficiency is especially important. This is because most of the generated photons remain inside an LED owing to total internal reflection at its surface, arising because of the large refractive index difference between the semiconductor and air (Fig. 1a). Eventually, the photons confined inside the LED are absorbed by the electrode or other components and lost, degrading the device efficiency.

On page 163 of this issue, Wierer *et al.*[2] successfully demonstrate a significant increase in light-extraction efficiency by introducing photonic crystals into a GaN-based LED, as shown in Fig. 1b. Photonic crystals, nanostructures for light with a periodic refractive index distribution, give control over the direction of light propagation (by multi-directional Bragg diffraction effect) and can even inhibit undesired light emission by the photonic bandgap effect[3,4].

Wierer *et al.* use a two-dimensional (2D) photonic crystal and harness its control over light propagation to increase the light-extraction efficiency of an LED. Put simply, modification of the light-propagation direction can break the total internal reflection condition at the surface of the LED, helping more photons to leave the device and thus increasing its light-extraction efficiency.

However, if there are many optical modes inside the LED, the beneficial effects of the photonic crystal vary too much among these modes to have a net benefit for the entire device. As shown in Fig. 1a, a large number of optical modes exist in a typical LED. Each mode has a different electromagnetic field distribution, propagation direction and frequency. The photonic crystal's complicated modification of the light-propagation direction changes for individual mode parameters, so that the optimal structure of the photonic crystal differs from mode to mode. Therefore, the optimization of a photonic crystal structure is generally very difficult, limiting the ability of the photonic crystal to increase the overall light-extraction efficiency.

This fact strongly indicates that reducing the number of optical modes inside an LED is essential to making better use of photonic crystals. In the present work, Wierer *et al.* have reduced the device thickness down to ~700 nm by using a laser-liftoff technique[2] to reduce the number of optical modes. They have successfully reduced the number of optical modes in an LED to just seven, which is few enough to enhance the effect of the photonic crystal. In addition, Wierer *et al.* tailored the electrode underneath to avoid optical absorption as much as possible[2]. They used silver as an electrode, and optimized the distance between the emitting layer and the electrode to suppress the absorbing surface plasmon localized at the surface of the electrode. As a result, they have achieved a light-extraction efficiency as high as 73%, a record value for any unencapsulated LED in which the emission is directly extracted[2].

Although Wierer *et al.* used the photonic crystal to control the light propagation direction[2], using photonic crystals to inhibit undesired light emission may help to increase the light-extraction efficiency still further[4,5]. This is the ideal goal of using photonic crystals — simultaneous inhibition

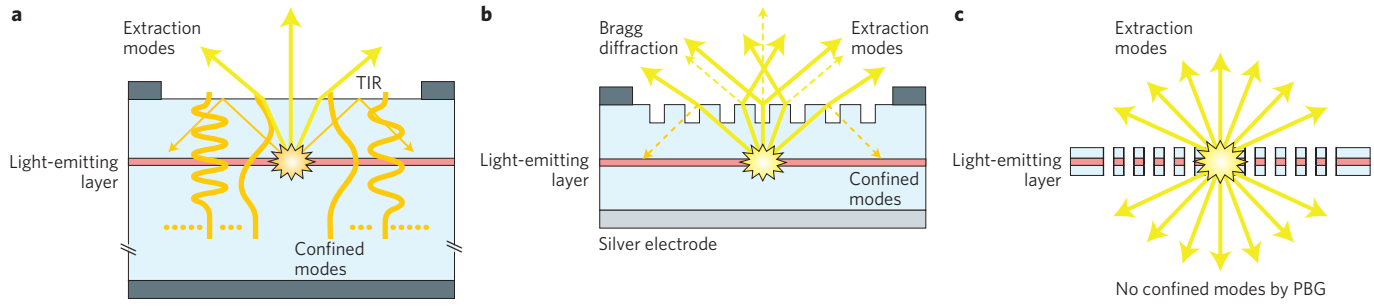

Figure 1 | Cross-sectional schematic of LED structures. The optical modes confined inside and the light-extraction method are shown here. **a**, Conventional planar-surface structure. Most of the light is confined inside by total internal reflection (TIR) phenomena at the surface. **b**, Light-propagation control structure. The light extraction is improved by control of the light-propagation direction (or multi-directional Bragg diffraction effect) with the photonic crystal, although some confined modes still exist. The photonic crystal effect is increased by the reduction in the number of confined modes through the introduction of a thin-film structure and a silver electrode. **c**, Photonic bandgap (PBG) structure. Confined modes are inhibited. This is an ideal structure for light extraction because all light from the light-emitting layer couples to extraction modes.

and redistribution of light emission by the photonic bandgap[4,5] effect.

Imagine an LED structure that features a 2D complete photonic crystal as shown in Fig. 1c. Light emission in the in-plane direction can be inhibited, and thus the injected electron–hole pairs cannot be used for emission in the in-plane direction. As a result, most of the injected electron–hole pairs accumulate and are finally used to emit light only in the direction normal to the photonic crystal, where the photonic bandgap effect is not present. Thus, the injected carriers are used most effectively to emit light out of the device, leading to a significant increase in the light-extraction efficiency[4,5], ideally approaching 100%. In this scheme, the most important issue is how to suppress the non-radiative surface recombination process at the air holes of the photonic crystals, which degrades the internal quantum efficiency. But this problem could be overcome by the introduction of quantum nanostructures, or quantum dots[4], where three-dimensional localization of the electron–hole pairs occurs and the non-radiative process could be significantly reduced[4].

Photonic crystals can be also applied to increase the light-extraction efficiency in various other material systems, including silicon[6] and organic materials[7]. Finally, it should be pointed out that there are various competitive methods for improving light-extraction efficiency in LEDs, including the introduction of surface roughness[8], the use of a patterned substrate[9] and chip shaping[10]. This competition between various technologies will continue until the realization of ultimate efficiency. ❐

Susumu Noda and Masayuki Fujita are in the Department of Electronic Science and Engineering, Kyoto University, Katsura, Nishikyo-ku, Kyoto 615-8510, Japan.
e-mail: snoda@kuee.kyoto-u.ac.jp

References

1. Narumawa, Y. *et al. Jpn. J. Appl. Phys.* **46,** L963–L965 (2007).
2. Wierer, J. J., David, A. & Megens, M. M. *Nature Photon.* **3,** 163–169 (2009).
3. Yablonovitch, E. *Phys. Rev. Lett.* **58,** 2059–2062 (1987).
4. Noda, S., Fujita, M. & Asano, T. *Nature Photon.* **1,** 449–458 (2007).
5. Fujita, M., Takahashi, S., Tanaka, Y., Asano, T. & Noda, S. *Science* **308,** 1296–1298 (2005).
6. Fujita, M., Tanaka, Y. & Noda, S. *IEEE J. Sel. Top. Quant. Electron.* **14,** 1090–1097 (2008).
7. Fujita, M. *et al. Jpn. J. Appl. Phys.* **44,** 3669–3677 (2005).
8. Krames, M. R. *et al. J. Display Tech.* **3,** 160–175 (2007).
9. Narumawa, Y. *et al. Jpn. J. Appl. Phys.* **45,** L1048–L1086 (2006).
10. Krames, M. R. *et al. Appl. Phys. Lett.* **75,** 2365–2367 (1999).

TERAHERTZ OPTICS

Terahertz phase modulator

Electrically tunable metamaterials make it possible to create the first solid-state phase modulator operating at terahertz frequencies.

Carsten Rockstuhl and Weili Zhang

The ability to tailor the flow of light in a manner beyond what is possible with naturally occurring materials is a promise that can be fulfilled with artificial metamaterials[1]. Such artificially structured materials are usually composed of periodically arranged unit cells that allow the creation of a medium with customized electromagnetic properties[2]. In particular, strong dispersion of the medium's effective permittivity, effective permeability, or both, is possible if the unit cells are sculptured to possess a resonant electric and/or magnetic response to the incident electromagnetic radiation.

The development of new unit cells that serve a well-defined purpose can be seen as the prototypical problem in metamaterial design. Furthermore, a mechanism to tune a metamaterial's properties is strongly desired. In particular, the creation of a material for which both permittivity and permeability are dispersive might yield unprecedented applications. An important step along this path has now been taken by a collaboration of researchers working in Los Alamos, Boston and Albuquerque[3]. On page 148 of this issue, Chen and co-workers report the development of a metamaterial phase modulator with an operating frequency of 0.89 THz.

Original proposals for applications relying on metamaterials, such as the perfect lens[4] or the invisibility cloak[5], have arguably attracted the largest research interest in the past, as their operation contradicts the expectations of our common sense regarding how light propagates. But these concepts have somewhat overshadowed metamaterial-based ideas for other functional devices that may be far closer to practical realization. The promise of metamaterials that address specific applications, such as the development of perfect absorbers[6] or anti-reflection structures[7], might be less spectacular at first glance; however, they are far more needed from a practical and technological point of view. This viewpoint especially holds true for metamaterials operating at terahertz frequencies. Terahertz radiation (0.1–10 THz) has a plethora of desirable attributes such as its non-ionizing nature, good transmission through many optically opaque materials for imaging applications and the ability to characterize many biochemical molecules and illegal drugs. Electronics is pushing its boundaries into this far-infrared region, driven by the promising applications in a broad range of disciplines. But because natural materials providing the required functionalities are not currently available in this spectral domain[8], there is a great lack of basic optical components necessary for the effective manipulation of terahertz waves.

The metamaterial device proposed by Chen and co-workers consists of carefully designed gold split-ring resonators (SRRs) measuring 36 μm across. An array of SRRs with a 50-μm period was deposited on an n-doped GaAs layer, where the combination of both forms a Schottky diode. By applying a voltage, the carrier depletion in the layer underneath the SRR can be controlled and the otherwise conductive substrate that shunts the gap capacitance of the SRR becomes increasingly electrically isolating. This causes the formation of a resonant spectral response of the SRR which can greatly alter the magnitude and the phase (complex amplitude) of a transmitted terahertz wave. Depending on the frequency, different operational regimes can be used. Directly on resonance, the phase of the transmitted field remains almost the same but the amplitude is strongly modulated, whereas slightly off-resonance the opposite behaviour occurs. At a negligible amplitude modulation a significant phase variation of 0.56 radians occurs, making it possible to obtain a complete 2π phase variation from a metamaterial with only a few functional layers. Fabrication of such stacked structures was recently shown to be feasible[9].

Moreover, as the transmitted amplitude and the phase are intrinsically linked by the Kramers–Kronig relationship, the combined action allows modulation of the complex amplitude over a large spectral domain.

The main contribution of Chen *et al.*, however, has to be their effort to push such physical resonance phenomena into a practical application. The authors have shown that in comparison with a mechanical chopper their switch performs admirably as an optical modulator when set to work in a modern terahertz time-domain spectroscopy system[10]. Unlike the mechanical chopper, the metamaterial modulator is compact and suits integration with electronic circuitry because it can be fabricated by standard microprocessing techniques. Another important benefit is that its modulation frequency can reach a few megahertz, which is orders of magnitude faster than the kilohertz modulation of its mechanical counterpart.

Beside the demonstration of the control of phase at terahertz frequencies, the work also contributes to the general efforts of pushing carefully customized metamaterials towards feasible applications. Such efforts are necessary if this field of research is to be lifted from a purely academic orientation towards an application-driven field. Although Chen and co-workers' device still has some intrinsic limitations and is not yet optimized (for example, amplitude transmission is reduced if the phase modulator is operated close to the resonance frequency), their contribution is a beautiful example of how metamaterials can serve applications for which otherwise no solutions exist. It will be challenging to translate this concept to other spectral domains, where well-established technologies do exist, but the hope remains that this work will stimulate new ideas on how to build functional devices from metamaterials that fulfil a desired functionality. ❐

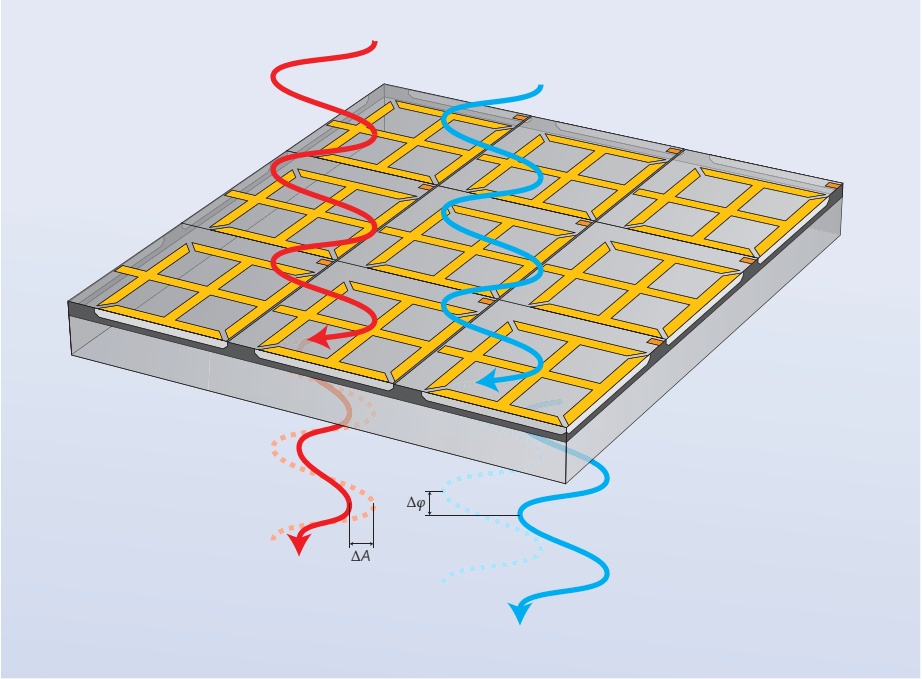

Figure 1 | Diagram of the proposed metamaterial modulator. By applying a voltage, the transmitted signal can be modulated either in phase (φ, blue) or in amplitude (A, red), depending on the operational frequency relative to the resonance frequency.

Carsten Rockstuhl is at the Institute of Condensed Matter Theory and Solid State Optics, Friedrich-Schiller-Universität, Jena 07743, Germany.
Weili Zhang is at the School of Electrical and Computer Engineering, Oklahoma State University, Stillwater, Oklahoma 74078, USA.
emails: carsten.rockstuhl@uni.jena.de; weili.zhang@okstate.edu

References

1. Soukoulis, C. M., Linden, S. & Wegener, M. *Science* **315,** 47–49 (2007).
2. Smith, D. R., Schultz, S., Markos, P. & Soukoulis, C. M. *Phys. Rev. B* **65,** 195104 (2002).
3. Chen, H.-T. *et al. Nature Photon.* **3,** 148–151 (2009).
4. Pendry, J. B. *Phys. Rev. Lett.* **85,** 3966–3969 (2000).
5. Schurig, D. *et al. Science* **314,** 977–980 (2006).
6. Garcia-Vidal, F. J. *Nature Photon.* **2,** 215–216 (2008).
7. Huang, Y.-F. *et al. Nature Nanotech.* **2,** 770–774 (2007).
8. Ferguson, B. & Zhang, X.-C. *Nature Mater.* **1,** 26–33 (2002).
9. Liu, N. *et al. Nature Mater.* **7,** 31–37 (2008).
10. Grischkowsky, D. R. *et al. J. Opt. Soc. Am. B* **7,** 2006–2015 (1990).

TERAHERTZ TECHNOLOGY

Mind the gap

Researchers in South Korea and the Netherlands have demonstrated that the enhancement of the electric field of terahertz radiation inside a nano-slit continues to grow, even when the slit becomes narrower than the skin depth of the material.

Luis Martin-Moreno

Research in the terahertz (THz) region of the electromagnetic spectrum (0.03–3 mm wavelength) has boomed since the appearance of solid-state coherent THz sources. The interest arises from the great potential of THz spectroscopy and imaging equipment. Applications include molecular recognition (many vibrational modes of molecules lie in the THz range) and security screening — dielectrics are mostly transparent to THz waves whereas metals are opaque, and plastic explosives and drugs present characteristic absorption lines. Other potential uses are the non-destructive analysis of biological tissue, which makes it possible to differentiate between fat and muscle, or between tumours and healthy tissue, for example.

Terahertz antennas[1] are an important part of the growing toolbox of THz technology. The work by Seo *et al.*, described

on page 152 of this issue[2], measures the enhancement of a THz electric field inside a slit of width around 30,000 times smaller than the wavelength λ, reporting an intensity enhancement of $|E|^2 \approx 10^5$.

Of course, field enhancements in gaps much smaller than the wavelength are commonplace: a capacitor with a linear dimension of 1 cm connected to the 50-Hz power grid would have λ/width = 6×10^8. What makes the work of Seo *et al.* different is not only that this large ratio occurs for THz frequencies, but that it considers a previously unexplored regime in which the skin depth, which is a measure of how quickly the fields decay inside the metal, is larger than both the film thickness (60 nm in the experiment) and slit width (as small as 70 nm in the experiments and 20 nm in the simulations).

A way to understand the field enhancement in a nanogap in a metal substrate in the usual situation, when the skin depth is smaller than any other dimension of the system, is to start by considering an opaque flat metal plane. When this plane is illuminated by a normal-incident electromagnetic field, electrical currents oscillate freely. If the plane ends in a discontinuity perpendicular to the incident electric field, charges accumulate close to the edge. A slit formed by two such discontinuities will accumulate (oscillating) charges of different sign. The average electric field in the gap is proportional to the amplitude of the charge, which is proportional to the distance at which the oscillating current feels the discontinuity — that is, proportional to the wavelength. The electric field increases with decreasing slit width: as the slit gap closes, charges at both sides attract each other with increasing strength, which brings them closer to the edge.

The question is, can this view be maintained when the width and depth of the nanogap are smaller than the skin depth? Seo *et al.* have now provided an answer by performing numerical simulations showing that the electric field is largely enhanced, even in the case when the metal thickness is only 1/4 of the skin depth (see Fig. 1 for a representative example). Moreover, the simulations show that the electric field still concentrates in the gap even for slit widths smaller than 1/10 of the skin depth. This occurs because the incident field excites what essentially is a transverse electromagnetic waveguide mode in the slit, with the electric field perpendicular to the gap wall. Continuity of the displacement vector implies that the electric field is enormously reduced inside the metal (the dielectric constant of gold in the THz regime is of the order of 10^7), so how quickly the field decays inside the metal is of no importance.

Seo *et al.* also provide experimental confirmation of the intense enhancement of the THz electric field in nanocapacitors and its increase with shrinking gap width, even in the sub-skin-depth limit. For this, they first measured the electric field amplitude in the far field of a slit in a nearly free-standing gold film. The measurement was done through electro-optic sampling time domain spectroscopy, which takes advantage of the proportionality between the electric field and the measurable birefringence it induces in certain non-centrosymmetric materials. Second, the measured far-field amplitude was related to the electric field in the gap through diffraction theory and the assumption (based on the numerical results) that the field is concentrated in the gap. Although not a direct measurement of the electric field in the gap, the validity of the estimation is supported by the good agreement with the computed results. It also tells us something about the quality of the sample: to compare with the simulations (performed for an infinitely long slit), the actual slit had to maintain a uniform 70-nm gap width for ~1 cm (giving a remarkable top-view aspect ratio of around 10^5).

These results may find applications in enhancing the interaction between THz radiation and nanoparticles (with a spatial resolution of a few tens of nanometres), in THz signal detection in astronomy (where the low-pass filtering properties may come as a bonus) and in THz nonlinear optics. In this last case, the reported field enhancement should already be enough to induce nonlinearity directly in semiconductor structures with existing THz sources.

To take full advantage of the spatial resolution and field-enhancing capabilities, it would be convenient to have a method for fabricating centimetre-long slits with reduced width (the electric field is expected to increase at least until the slit width is of the order of the electron mean free path, which is 1 nm). Also, for nonlinear applications, it will be necessary to fill the gap selectively with an appropriate nonlinear material. This may not prove easy. However, there is plenty of room for improvements, especially given that the analysed single-slit structure presents a broadband (non-resonant) response. Combining it with other types of resonant THz antennas (for instance by proper corrugation of the metal surface a few wavelengths from the slit[3]) could further enhance the electric field at some wavelengths. ❐

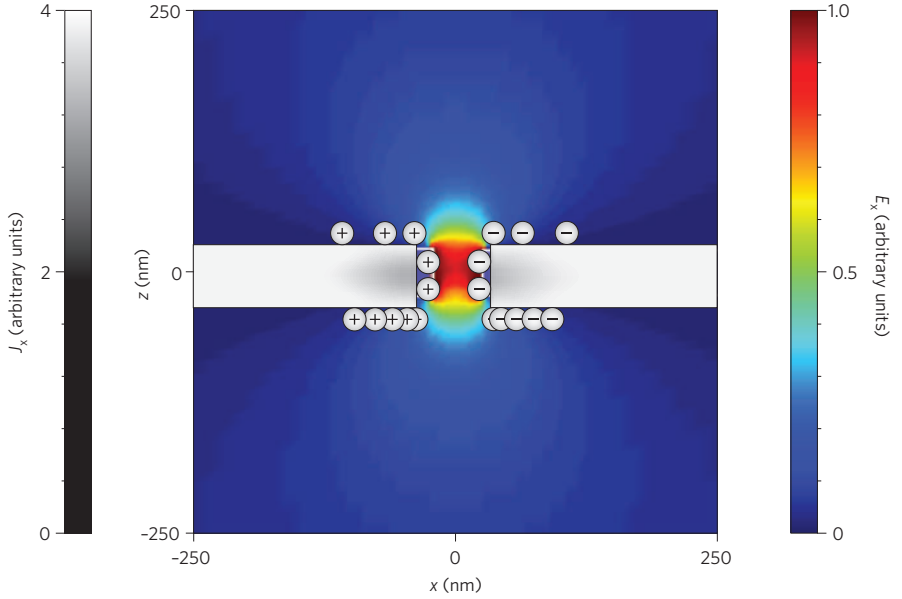

Figure 1 | Computed electric field amplitude, *E*, and current, *J*, for a 70-nm-wide slit in a 60-nm-thick gold film. The film lies on a 1.2-μm-thick SiO_2 layer on top of a 0.5-μm SiN layer. The structure is illuminated from the SiN side with a normal-incident plane wave with λ = 0.3 mm (for which the skin depth of gold is 250 nm).

Luis Martin-Moreno is in the Instituto de Ciencia de Materiales y Departamento de Fisica de la Materia Condensada, CSIC-Universidad de Zaragoza, C/Pedro Cerbuna 12, 50009 Zaragoza, Spain.
e-mail: lmm@unizar.es

References

1. Huber, A. J *et al. Nano Lett.* **8,** 3766–3770 (2008).
2. Seo, M. A. *et al. Nature Photon.* **3,** 152–156 (2009).
3. Lezec H. J. *et al. Science* **297,** 820–822 (2002).

METAMATERIALS

Chirality-assisted negative index

The creation of a negative refractive index — responsible for a host of interesting phenomena, including negative refraction, the inverse Doppler effect and reverse Čerenkov radiation — usually requires a material with simultaneous negative permittivity and negative magnetic permeability. The problem is that this is hard to achieve in practice, especially at optical wavelengths.

It now seems that manmade chiral metamaterials may provide an answer. Two separate research collaborations in the United States and Europe have now independently provided experimental proof that such chiral materials can be fabricated to provide a negative index in the terahertz and microwave regions.

Shuang Zhang and colleagues at the University of California, Berkeley, and Oklahoma State University report a negative index at terahertz frequencies with the assistance of a man-made chiral metamaterial (*Phys. Rev. Lett.* **102,** 023901; 2008), while Eric Plum at the University of Southampton and an international team of collaborators report a negative index due to chirality at gigahertz frequencies (*Phys. Rev. B* **79,** 035407; 2008).

Both results make use of chirality — a structural design that does not show mirror symmetry. Some naturally occurring materials, such as milk or sugar solutions, have extremely weak chirality. Now chirality in man-made metamaterials that is orders of magnitude stronger than in those natural materials has been demonstrated.

Chirality plays a part in all fields of physics. In optics, it is known for its effect on the spin of photons: that is, its influence on left-handed and right-handed circularly polarized light. In conventional materials, these two circular polarizations propagate with the same phase velocity.

According to Zhang, once chirality is introduced, this behaviour is changed, with one polarization propagating with a faster phase velocity and the other with a slower phase velocity. "If the chirality is really strong, one circular polarization will experience very slow phase velocity and even finally becomes negative. As a result, the refractive index can be negative even though the permittivity and permeability are not simultaneously negative, as required by the conventional negative index materials consisting of small metallic coils and rods", he told *Nature Photonics.*

The Zhang group used this effect to observe a negative index between

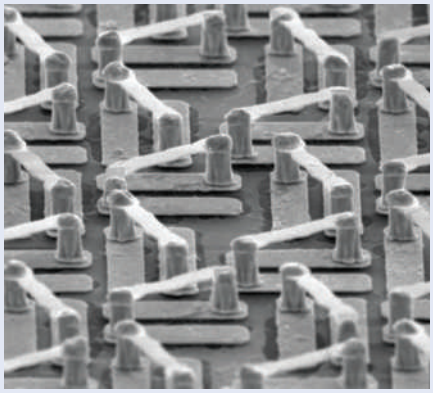

UNIVERSITY OF CALIFORNIA, BERKELEY

1.06 and 1.27 THz in a sample measuring 1.5 cm × 1.5 cm composed of an array of micrometre-scale gold resonators (image above) with bridges roughly 20 μm long elevated by pillars 4.5 μm tall.

The results are likely to inspire further work into the potential for chiral metamaterials, such as isotropic and active designs. The US team is now working towards a new type of chiral metamaterial that can flip the handedness of the chiral structures upon illumination by a control light beam.

DAVID PILE

IMAGING

Seeing diamond defects

The high-resolution imaging of individual colour centres in diamond using stimulated emission depletion microscopy is set to offer new insights into the physics underlying solid-state light emitters.

Vahid Sandoghdar

Although optical techniques have played an important part in the development of natural sciences and engineering, diffraction has been a serious limitation for a long time — arguably too long. In the context of optical microscopy, this limitation is often formulated as the Abbe limit, which restricts the resolution of imaging to $(\lambda/2)$NA, with NA being the numerical aperture of the imaging system and λ the wavelength of illumination. Put simply, the long-held wisdom has been that the wave nature of light does not let us resolve two light emitters that are spaced at nanometre separations.

The dogma of this diffraction limit being a fundamental barrier in optical studies was seriously brought into question when scanning near-field optical microscopy (SNOM) was introduced in the 1980s[1,2]. Research showed that if one images a sample using non-propagating near fields, there is no theoretical limit on how high the resolution can be. Unfortunately, SNOM has proved to be very difficult to implement at a resolution below 50 nm because of challenges associated with reproducible probe fabrication and very small signals. Furthermore, it is by nature only applicable to surface studies. Nevertheless, SNOM fueled single-molecule microscopy[3], which in turn provided a viable approach for achieving very high spatial resolutions. The idea is that if one can turn on each molecule selectively, one can determine the centre of the point spread function of each molecule very accurately, thus resolving them even if they are very close to each other. Indeed, single dye molecules spaced by about 10 nm have been resolved in three dimensions at liquid helium temperature, where the exquisite spectral selectivity allows one to address each molecule separately[4].

Another important development that took place somewhat in parallel with SNOM and single-molecule microscopy was nonlinear optical microscopy[5]. Although standard multiphoton fluorescence imaging schemes do not offer a big advantage in resolution, stimulated emission depletion (STED) microscopy[6] has revolutionized our views of resolution in far-field microscopy. In this technique, one uses stimulated emission to depopulate the excited state of the fluorescence molecule in the outer shell of the laser spot. This results in a smaller effective excitation area, which has been shown to go below 20 nm in size. But the theory does not put any limit on how high the resolution can become. Just imagine deciphering the images of several optical emitters spaced by 1 nm in a 'normal' microscope. The work on imaging nitrogen-vacancy (NV) diamond colour centres (point defects in diamond that are occupied by a nitrogen atom and emit red light; see Fig. 1), which is reported on page 144 of this issue by Eva Rittweger and co-workers[7], brings us very close to a laboratory demonstration of this imaginary scheme.

Although the concept of STED microscopy has been widely reported and its attractive attributes of high spatial resolution and imaging speed have been successfully applied to biological imaging[8], its application to imaging diamond colour centres, reported in this issue, is worth examining for several reasons. As with all fluorescence techniques, one of the difficulties of STED microscopy has been the limited photostability of the fluorophores. It turns out that typical emitters undergo photochemical processes after about 10^6–10^9 excitations under ambient conditions, but NV colour centres in diamond are among the very few emitters that are exempt from this seemingly universal rule of thumb. Furthermore, they have become very popular for studies in quantum information processing because of their attractive energy level schemes and long electron spin coherence times, which can be detected by optical spectroscopy even at room temperature.

The report on STED imaging of NV centres with unprecedented resolution[7] is important because it provides a playground for exploring the limits of STED microscopy in achieving ultrahigh resolution down to the nanometre scale. Although Rittweger *et al.* present images of colour centres that are many tens of nanometres apart, they also demonstrate very convincingly that they have the capability to resolve such emitters even if they were to be separated by less than 10 nm. Furthermore, they achieve a localization accuracy well below 1 nm. Given the mechanical and optical robustness of the system, it should then be possible to explore diamond crystals or nanocrystals with a very high density of colour centres. This would provide a non-invasive quantitative characterization method for the concentration and distribution of defects in both natural and man-made diamond products. In particular, STED imaging offers an easy and reliable method for examining arrays of colour centres created by ion bombardment of pure diamond layers[9].

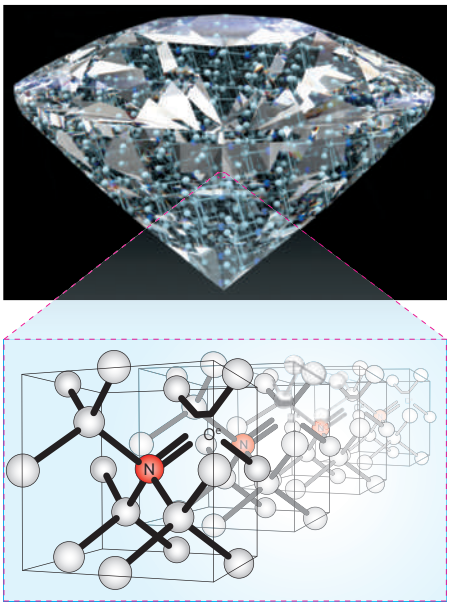

Figure 1 | Stimulated emission depletion microscopy can perform high-resolution imaging of individual nitrogen-vacancy colour centres in diamond. Expanded view shows the diamond structure with a substitutional nitrogen atom (N) and a neighbouring vacant site. Repeated occurrence of the nitrogen-vacancy centres would provide a playground for exploring the limits of resolution in optical microscopy.

Aside from realizing a dream-come-true in optical microscopy, near-atomic resolution of individual NV centres would open doors to exciting investigations of their interaction with their immediate nano-environments. Although NV centres are extremely robust against photobleaching, we have seen that their fluorescence lifetimes can vary a great deal in diamond nanocrystals, indicating fluctuations in their local environments. STED microscopy could help to shed light on the character of these variations. Another prospect concerns the coupling of the electron spin of a NV to the spins of the neighbouring ^{13}C nuclei in the matrix[10]. STED imaging of densely packed colour centres could allow one to investigate the coherent coupling of several very close-lying NV centres to a common nuclear environment, opening new possibilities for room-temperature multipartite entanglement. A subtle aspect to point out, though, is that the nature of STED imaging does not allow one to address several neighbouring emitters at the same time, because fluorescence is always depleted from a diffraction-limited region of the imaging centre.

Zooming in on emitters that are arranged at atomic-scale separations could open new frontiers but might be accompanied by complications. Reaching atomic resolution by STED imaging would mean that the commonly used dipole approximation for treating the interaction between the excitation light and the emitter no longer holds. In other words, one would have to account for the strong spatial variation of the optical fields on length scales comparable to the emitter size. At the same time, material issues might arise. For instance, NV centres that are too close to each other might perturb the lattice enough to cause spectral instabilities. Furthermore, interactions such as dipole–dipole coupling could complicate the spatial images because absorption and emission of photons might not be directly linked to one well-defined emitter; instead, the optical excitation would be delocalized in the coupled system. Such interactions would have to be identified and taken into account[4].

Having the great advantage of being non-destructive and providing ultrahigh resolution at room temperature, STED microscopy promises to become a workhorse in optical studies of densely packed solid-state emitters in general. Some might have expected that the NV centres could not be seen by STED imaging. Others would have thought that of course STED microscopy should also image NV centres. But as they say, seeing is believing, and we now believe. ❐

Vahid Sandoghdar is at the Laboratory of Physical Chemistry and optETH, ETH Zurich, 8093 Zurich, Switzerland.
e-mail: vahid.sandoghdar@ethz.ch

References

1. Pohl, D. W., Denk, W. & Lanz, M. *Appl. Phys. Lett.* **44,** 651–653 (1984).
2. Lewis, A., Isaacson, M., Harootunian, A. & Muray, A. *Ultramicroscopy* **13,** 227–232 (1984).
3. Betzig, E. & Chichester, R. J. *Science* **262,** 1422–1425 (1993).
4. Hettich, C. *et al. Science* **298,** 385–389 (2002).
5. Denk, W., Strickler, J. H. & Webb, W. W. *Science* **248,** 73–76 (1990).
6. Hell, S. W. & Wichmann, J. *Opt. Lett.* **19,** 780–782 (1994).
7. Rittweger, E., Han, K. Y., Irvine, S. E., Eggeling, C. & Hell, S. W. *Nature Photon.* **3,** 144–147 (2009).
8. Westphal, V. *et al. Science* **320,** 246–249 (2008).
9. Meijer, J. *et al. Appl. Phys. Lett.* **87,** 261909 (2005).
10. Childress, L. M. *et al. Science* **314,** 281–285 (2006).

OPTICAL SWITCHING

Polariton diode microcavities

A transition between strong and weak coupling regimes in a polariton diode microcavity yields optically controlled switching of current. Researchers show bistable cycles for optical powers two to three orders of magnitude less than typical schemes.

Alexey Kavokin

More than 50 years ago, Gross *et al.*[1] demonstrated that excitons — electron–hole pairs bound by Coulomb interactions — can strongly modify the absorption spectra in semiconductors near their bandgap frequency. The excitons give rise to sharp peaks in the absorption spectra of semiconductors, which have an amplitude and shape that are particularly sensitive to temperature as well as external electric and magnetic fields.

Excitons are also a source of strong optical nonlinearity in semiconductors, making them promising for applications in a wide range of optical devices, including laser diodes and optical parametric oscillators. A group of researchers in Marcoussis, France, led by Jacqueline Bloch, have now shown that excitons can be used to make a bistable photocurrent device which uses a low-power optical beam to effectively switch current on and off[2]. The attraction of the device is that it operates with input optical powers that are two to three orders of magnitude less than that required from conventional bistable devices based on Kerr nonlinearity.

Put simply, optically bistable systems show two photonic states of operation, with switching between them controlled by another optical beam. Commonly, this is achieved by using nonlinear materials, for example those showing the Kerr nonlinear effect, that mediate the interaction between signal and control beams. Owing to relatively weak optical nonlinearities in such materials, however, they often require large optical intensities and do not allow the creation of compact devices.

Instead of using conventional optical nonlinearity to create a bistable device, Bloch and collaborators instead use a light-emitting p-i-n diode based on an electrically biased single-mode Fabry–Perot microcavity (see Fig. 1). The researchers take advantage of an abrupt transition between two distinct regimes in the microcavity, the so-called weak coupling and strong coupling regimes, to control current.

At weak coupling, enhancement or inhibition of spontaneous emission is possible by tuning the cavity. However, in the strong coupling regime, in which the photons in the cavity have a chance to exchange energy with the excitons, striking effects such as Rabi splitting, photon squeezing and anti-bunching are possible. The threshold from the weak to the strong coupling regime manifests itself by marked changes in the optical properties of the cavity, in particular the splitting of the exciton peak in the absorption spectrum into the so-called Rabi doublet[3].

The researchers' scheme allows controllable switching between the two regimes. At zero external bias the sample is in the weak coupling regime, owing to rapid dissociation of excitons under the effect of the built-in electric field of the p-i-n junction. The system can be shifted to the strong coupling regime if the internal electric field is compensated for by optical pumping. Now, if the external pumping is provided by a laser operating at a frequency resonant with one of the exciton–polariton modes, the absorption of light is much more efficient in the strong coupling regime than in the weak coupling regime.

This is where the bistability comes from: if the system is in the weak coupling regime, the photocurrent is low because of the low absorption; on the other hand, if it is in the strong coupling regime, the photocurrent is strong, because of the resonant absorption. The hysteresis cycle,

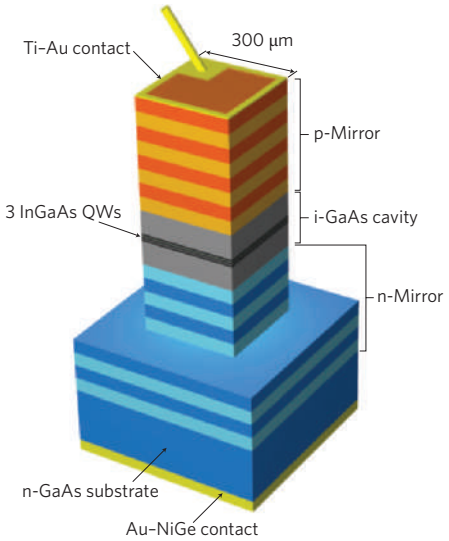

Figure 1 | Schematic structure of a microcavity polariton diode structure. Reproduced with permission from ref. 2. © 2008 APS.

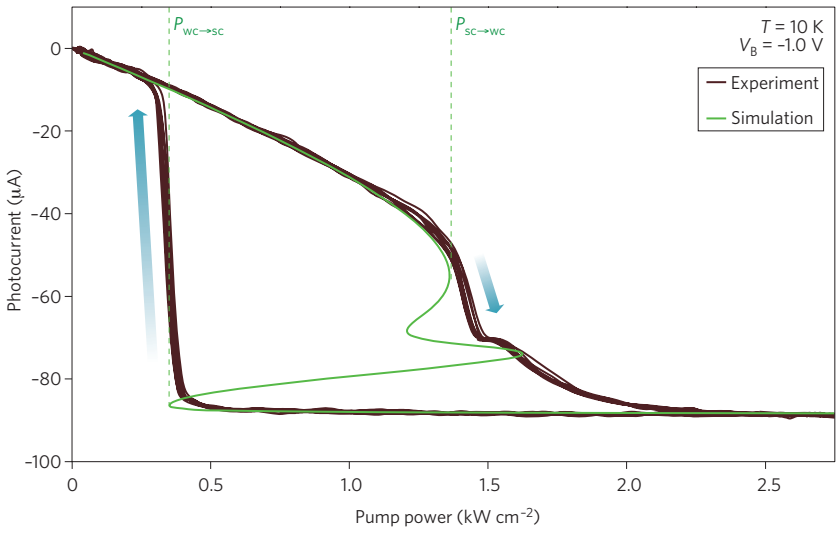

Figure 2 | Experimental (black) and simulated (green) photocurrent as a function of the optical excitation power. Here V_b is the bias voltage, WC → SC denotes transition from weak coupling to strong coupling and SC → WC indicates the reverse transition. Reproduced with permission from ref. 2. © 2008 APS.

or switching, experimentally observed by Bajoni *et al.* in the photocurrent dependence on the optical pumping power is shown in Fig. 2. The effect takes place at low excitation power (1–2 kW cm^{-2}), which is important for future device applications. Interestingly, illuminating a small spot on the sample is sufficient to bring the whole system into the strong coupling regime. Apparently the domain of strong coupling rapidly expands over the whole sample. The motion of domain walls in laterally patterned bistable microcavity systems ('polariton neurons'[4]) could be used for information processing in all-optical logic gates.

The field of polaritonics (or polaritronics[5]) is experiencing extremely rapid progress, and the work of Bajoni *et al.* is just one of a number of new developments. After the first observation of the strong coupling regime[3] in microcavities, exciton–polaritons have proved to be promising candidates for micro-sized optical parametric oscillators[6] and ultra-low-threshold semiconductor lasers[7]. They are also of enormous interest because they might demonstrate the fundamental physics of the Bose–Einstein condensation[8] and, possibly, superfluidity[9]. Owing to their macroscopic coherence length, the exciton–polaritons may be used as carriers of logical signals. The limitation comes from their extremely short lifetime (of the order of 10^{-12} s). Using bistable microcavity systems like that studied by Bajoni *et al.* allows one to overcome this limitation: the switching fronts between weak and strong coupling domains propagate over distances greatly exceeding the mean free path of individual exciton–polaritons. The nonlinear effects demonstrated by the Marcoussis group take place at low temperature (10 K). In the future, using these effects in large-bandgap materials such as GaN or ZnO may prove a more practical approach for room-temperature operation. ❐

Alexey Kavokin is at the Dipartimento di Fisica, University of Rome II "Tor Vergata", and at the Physics and Astronomy School of the University of Southampton, Highfield, Southampton, SO17 1BJ, UK.
e-mail: alexey@phys.soton.ac.uk

References

1. Gross, E. F. & Karryev, N. A. *Dokl. Acad. Sci. USSR* **84,** 261–264 (1952).
2. Bajoni, D. *et al. Phys. Rev. Lett.* **101,** 266402 (2008).
3. Weisbuch, C. *et al. Phys. Rev. Lett.* **69,** 3314 (1992).
4. Liew, T. C. H., Kavokin, A. V. & Shelykh, I. A. *Phys. Rev. Lett.* **101,** 016402 (2008).
5. Deveaud-Pledran, B. *Nature* **453,** 297–298 (2008).
6. Diederich, C. *et al. Nature* **440,** 904–907 (2006).
7. Christopoulos, S. *et al. Phys. Rev. Lett.* **98,** 126405 (2007).
8. Kasprzak, J. *et al. Nature* **443,** 409–414 (2006).
9. Amo, A. *et al. Nature* **457,** 291–295 (2009).

NONLINEAR OPTICS

Signal analyser on an optical chip

By carefully optimizing the properties of a waveguide made from a highly nonlinear glass, Australian researchers have achieved record optical nonlinearity and put it to use in a broadband radiofrequency spectrum analyser. The work could ultimately lead to improved all-optical signal processing.

Christophe Dorrer

Optical waves can modify the properties of the medium in which they travel by inducing a nonlinear response. These nonlinear responses can then be used to generate optical waves in new wavelength ranges and to modulate the propagation of light. Improving the efficiency and performance of nonlinear materials has the potential to open the door to a host of new practical applications and, on page 139 of this issue, Mark Pelusi and colleagues in Australia illustrate an example of this[1]. By optimizing the linear properties of a waveguide made from a highly nonlinear glass, they have created an ultrafast, broadband, chip-based all-optical radiofrequency spectrum analyser. The device is distortion-free, and offers a bandwidth greater than 2.5 THz and flexible wavelength operation.

Measuring the temporal properties of signals — be they electrical or optical — is important in the fields of electronics, optical telecommunications and ultrafast optics. The radiofrequency (RF) spectrum of a time-varying (electrical or optical) signal corresponds to the spectrum of the intensity of the signal and is commonly used to characterize the time-varying characteristics of the source. For example, it can be used to detect impairments such as distortion induced by components in an electrical circuit, or the broadening of a data-encoded optical signal in a telecommunication network that could potentially degrade the performance of the transmission link (Fig.1).

The RF spectrum is a fundamentally different quantity from the optical spectrum, which is the spectral power distribution of the electric field of the optical wave. The optical spectrum quantifies the spectral density of the source at different optical frequencies but relays no information about the way in which different spectral components are correlated and, in general, does not provide much information about the temporal variations of an optical waveform.

Measuring the RF spectrum of an optical source typically involves detecting the time-varying intensity of the source using a photodetector and analysing the generated photocurrent with an electrical RF spectrum analyser. This approach requires components that have a bandwidth of the order of the inverse of the temporal variations of the source under test. Optical sources can have a bandwidth significantly larger than electrical components and photodetectors; for this reason, optical-to-electrical conversion can be limited in terms of bandwidth, thus leading to an incomplete description of the properties of the optical source.

In contrast to electrical components, the intrinsic response time of optical materials is usually in the femtosecond range, meaning that the nonlinear optical response to an excitation is quasi-instantaneous. As a result, the intensity of an optical wave can modulate the properties of the medium, and therefore the propagation of other optical waves, at a very high bandwidth. This opens the door to signal analysis based on nonlinear optics at far higher frequencies than electronics can accomplish.

The principle used by Pelusi *et al.*[1] is that the RF spectrum of one optical source under test is encoded onto the optical spectrum of another optical source using cross-phase modulation[2] — a nonlinear process that induces a phase proportional to the intensity of the source under test onto the electric field of the ancillary source.

In this way, the RF spectrum can be directly read after the nonlinear interaction as the optical spectrum of the phase-modulated source, provided that the nonlinear interaction has a large enough bandwidth to map the RF spectrum of the source under test onto the optical spectrum of the modulated source. The key aspect of this all-optical approach is that it bypasses the conversion to high-speed electrical signals and achieves an unprecedented bandwidth of several terahertz. This represents a more than tenfold improvement in bandwidth over electronics, and is limited only by the bandwidth of the nonlinear process and uncompensated linear propagation effects.

The material that Pelusi *et al.* use to produce their nonlinear photonic chip is a chalcogenide glass. This glass family has an intrinsically very high nonlinear index, n_2. For example, As_2Se_3, which has previously been used in optical fibres[3], has an index of about 10^{-17} m^2 W^{-1} (~500 times that of silica)[4]. The glass used in this demonstration, As_2S_3, on the other hand, has a nonlinear index of the order of 3×10^{-18} m^2 W^{-1}. The quantity n_2 describes the change in the optical refractive index proportional to the optical intensity (for linear propagation, the index does not depend on the intensity). Unfortunately, the linear dispersion of the chalcogenides can hinder their use in practical applications.

What Pelusi and colleagues have done is to optimize the As_2S_3 waveguide design to yield two benefits. First, the waveguide has a very small mode (this is where the optical waves are confined during propagation), which leads to an increase of the optical intensity and makes the nonlinear response stronger. Second, the design gives rise to a strong waveguide dispersion that offsets the material dispersion, meaning that dispersion effects (unwanted pulse broadening and distortion due to variation of phase velocity with wavelength) are not deleterious over distances for which significant nonlinear effects are induced.

In this work, the dispersion — and therefore the distortion and bandwidth limitation — is significantly reduced around the telecommunication wavelength of 1,550 nm. The area of the propagation mode is 1.9 μm^2; in comparison, the mode-field area of a highly nonlinear silica fibre is of the order of 10 μm^2. Because of the high intrinsic nonlinearity and concentration of the optical intensity into a tight spatial mode, large nonlinear effects that would typically require hundreds of metres of highly nonlinear silica fibre can be induced over short optical path lengths (in this case just 16 cm). The entire waveguide fits on a compact 6-cm-long substrate (Fig. 2), making it suitable for integration as a subsystem of a larger system.

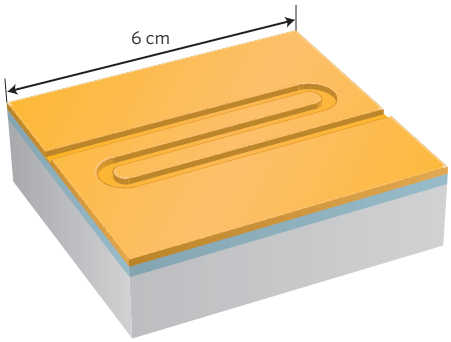

Figure 2 | Schematic of the waveguide fabricated by Pelusi and colleagues[1].

Using their component[2], Pelusi *et al.* make direct optical measurements of the RF spectrum of high-bit-rate (320 Gbit s^{-1}) optical sources that are impaired by various distortions. For the 320-Gbit s^{-1} telecommunication channel, data are encoded digitally in optical pulses, with one bit arriving at the receiver roughly every 3 ps. Although the data encoding is digital (0 and 1 being represented by the absence or presence of an optical pulse in a given bit slot), impairments caused by imperfect generation and propagation of the signals can lead to signal degradation (for example, significant chromatic dispersion could lead to a temporal overlap of pulses corresponding to different bit slots).

The chalcogenide waveguide fabricated in this work offers a considerable improvement on previous results that were based on a similar concept but used silica fibres. The measurement bandwidth is ultimately limited by the response time of the waveguide nonlinearity and uncompensated dispersion. Previous all-optical RF spectrum monitors have reported much narrower bandwidths due to the long fibre (~800 m) lengths required[2].

Monitoring high-bandwidth optical signals is important for research and development in optical telecommunications, and the results presented here are convincing. However, existing commercial optical networks operate at data rates of 40 Gbit s^{-1} and lower (that is, with a bit slot of 25 ps), for which bandwidths of the order of 100 GHz are likely to be required for performance monitoring.

An important feature of the waveguide designed by Pelusi and colleagues is that an efficient nonlinear interaction can be obtained for optical sources over an extended band of wavelengths. This colourless operation is important for characterizing multiple channels at different central wavelengths propagating in a fibre optical link, enabling a channel of interest to be filtered out and accurately characterized without modifying the wavelength of the ancillary source in the all-optical RF spectrum analyser. The engineered chalcogenide waveguide devised by Pelusi *et al.* could also replace highly nonlinear fibres in applications such as temporal pulse compression (reducing pulse duration), 'continuum generation' and processing information optically (for example, transferring information from one data-encoded channel to another without electrical conversion).

The development of optical structures with high nonlinearities and large figures-of-merit is of great practical importance, and photonic crystal fibres[5], silicon waveguides[6] and periodically poled structures[7] are other important examples of such structures. They are likely to be most useful where other nonlinear elements such as nonlinear crystals, nonlinear fibres and semiconductor optical amplifiers are currently being used — in all-optical signal processing, wavelength conversion and nonlinear optical sampling, for example. Although the results presented by the Australian team are very encouraging, there is of course room for improvement. Further reduction of the dispersion would lead to higher-bandwidth operation over a larger range of signal wavelengths. By increasing the total nonlinearity and decreasing the coupling losses and propagation losses of the waveguide structure, more sensitive operation would be possible and nonlinear effects could be induced with a lower optical intensity.

Finally, there is the usual issue of cost and reliability to sort out, both of which strongly affect the commercial adoption of new technologies. Although nonlinear devices have been developed for decades for applications in optical telecommunications, commercial optical networks and the associated diagnostics rely mainly on electronics and linear optics. ❐

Christophe Dorrer is at the Laboratory for Laser Energetics, University of Rochester, 250 East River Road, Rochester, New York 14623, USA.
e-mail: cdorrer@lle.rochester.edu

References

1. Pelusi, M. *et al. Nature Photon.* **3,** 139–143 (2009).
2. Dorrer, C. & Maywar, D. N. *J. Lightwave Technol.* **22,** 266–274 (2004).
3. Fu, L. B., Rochette, M., Taèed, V. G., Moss, D. J. & Eggleton, B. J. *Opt. Expr.* **13,** 7637–7644 (2005).
4. Lenz, G. *et al. Opt. Lett.* **25,** 254–256 (2000).
5. Russell, P. St. J. *J. Lightwave. Technol.* **24,** 4729–4749 (2006).
6. Foster, M. A. *et al. Nature* **456,** 81–84 (2008).
7. Langrock, C., Kumar, S., McGeehan, J. E., Willner, A. E. & Fejer, M. M. *J. Lightwave Technol.* **24,** 2579–2592 (2006).

DIFFRACTIVE OPTICS

Floral seduction

Certain species of flowers use iridescent petals featuring submicrometre-scale diffraction gratings to act as a pollination cue and attract insects. That's the finding of UK researchers who have just published a study of the *Hibiscus trionum* (below, left) and *Tulipa* species and the behaviour of bumblebees (*Science* **323,** 130; 2009).

It is well known that in animals, iridescence (change of colour with varying observation angle) is used for recognizing species as well as attracting and choosing promising candidates for mating. However, there has been much less study of how plants signal to animals, which is particularly important for the pollination cycle among other things. Conventional non-iridescent cues such as pigment colour, ultraviolet and polarization effects are assumed to provide signals, but many flowers also show iridescence (particularly in the blue and ultraviolet spectra) that is presumed to have a biological signalling function. Researchers have now shown that these iridescent features, causing continuously changing colour as seen by a moving observer such as an insect, are used by bumblebees to identify flowers.

Initially the team investigated the surface structure of hibiscus and tulip petals, revealing a rich and detailed texture that allowed the flower surfaces to function as diffractive optics in the ultraviolet and visible region. For example, petals of *T. kolpakowskiana* flowers were shown to be bi-periodic with one period of about 1 μm (below, bottom right) and larger undulations with a period of 29 μm (below, top right). With the knowledge of the petal surfaces, artificial flowers were then fabricated from disassembled compact disks.

To test the hypothesis of iridescent signalling, iridescent disks and non-iridescent disks both containing yellow, blue and violet pigments were offered to the bees. The iridescent disks yielded sucrose rewards, whereas the non-iridescent disks provided a less than appetizing quinine hemisulphate salt solution. After 80 feedings the bees dined on the iridescent disks more frequently than when they were first introduced. The conclusion drawn was that the bees were not only able to recognize the iridescent disks from the others, but also to associate that with a particular type of flower. Preference for iridescence was not affected by pigment colour. The researchers also did similar experiments with casts of actual flower surfaces to ensure that the behaviour was also observable with less regular and imperfect gratings. So far the researchers have identified ten angiosperm families containing species that show petal iridescence, but it is assumed that this is a very common feature of flowers.

DAVID PILE

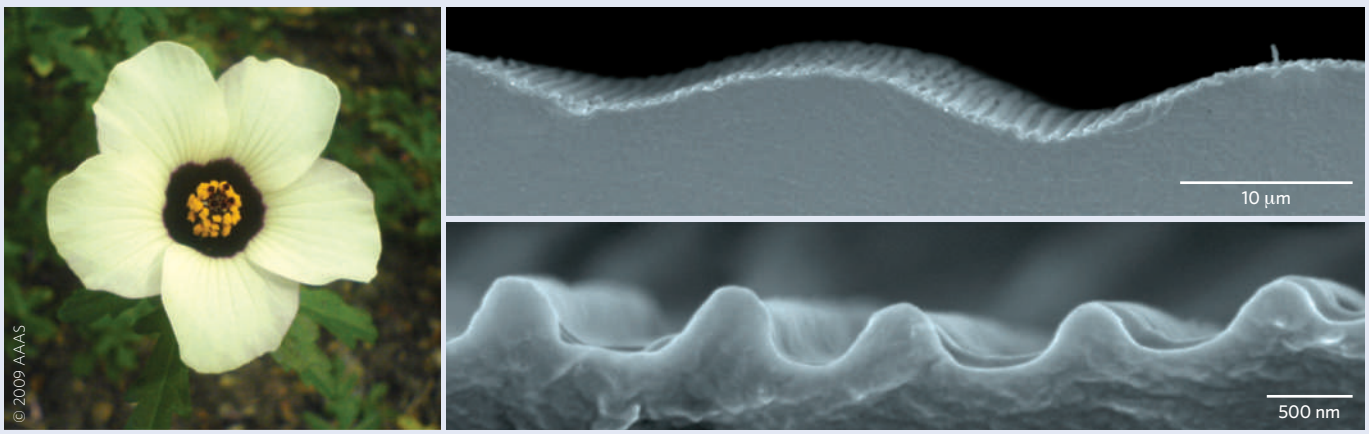

nature photonics

LETTERS

PUBLISHED ONLINE: 15 FEBRUARY 2009 | DOI: 10.1038/NPHOTON.2009.1

Photonic-chip-based radio-frequency spectrum analyser with terahertz bandwidth

Mark Pelusi[1]*, Feng Luan[1], Trung D. Vo[1], Michael R. E. Lamont[1], Steven J. Madden[2], Douglas A. Bulla[2], Duk-Yong Choi[2], Barry Luther-Davies[2] and Benjamin J. Eggleton[1]

Signal processing at terahertz speeds calls for an enormous leap in bandwidth beyond the current capabilities of electronics, for which practical operation is currently limited to tens of gigahertz[1]. This can be achieved through all-optical schemes making use of the ultrafast response of $\chi^{(3)}$ nonlinear waveguides[2]. Towards this objective, we have developed compact planar rib waveguides based on As_2S_3 glass, providing a virtual 'lumped' high nonlinearity in a monolithic platform capable of integrating multiple functions. Here, we apply it to demonstrate, for the first time, a photonic-chip-based, all-optical, radio-frequency spectrum analyser with the performance advantages of distortion-free, broad measurement bandwidth (>2.5 THz) and flexible wavelength operation (that is, colourless). The key to this is the waveguide's high optical nonlinearity and dispersion-shifted design. Using the device, we characterize high-bit-rate (320 Gb s^{-1}) optical signals impaired by various distortions. The demonstrated ultrafast, broadband capability highlights the potential for integrated chip-based signal processing at bit rates approaching and beyond Tb s^{-1}.

The nonlinear signal propagation underpinning the operation of our set-up arises from intensity-dependent effects, which can take the form of self-phase modulation (SPM), cross-phase modulation (XPM) or four-wave mixing[2] to enable a range of all-optical signal-processing functions, such as regeneration[3,4], wavelength conversion[5–7], switching[8,9], phase conjugation[10] and performance monitoring[11–14]. These have been reported with various waveguides including fibre[6,7,9,12–14], silicon[4,5,10] and semiconductor optical amplifiers (SOA) (ref. 8). Among these, optical-fibre waveguides exhibiting near-instantaneous $\chi^{(3)}$ nonlinearity[2] provide unrivalled speed capability. However, the low optical nonlinearity of most silica-based fibres means a long propagation length is necessary, leading to detrimental effects owing to dispersion. Although compact silicon chip devices have been reported, their free-carrier effects and two-photon absorption[5] can inhibit ultrafast signal processing. The SOA offer compact solutions, but their signal bandwidth can also be limited by free carriers. So, finding an alternative compact, ultra-high nonlinearity waveguide is a compelling requirement for future high-speed optical communication systems.

An application highlighting the enormous bandwidth potential of all-optical schemes over electronics is the monitoring of the radio frequency (RF) spectrum of a signal, that is, the power spectrum of its intensity waveform. Used routinely in telecommunications and microwave photonics for measuring distortions in amplitude or phase[15] and for characterizing components, it typically uses an expensive high-speed photodetector in combination with an electrical spectrum analyser. The electronic bandwidth limits of this approach, however, make it inadequate for measuring signals much faster than 40 Gb s^{-1}.

Here, we report the first demonstration of an all-optical terahertz-bandwidth RF spectrum monitor based on a monolithic $\chi^{(3)}$ nonlinear waveguide. Our approach makes use of XPM in a compact dispersion-engineered photonic chip fabricated from highly nonlinear As_2S_3 chalcogenide (ChG) glass. The principle of the all-optical RF spectrum analyser[16] is summarized in Fig. 1a. The RF spectrum of an optical signal (with electric field E) is the power spectrum of its temporal intensity ($|E(t)|^2$) given by the squared magnitude of its Fourier transform, $S_{RF}(\omega) = |\int |E(t)|^2 e^{i\omega t}\,dt|^2$, where t and ω are time and angular frequency, respectively, and $\int$ denotes integration from $-\infty$ to $+\infty$. This differs from the power spectrum of the electric field itself, given by $S_o(\omega) = |\int E(t) e^{i\omega t}\,dt|^2$, which is obtained from an optical spectrum analyser (OSA). The optical signal under test at wavelength λ_s is launched into a $\chi^{(3)}$ nonlinear waveguide with a weak continuous-wave (c.w.) probe at wavelength λ_p. By the optical Kerr effect, the waveguide refractive index n varies with the signal's temporal intensity I according to $n(I) = n_0 + n_2 I$ for linear and nonlinear refractive indexes of n_0 and n_2, respectively[2]. This induces XPM of the probe on an ultrafast timescale, whereby its phase is modulated in proportion to $I\gamma L$ (ignoring propagation losses), where L is the waveguide length and γ the waveguide nonlinearity coefficient[2] given by $\gamma = (2\pi/\lambda_s)(n_2/A_{eff})$ for an effective mode area A_{eff}. This generates frequency modulation sidebands around the monochromatic probe of frequency ω_0 (corresponding to λ_p) according to $S_o'(\omega) \propto |\gamma L|^2 S_{RF}(\omega - \omega_0)$, which enables $S_{RF}(\omega)$ to be measured on an OSA (ref. 16).

This scheme is capable of an enormous measurement bandwidth, greater than 10 THz, which is ultimately limited by the response time of the waveguide nonlinearity. Previous all-optical RF spectrum monitors have reported much narrower bandwidths owing to the requirement for long lengths of highly nonlinear silica fibre (HNF), in which the broadband dispersion characteristics degrade the phase (and group velocity) matching between the signal and probe[16].

To overcome this, our photonic-chip RF spectrum analyser (PC-RFSA) takes advantage of the high $n_2 \approx 3 \times 10^{-18}$ m^2 W^{-1} of As_2S_3 (>100 times of silica) and our ability to tailor A_{eff} to very small dimensions. This enhances γ to hundreds of times that of HNF, allowing a much shorter waveguide to be used, and also produces strong waveguide dispersion, which compensates the material dispersion, reducing the net dispersion to near zero at 1,550 nm wavelength. This results in a dramatically reduced footprint and the consequent performance advantages of distortion-free, broad measurement bandwidth (>2.5 THz) and colourless operation, allowing our device to be operated on any desired channel.

A schematic and image of the fabricated waveguide[17] are shown in Fig. 1b. Reducing the As_2S_3 film thickness was key to our design, as it leads to a strong waveguide dispersion that can offset the large material component of -364 ps nm^{-1} km^{-1} (normal dispersion)[18]. This is evident for the transverse-magnetic (TM) mode when its field permeates

[1]CUDOS, Institute for Photonic Optical Sciences (IPOS), School of Physics, University of Sydney, New South Wales 2006, Australia, [2]CUDOS, Laser Physics Centre, The Australian National University, Canberra, ACT 0200, Australia; *e-mail: m.pelusi@physics.usyd.edu.au

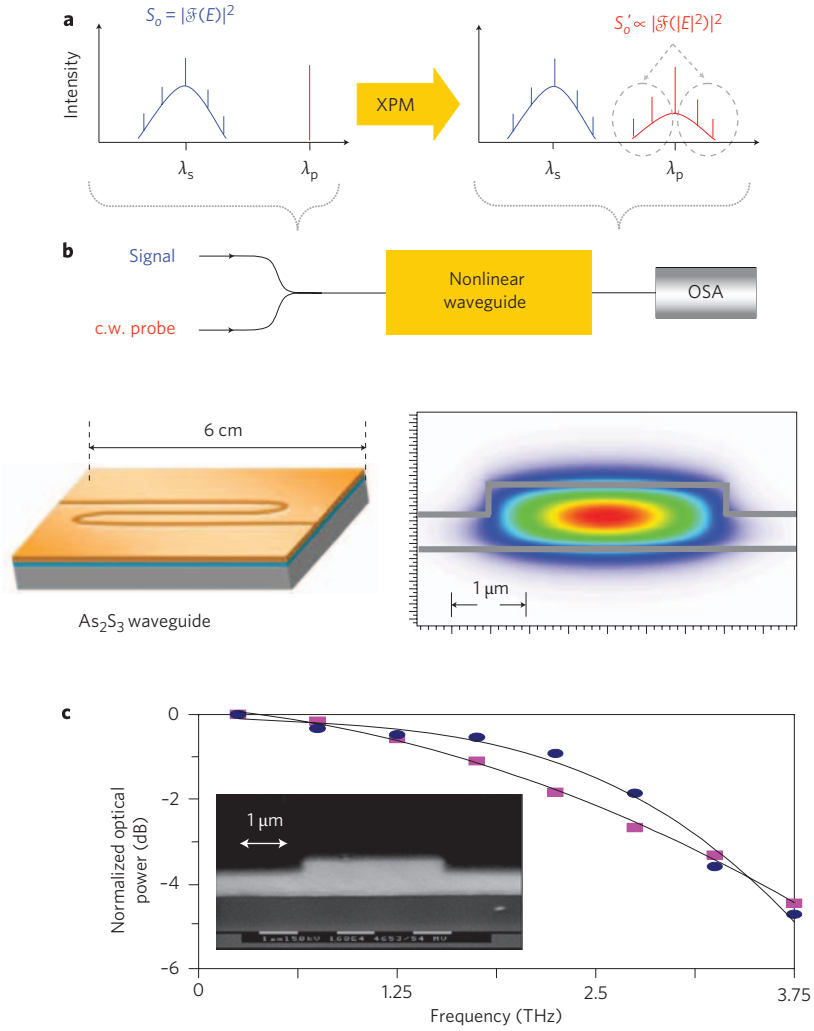

Figure 1 | Key aspects of the PC-RFSA. a, Principle for making use of XPM in a waveguide to capture the power spectrum of a signal's temporal intensity on an OSA according to $S_o' = |\mathfrak{F}(|E|^2)|^2$ (where $\mathfrak{F}$ denotes the Fourier transform and E is the electric field), which is distinct from the signal optical spectrum, S_o. **b**, Waveguide schematic and numerically generated TM mode intensity profile for a 3-μm rib width. **c**, Measured magnitude–frequency response showing bandwidth of the PC-RFSA for a 4-μm-wide rib waveguide with the signal at 1,550 nm and the probe at 1,530 nm (squares) and 1,569 nm (circles). Inset: Micrograph image of an As_2S_3 waveguide.

the rib top surface, as shown in Fig. 1b for the numerical intensity-mode profile calculated for the waveguide dimensions of 0.87 by 3 μm. This gave a value of $A_{eff} \approx 1.9$ μm^2 at the 1,550 nm wavelength, corresponding to $\gamma \approx 7{,}250$ W^{-1} km^{-1} and a net dispersion D (defined as differential of the group delay with wavelength) of ~40 ps nm^{-1} km^{-1} (anomalous dispersion). Mode solving for the 4-μm-wide rib of the same height predicted a smaller D, and $\gamma \approx 5{,}560$ W^{-1} km^{-1}.

To characterize the measurement bandwidth of the PC-RFSA, we applied a sine-wave signal at $\lambda_s = 1{,}550$ nm and tuned its beat frequency (Δf) while measuring the power of the XPM sideband that was generated around the c.w. probe[16] at $\lambda_p = 1{,}530$ nm. The total launch power was fixed at 118 mW (100 mW for the signal). This revealed a 3-dB bandwidth of 2.5 THz for the 3-μm rib waveguide. Repeating the experiment for the 4-μm rib gave a broader bandwidth of 3 THz (Fig. 1c) which is explained by its lower D. A similar bandwidth of 3.2 THz was also measured when λ_p was shifted to 1,569 nm, highlighting the small dispersion variation with wavelength and the potential for colourless operation.

We then applied the 3-μm rib PC-RFSA to characterize high-speed 320 Gb s^{-1} signals subject to various impairments using the experimental set-up shown in Fig. 2. The signal was launched into the waveguide with a c.w. probe at $\lambda_p = 1{,}546$ nm and total power of 127 mW (90 mW signal average). Its output was measured on an OSA with a spectral resolution of 0.01 nm (1.25 GHz) and converted to frequency scale. The resulting RF spectrum, shown in Fig. 3c(i), demonstrated good agreement with the numerically calculated RF spectrum of an ideal 320 Gb s^{-1} signal (grey curve). The dynamic range of the measurement, defined as the ratio of the 320 GHz tone above the OSA noise floor was 35 dB. The low signal distortion in the waveguide was confirmed by measuring its output on an optical sampling oscilloscope (OSO) after filtering out the probe (Fig. 2ii). A small difference in the output-signal eye diagram was observed when substituting the waveguide for an attenuator (Fig. 2i).

We then used the PC-RFSA to characterize a distorted 320 Gb s^{-1} signal simulated by misaligning the optical time-division multiplexing (MUX) stage of its generation. Doing so created an amplitude modulation as shown by the OSO trace in Fig. 3a(ii). Although the signal optical spectrum appeared unchanged (Fig. 3b(ii)), the PC-RFSA revealed the formation of a 160 GHz clock tone and other harmonics (Fig. 3c(ii)).

The PC-RFSA was also used to monitor 320 Gb s^{-1} signals distorted by group velocity dispersion (GVD)[12] and differential group

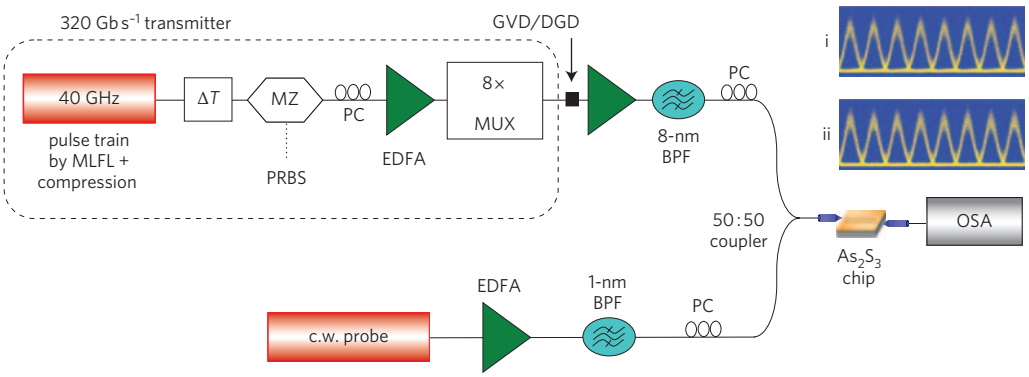

Figure 2 | Experimental set-up for measuring 320 Gb s^{-1} signals using the PC-RFSA. Signal distortion is introduced by non-optimal optical time-division multiplexing (MUX) (that is, unequalized amplitude and phase alignment between interleaved 40 Gb s^{-1} channels), or transmission induced group velocity dispersion (GVD) or differential group delay (DGD). ΔT, optical delay line; PC, polarization controller; MLFL, mode-locked fibre laser; PRBS, pseudo-random bit sequence generator; EDFA, erbium-doped fibre amplifier; OSA, optical spectrum analyser; MZ, Mach–Zehnder modulator. Inset: eye diagrams of 320 Gb s^{-1} signals (of 3.125-ps bit period and power in arbitrary units) measured on an optical sampling scope after transmission through the experimental set-up (followed by filtering to reject the c.w. probe) in the case of the nonlinear waveguide either (i) substituted for an attenuator or (ii) kept in place.

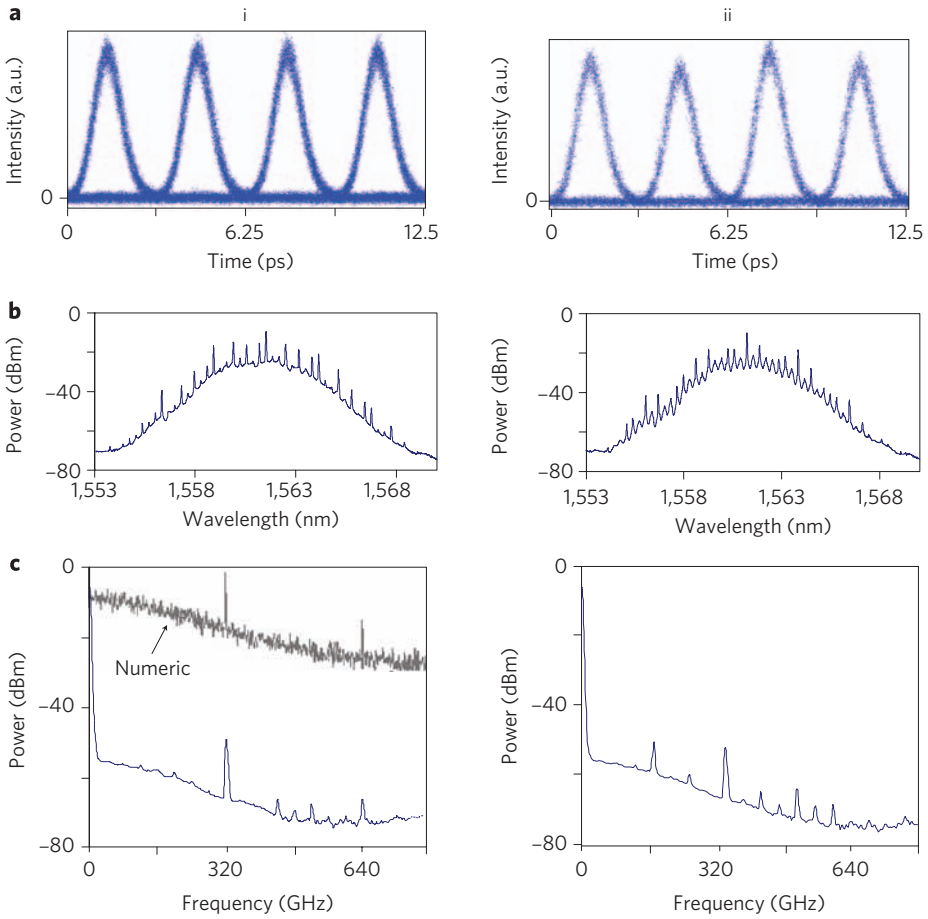

Figure 3 | Comparison of measurement data for 320 Gb s^{-1} signals. a–c, Output traces of 320 Gb s^{-1} test signals for (i) best and (ii) non-optimal MUX settings captured as signal 'eye diagrams' from high-resolution optical sampling scope (**a**), optical spectra from an OSA (**b**), and RF spectra from the PC-RFSA (**c**), with comparison to a numerically generated RF spectrum of an ideal 320 Gb s^{-1} optical signal (grey curve).

delay (DGD)[13]. These effects change the temporal waveform (and thus its RF spectrum), but not the optical spectrum. Figure 4 plots the power of the fundamental 320 GHz clock tone measured from the PC-RFSA as a function of both GVD and DGD. The result shows a large dynamic range in the measurement (up to ~20 dB), and compares well with numerical simulation by the split-step Fourier method[2] for the same parameters of both the signal and waveguide, highlighting the potential for this device to be used also for monitoring distortion in high-speed optical communication systems.

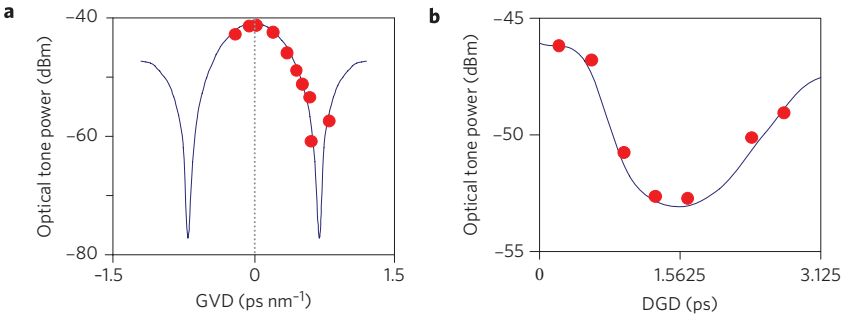

Figure 4 | Performance monitoring of 320 Gb s^{-1} signals using the PC-RFSA. a,**b**, A signal distorted by GVD (**a**) or DGD (**b**) affects the 320 GHz clock tone power measured from the PC-RFSA output (when fixed average input power is maintained) as plotted for experimental data (symbols) and numerical simulation (curves), which provides a calibrated reference for real-time performance monitoring.

Table 1 | Comparing the performance of nonlinear waveguides.

Waveguide	γ (W^{-1} km^{-1})	D (ps nm^{-1} km^{-1})	S (ps nm^{-2} km^{-1})	Bandwidth FOM (L_W/L_{NL})	Accuracy FOM (L_D/L_{NL})
ChG chip	7,250	40	0.73	103	85
Silica HNF	20	0.5	0.02	34	19
Silica DSF	3	0.5	0.08	5	2.8
Bi_2O_3 fibre	1,360	−260	—	2.6	2.4
ChG fibre	1,200	−560	—	1	1

ChG, chalcogenide; HNF, highly nonlinear silica fibre; DSF, dispersion-shifted fibre.
Calculated figures of merit (FOMs) for the measurement bandwidth and accuracy of all-optical RF spectrum analysers based on various types of $\chi^{(3)}$ nonlinear waveguides normalized to the ChG fibre for $\Delta\lambda = 20$ nm and fixed P_0 and T_0.

The performance advantages of the PC-RFSA stem from the combination of the waveguide's short length, highly nonlinearity and low dispersion. This enhances both the measurement bandwidth and colourless operation capability by reducing the dispersion-induced 'walk-off' delay[2] (ΔT) between the signal and probe arising from their mismatched group velocities associated with the nonzero D and their wavelength separation ($\Delta\lambda$). For a waveguide of length L, and D defined at λ_s, walk-off delay can be expressed approximately as $\Delta T = \Delta\lambda(2D - S\lambda)\Delta L/2$, where S is the dispersion slope, that is, the linear change of D with wavelength. Walk-off delay reduces the nonlinear interaction length, which for a signal pulse of width T_0 can be approximated as $L_W \approx 2T_0/|\Delta\lambda(2D - S\Delta\lambda)|$. Hence, the measurement bandwidth (Δf_{max}) of our 16-cm device (with $S = 0.73$ ps nm^{-2} km^{-1}) determined by considering a sine-wave input signal ($T_0 = 1/(2\Delta f_{max})$) at $\lambda_s = 1{,}550$ nm satisfying $L_W \gg 16$ cm is $\Delta f_{max} \ll 4.8$ THz, which is consistent with the experimental value.

A useful figure of merit (FOM) is the ratio of L_W to the nonlinear length $L_{NL} = 1/(\gamma P_0)$, which defines the length where the nonlinear phase shift induced becomes significant for an incident pulse peak power P_0. When $L_W/L_{NL} \approx 2\gamma P_0 T_0/|\Delta\lambda(2D - S\Delta\lambda)|$ is large, the impact of walk-off delay on XPM is reduced. Table 1 compares this FOM for various nonlinear waveguides, including a low-dispersion-slope silica HNF (ref. 19), silica dispersion-shifted fibre (DSF), and typical Bi_2O_3 and As_2Se_3 type HNF (ref. 7) in the case of $\Delta\lambda = 20$ nm. It shows that the ChG chip has the highest FOM, which means, in comparison to other waveguides of equal γL product, it will sustain the nonlinear interaction over the widest ranging $\Delta\lambda$, translating to the broadest measurement bandwidth. Its FOM could be even further increased by reducing D by optimizing the waveguide film thickness during fabrication[18]. Although silica HNF has near-zero dispersion, the actual zero dispersion wavelength is susceptible to temperature fluctuations of the fibre[19], as well as fluctuations along its length during manufacturing, restricting its FOM.

Our short, low-dispersive device also increases the measurement accuracy. This is evident from the pulse dispersion length[2] given by $L_D = T_0^2 2\pi c/(D\lambda_s^2)$ (where c is the speed of light), which defines the distance where pulse broadening becomes significant. The ChG chip satisfying $L_D \gg L$ ensures pulse distortion is negligible, as was observed experimentally for the 320 Gb s^{-1} signal through the PC-RFSA. Hence, for a 33% duty cycle signal of Gaussian pulses (that is, $T_0 = 1/(3 \times 1.665 \times R)$ at bit rate R), the maximum R ensuring high measurement accuracy for our 16-cm waveguide is $R_{max} \ll 2.2$ Tb s^{-1} (at 1,550 nm wavelength). It is also useful to contrast L_D with L_{NL} for different waveguides by the FOM $L_D/L_{NL} = \gamma P_0 T_0^2 2\pi c/(D\lambda_s^2)$. As shown in Table 1, the FOM is again highest for the ChG chip, which means, in comparison to other waveguides of equal γL product, it will induce the least broadening and thus distortion of the signal under test. An added advantage of lower dispersion is the prevention of signal distortion owing to SPM at higher signal powers, which then permits a larger input power to be used to achieve higher dynamic range in the measurement. Furthermore, calculations show that even when factoring in the predicted dispersion slope of 0.73 ps nm^{-2} km^{-1} at 1,550 nm, both R_{max} and Δf_{max} vary only marginally when λ_s is swept between 1,530 and 1,570 nm, highlighting the unique colourless advantage of the ChG chip. This enables high-performance monitoring over a broad range of signal channels rather than only those near the waveguide's zero-dispersion wavelength.

In conclusion, a photonic-chip-based all-optical RF spectrum analyser with measurement bandwidth exceeding 2.5 THz has been demonstrated for the first time using a dispersion-shifted As_2S_3 planar waveguide. The combined high nonlinearity and low dispersion in a short length device enabled greater measurement bandwidth, higher accuracy and colourless operation. The device was effectively used to characterize signals of very high bit rate (320 Gb s^{-1}) and to monitor distortions common in fibre-optic communications systems.

Methods

Waveguide fabrication. The waveguide was fabricated by thermally evaporating an 870-nm-thick film of As_2S_3 (refractive index $n \approx 2.4$ at 1,550 nm wavelength) on an oxidized silicon wafer ($n = 1.44$). From this, 16-cm-long ribs of width 3 and 4 μm were patterned using standard contact photolithography. Surrounding trenches were

then dry-etched 380 nm deep using inductively coupled plasma reactive ion etching[17]. After removing the photoresist, the chip was overclad with a UV cured inorganic polymer glass (RPO Pty Ltd IPG, $n = 1.53$ at 1,550 nm). The serpentine waveguides comprised three straight sections connected with two 180 ° bends of ~3-mm radii on a 6-cm-size chip. Its end facets were prepared by hand-cleaving the silicon substrate using a diamond scriber. Optical coupling into the waveguides was through a pair of lensed fibres with spot diameter of 2.5 μm. Their back-to-back coupling loss (without the waveguide) was 2.5 dB. The total insertion loss of the waveguide when coupling to the TM mode was 16 dB, comprising 0.5 dB cm^{-1} propagation loss and ~4 dB coupling loss per facet. Coupling to the transverse-electric (TE) mode achieved ~2 dB lower loss, but its dispersion was higher. The waveguide parameters A_{eff}, γ, D and S were determined from the numerically solved TM mode by using the finite-element method.

Signal generation. The 320 Gb s^{-1} transmitter used a mode-locked fibre laser (MLFL) and nonlinear (SPM based) pulse compressor comprising a 1-km silica HNF ($\gamma = 11.5$ W^{-1} km^{-1}, $D = -2.4$ ps nm^{-1} km^{-1} at 1,550 nm) followed by a 5-nm bandpass optical filter (BPF) and ~100 m of standard single-mode fibre to generate a 40 GHz pulse train of 1-ps pulses at a wavelength of 1,560 nm. These were then encoded with an on–off keyed signal using a Mach–Zehnder (MZ) modulator driven electrically by a 40 Gb s^{-1} pseudo-random bit sequence (PRBS) of $2^{31} - 1$ pattern length. Optical time-division multiplexing (MUX) in a three-stage fibre delay line interferometer of $2^7 - 1$ bit delay produced a 320 Gb s^{-1} signal.

PC-RFSA measurement implementation. The signal was boosted in an erbium-doped fibre amplifier (EDFA) and launched into the PC-RFSA with a c.w. probe at 1,545 nm wavelength, which was also separately amplified and filtered. Polarization controllers (PCs) were used to align the polarization states of the signal and probe so that they were aligned for maximum XPM in the waveguide and simultaneously coupled to the TM mode for lowest dispersion. A few metres of dispersion-compensating fibre was inserted after the MUX to compensate for dispersion within the transmitter to produce the optimized 320 Gb s^{-1} signal.

To test the PC-RFSA for monitoring signal distortion, a variable GVD up to ~1 ps nm^{-1} was applied to the signal by transmitting it through different lengths of standard single-mode fibre before reaching the PC-RFSA. This amount of dispersion caused severe distortion of the signal and closure of its eye diagram as observed from the optical sampling scope. By maintaining a constant average power of the input signal to the PC-RFSA, the peak intensity of the pulses entering the ChG chip decreased with increasing GVD. Similarly, DGD monitoring was tested using an emulator that degraded the signal by splitting it into two orthogonal linear polarization states with a relative delay offset that was programmable over the 3.125-ps bit period of the signal. The effect was a drop in peak intensity for fixed average input power. The PCs for the input signal and probe were kept at the same setting that maximized XPM and coupling to the waveguide TM mode when DGD was zero. Hence for nonzero DGD, the signal was simultaneously coupled to the TE mode. Despite this added complexity, the DGD of the 320 Gb s^{-1} signal was effectively monitored.

The measurement bandwidth of PC-RFSA was characterized using a sine-wave signal formed by the combined emission from two narrow-linewidth external-cavity c.w. lasers with a wavelength separation $\delta\lambda$ (centred at λ_s), creating an interference pattern of beat frequency Δf. Each laser was separately boosted in an EDFA, and then filtered by a 1-nm BPF before being combined using a 50 : 50 coupler. Their polarization states were aligned using PCs to maximize the sine-wave modulation depth. Another 50 : 50 coupler was used to combine the signal with a c.w. probe fixed at $\lambda_s = 1{,}530$ nm, which was separately boosted with an EDFA and filtered by a 0.6-nm BPF. Another PC was used to align its polarization state with that of the signal. Polarization states of both signal and probe were aligned to the TM mode of the waveguide. The maximum signal frequency was obtained for $\delta\lambda = 30$ nm, corresponding to 3.75 THz.

Received 24 September 2008; accepted 7 January 2009; published online 15 February 2009

References

1. Roberts, K. Electronic dispersion compensation beyond 10 Gb s^{-1}. *LEOS Summer Topical Meetings*, 9–10 (2007).
2. Agrawal, G. P. *Nonlinear Fiber Optics* 3rd edn (Academic Press, 2001).
3. Ta'eed, V. G. *et al.* Self-phase modulation-based integrated optical regeneration in chalcogenide waveguides. *IEEE J. Sel. Top. Quant.* **12,** 360–370 (2006).
4. Salem, R. *et al.* Signal regeneration using low-power four-wave mixing on silicon chip. *Nature Photon.* **2,** 35–38 (2008).
5. Yamada, K. *et al.* All-optical efficient wavelength conversion using silicon photonic wire waveguide. *IEEE Photon. Technol. Lett.* **18,** 1046–1048 (2006).
6. Olsson, B.-E., Ohlen, P., Rau, L. & Blumenthal, D. J. A simple and robust 40 Gb s^{-1} wavelength converter using fiber cross-phase modulation and optical filtering. *IEEE Photon. Technol. Lett.* **12,** 846–848 (2000).
7. Ta'eed, V. G. *et al.* Error free all optical wavelength conversion in highly nonlinear As–Se chalcogenide glass fiber. *Opt. Express* **14,** 10371–10376 (2006).
8. Tangdiongga, E. *et al.* All-optical demultiplexing of 640 to 40 Gbits s^{-1} using filtered chirp of a semiconductor optical amplifier. *Opt. Lett.* **32,** 835–837 (2007).
9. Li, J., Olsson, B. E., Karlsson, M. & Andrekson, P. A. OTDM demultiplexer based on XPM-induced wavelength shifting in highly nonlinear fiber. *IEEE Photon. Technol. Lett.* **15,** 1770–1772 (2003).
10. Ayotte, S., Xu, S., Rong, H., Cohen, O. & Paniccia, M. J. Dispersion compensation by optical phase conjugation in silicon waveguide. *Electron. Lett.* **43,** 1037–1039 (2007).
11. Kilper, D. C. *et al.* Optical performance monitoring. *J. Lightwave Technol.* **22,** 294–304 (2004).
12. Luo, T. *et al.* All-optical chromatic dispersion monitoring of a 40 Gb s^{-1} RZ signal by measuring the XPM-generated optical tone power in a highly nonlinear fiber. *IEEE Photon. Technol. Lett.* **18,** 430–432 (2006).
13. Blows, J. L., Hu, P. & Eggleton, B. J. Differential group delay monitoring using an all-optical signal spectrum-analyser. *Opt. Commun.* **260,** 288–291 (2006).
14. Westbrook, P. S., Her, T. H., Eggleton, B. J., Hunsche S. & Raybon, G. Measurement of pulse degradation using all-optical 2R regenerator. *Electron. Lett.* **38,** 1193–1194 (2002).
15. Witte, R. A. *Spectrum and Network Measurements* (Prentice Hall, 1993).
16. Dorrer, C. & Maywar, D. N. RF spectrum analysis of optical signals using nonlinear optics. *J. Lightwave Technol.* **22,** 266–274 (2004).
17. Madden, S. J. *et al.* Long, low loss etched As_2S_3 chalcogenide waveguides for all-optical signal regeneration. *Opt. Express* **15,** 14414–14421 (2007).
18. Lamont, M. R. E., Martijn de Sterke, C. & Eggleton, B. J. Dispersion engineering of highly nonlinear As_2S_3 waveguides for parametric gain and wavelength conversion. *Opt. Express* **15,** 9458–9463 (2007).
19. Takahashi, M. *et al.* Low-loss and low-dispersion-slope highly nonlinear fibers. *J. Lightwave Technol.* **23,** 3615–3624 (2005).

Acknowledgements

This work was in part supported by the Australian Research Council (ARC) through its ARC Centres of Excellence and Federation Fellowship programs.

Author contributions

All authors have contributed to this paper and agreed on the content.

Additional information

Reprints and permission information is available online at http://npg.nature.com/reprintsandpermissions/. Correspondence and requests for materials should be addressed to M.P.

nature photonics

LETTERS

PUBLISHED ONLINE: 22 FEBRUARY 2009 | DOI: 10.1038/NPHOTON.2009.2

STED microscopy reveals crystal colour centres with nanometric resolution

Eva Rittweger†, Kyu Young Han†, Scott E. Irvine†, Christian Eggeling and Stefan W. Hell*

Because they have spin states that can be optically polarized and detected, fluorescent nitrogen vacancies in diamond[1–3] have considerable potential for applications in quantum cryptography[4,5] and computation[6–8], as well as for nanoscale magnetic imaging[9,10] and biolabelling[11,12]. However, their optical detection and control are hampered by the diffraction resolution barrier of far-field optics. Here, we show that stimulated emission depletion (STED) microscopy[13,14] is capable of imaging nitrogen-vacancy centres with nanoscale resolution and Ångström precision using focused light. The far-field optical control of the population of their excited state at the nanoscale expands the versatility of these centres and demonstrates the suitability of STED microscopy to image dense colour centres in crystals. Nitrogen-vacancy defects show great potential as tags for far-field optical nanoscopy[15] because they exhibit nearly ideal STED without bleaching. Measured point-spread functions of 5.8 nm in width demonstrate an all-physics-based far-field optical resolving power exceeding the wavelength of light by two orders of magnitude.

For many decades, diffraction precluded far-field optical imaging with resolution better than half the wavelength of light. This limit has been overcome with the advent of STED microscopy, which is a lens-based fluorescence microscope with a resolution conceptually no longer limited by diffraction[13,16,17]. In brief, a STED microscope separates two or more adjacent objects by ensuring that only one of them fluoresces at a time. Sequential object signalling is accomplished by transiently switching the objects off by stimulated emission.

STED microscopy has so far provided a resolution of 16–80 nm, which has been used for mapping proteins in cells[18], and for the real-time imaging of colloidal particles or synaptic vesicles in living neurons[19]. The fluorescent markers used were organic molecules or fluorescent proteins having a singlet ground state (S_0) and a first excited state (S_1), each with vibrational sublevels. Once excited, these molecules equilibrate to the lowest vibrational sublevel of the S_1 state, from where they can return to a vibrational sublevel of the S_0 state by fluorescence emission after an average period τ_{fl}. Alternatively, the so-called STED beam switches the molecules off by forcing them down to the S_0 state. This occurs if the stimulated emission rate $\sigma I_{STED}\lambda_{STED}/hc$ is much larger than that of the spontaneous decay, $1/\tau_{fl}$, where σ is the cross-section for stimulated emission, h is Planck's constant, c is the speed of light in vacuum, and I_{STED} is the STED beam intensity. The wavelength λ_{STED} is chosen such that the fluorophore is pumped into a rapidly decaying higher vibrational sublevel of the S_0 state, which makes de-excitation predominant. If we neglect polarization, the ability of the molecule to fluoresce decreases in proportion to $\exp(-I_{STED}/I_S)$ where I_S is a fluorophore characteristic[17]. Hence, for $I_{STED} \geq 3I_S$ the fluorophore is essentially switched off.

Organic fluorophores follow such switching, but have the disadvantage of suffering from bleaching and blinking, making solid-state-based fluorophores very appealing. It is also interesting, however, to explore applications of far-field optical nanoscopy to transparent solids. Luminescent transitions arising from defects in diamond, particularly nitrogen-vacancy centres composed of a substitution nitrogen next to a charged vacancy (Fig. 1a), have attracted much attention[2,20]. Absorption at 532 nm elevates them from their ground (^{3}A) state to an excited (^{3}E) state of $\tau_{fl} = 11.6$ ns lifetime, which emits at 600–850 nm with virtually no bleaching or blinking. Phononic coupling yields a pronounced Stokes shift, but the involved states are now spin triplets. Centres with magnetic quantum number $m_s = 0$ emit more strongly, because their $m_s = \pm 1$ counterparts have an increased tendency to convert into a dark singlet state (^{1}E), ultimately yielding ground-state centres with $m_s = 0$, a feature that allows for the orientation and detection of spin by illumination[2,20]. When used as scanning tips, nitrogen-vacancy centres in nanosized diamonds provide optical[21] and magnetic imaging[9,10], but the prospect of reading and controlling individual defects at the nanoscale with conventional lenses is very attractive.

We therefore investigated STED on nitrogen-vacancy defects within diamonds of type IIa grown by chemical vapour deposition. Excitation at 532 nm was achieved using a 60-ps pulsed laser diode, which was triggered by the pulses of the STED beam provided by a laser system operating at $\lambda_{STED} = 775 \pm 1$ nm and emitting 3.2 ns pulses at 8 MHz. The synchronized pulses were combined using

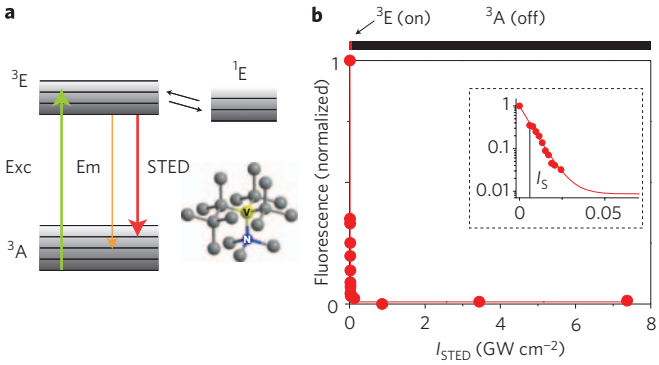

Figure 1 | Stimulated emission depletion of the excited state 'switches off' a charged nitrogen-vacancy colour centre by light. a, Energy diagram sketching the ground (^{3}A), fluorescent (^{3}E) and the dark singlet state (^{1}E) along with excitation (Exc), emission (Em) and stimulated emission (STED) transitions in nitrogen-vacancy centres. **b**, The steep ('rectangular') fluorescence depletion curve showing the abrupt decrease of the population of ^{3}E with intensity I_{STED} facilitates a nearly perfect implementation of STED. The inset representation confirms the exponential suppression of the excited state. For $I_{STED} > 20$ MW cm^{-2}, the centre is deprived of its ability to fluoresce (switched off).

Department of NanoBiophotonics, Max Planck Institute for Biophysical Chemistry, Am Fassberg 11, 37077 Göttingen, Germany; †These authors contributed equally to this work; *e-mail: shell@gwdg.de

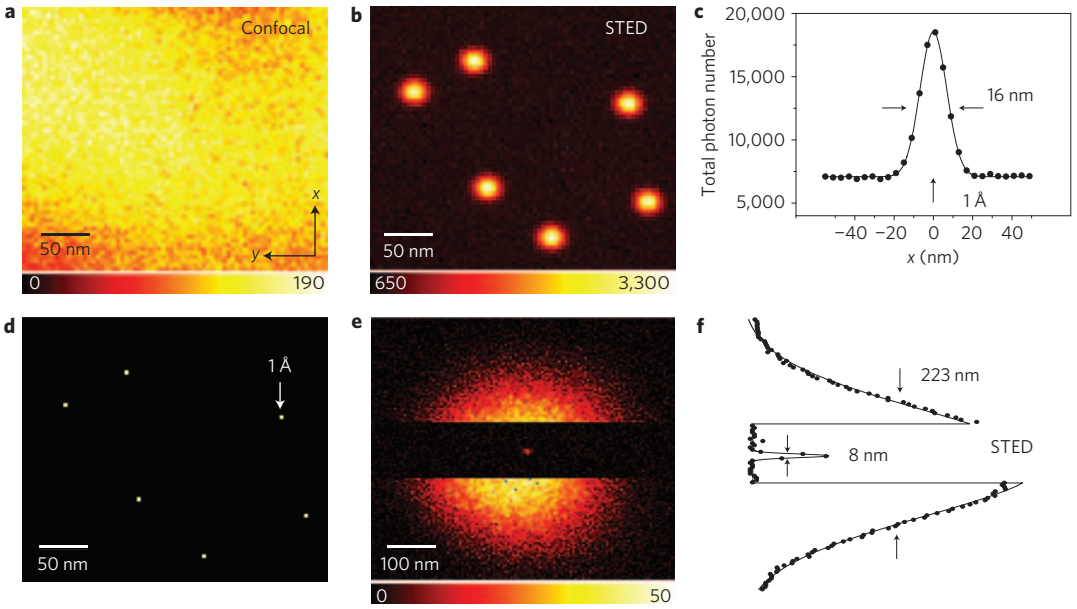

Figure 2 | Stimulated emission depletion microscopy reveals densely packed nitrogen-vacancy centres in diamond. a,**b**, Confocal (**a**) and STED (**b**) images from the same crystal region. **c**, The individual centres resolved in **b** automatically yield the effective PSF of the STED recording whose *y*-profile exhibits a FWHM of $\Delta y = 16.0$ nm. **d**, The coordinate of each centre can be calculated with 0.14 nm precision. Comparing **a** with **d** highlights the dramatic gain in information resulting from the unique increase in resolution. **e**,**f**, Applying $I_{STED}^{max} = 3.7$ GW cm^{-2} shrinks a confocal spot of 223 nm diameter (FWHM) down to 8 nm. Note that the increase in resolution is a purely physical phenomenon.

dichroic mirrors and collinearly directed through a 1.46 numerical aperture (NA) oil immersion lens, which also imaged the fluorescence onto the confocally arranged aperture of a counting avalanche photodiode.

The phononic coupling in the ^{3}A state enables quenching of excited nitrogen-vacancy centres by stimulated emission. This is demonstrated in Fig. 1b, which shows the fluorescence of a single centre as a function of I_{STED}, here defined as the peak intensity in the focal plane. The time-averaged power of the excitation light was 40 μW. A steep exponential drop of the fluorescence with I_{STED} is observed, as one would anticipate for perfect STED (ref. 13). Extracting $I_S = 6.6$ MW cm^{-2} yields $\sigma = 1.2 \times 10^{-17}$ cm^2, which agrees with the value determined from the emission spectrum. The main outcome, however, is that the nitrogen-vacancy centres can be sharply switched off by light (Fig. 1b).

To make use of this nearly 'rectangular' depletion curve[13] for nanoscopy, we produced a doughnut-shaped focal intensity distribution[22] $I_{STED}^{d}(x,y)$ with a central minimum $I_{STED}^{min}(0,0) \approx 0$. The minimum is ideally zero, but in practice it amounts to a fraction $\varepsilon \ll 1$ of the maximum intensity at the doughnut crest: $I_{STED}^{min} = \varepsilon \max[(I_{STED}^{d}(x,y)]$. Overlapping the Airy disk of the excitation beam with the doughnut and enforcing $I_{STED}^{max} \gg I_S$ switched off all the centres covered by the Airy disk except for those at the doughnut minimum where $I_{STED}^{d}(x,y) \leq 3I_S$. Therefore, the Airy disk can be ignored when calculating the spot in which the centres can still be 'on', that is, the effective point-spread function (PSF) of the system. It is described by the function $\exp(-I_{STED}^{d}(x,y)/I_S)$ having a full-width at half-maximum (FWHM) of $\Delta x,y \approx \lambda_{STED}/\sqrt{(CI_{STED}^{max}/I_S)}$, with the constant C depending on the shape of the minimum[22]. Although the resolution $\Delta x,y$ scales with the wavelength, adjusting $I_{STED}^{max} \gg I_S$ squeezes the PSF continuously, indicating that the wavelength has surrendered its limiting role.

We imaged by scanning the sample with respect to the beams using a three-dimensional piezo stage (Physik Instrumente, P-733.3DD) with 0.1 nm positional accuracy and 0.03% linearity. Figure 2 compares a confocal image (Fig. 2a) with the corresponding STED image (Fig. 2b), taken at $I_{STED}^{max} = 1.4$ GW cm^{-2}. Although the confocal reference lacks any detail, its STED counterpart resolves each nitrogen-vacancy defect. The similar brightness and sparse occurrence of the dots shown in the crystal allow us to conclude that they represent single nitrogen-vacancy defects. The images consist of 75 × 65 pixels of 4 × 4 nm in size, recorded with a dwell time of 5 ms. To reduce statistical error (number of counts given in the colour table), the displayed and analysed STED image comprises the sum of 97 consecutively recorded images. Representing the effective PSF, the images of individual centres reveal $\Delta x = 18.3$ nm and $\Delta y = 16.0$ nm as the resolution under the conditions used. Note that the resolution gain derives just from the optical preparation of the states.

The STED recording inherently resolves individual nitrogen-vacancy centres because they are all further apart from each other than Δx or Δy. An important insight is that, when scanned over the sample together with the excitation beam, the doughnut-shaped STED beam allows only a single nitrogen-vacancy centre to fall within the doughnut minimum; all others are switched off or simply not excited. Thus STED nitrogen-vacancy centres are resolved individually and hence registered sequentially in time.

Once all the centres are resolved, increasing the resolution further is no longer required. Their position can be calculated from the centroid of their subdiffraction-sized spot[23]. The precision of this calculation depends on the effective PSF, the number of collected photons and the background[24,25]. We measured a spatially homogeneous background of 1.6 counts ms^{-1} throughout the imaged region, as indicated in the images. Under these conditions and the assumption (here not made or asserted) that scanning errors are negligible, the *xy*-coordinates of each centre can be derived with 1–2 Å precision; that is, by three orders of magnitude below the diffraction limit (Fig. 2d). The information provided in Fig. 2d should be contrasted with that contained in the confocal recording (Fig. 2a), which fails to render any information about the number and location of the colour centres. The distance between the centres in the upper left corner projected in the *xy*-plane is 67.9 ± 0.1 nm. By extending STED into the third dimension, one can also incorporate depth information. Thus, provided

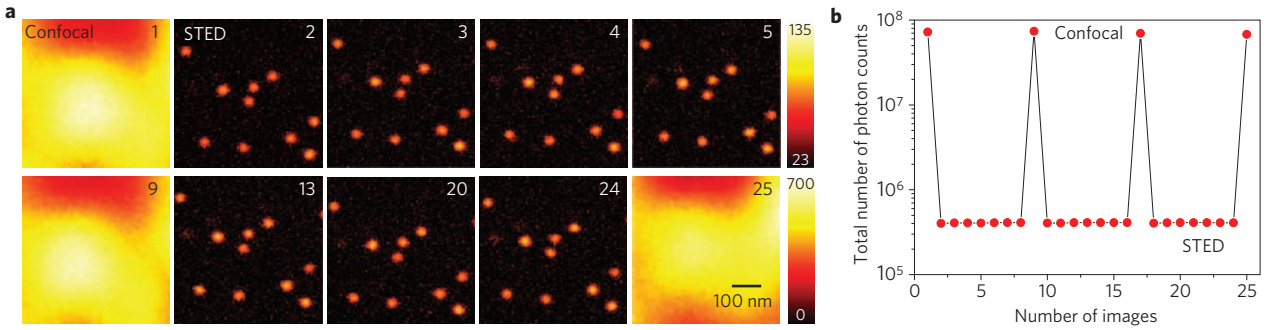

Figure 3 | STED microscopy without photobleaching. a, Consecutive confocal and STED recordings (as indicated) of the same crystal region. **b**, The total fluorescence signal in each image frame, showing virtually no change in brightness and in resolution (here <25 nm) with increasing number of recordings. The recording time for all images was the same, causing the STED images to be darker approximately by the (here ~100-fold) reduction in focal area. Importantly, the peak brightness of single centres is virtually equal in the STED and confocal recordings. Note the absence of blinking. The experiment demonstrates far-field optical nanoscopy recording without photobleaching.

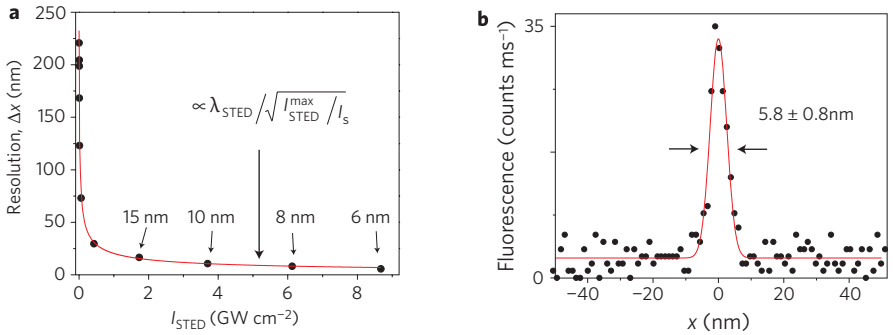

Figure 4 | Maximizing the resolving power by optimizing STED in a single direction. a, The measured decrease of the lateral FWHM Δx from 223 nm down to 6 nm scales inversely with the square-root of the intensity of the STED beam (red line). Note that all data were taken from the same single nitrogen-vacancy defect. **b**, A line profile of the effective PSF along the *x*-axis, demonstrating an unprecedented all-physics-based far-field optical resolving power of 5.8 ± 0.8 nm.

that care is exerted to avoid scanning distortions and drift, STED microscopy is able to map nitrogen-vacancy centres with nanometric resolution and subnanometre precision.

Figure 2e shows a confocal image of an isolated nitrogen-vacancy centre, but near its middle, the STED beam is momentarily engaged. Applying $I_{\mathrm{STED}}^{\mathrm{max}} = 3.7$ GW cm^{-2} produced a spot of 8 nm FWHM. In this case, the peak is also reduced by 3.5-fold, which is due to the nonzero doughnut minimum $I_{\mathrm{STED}}^{\mathrm{min}}(0,0) = \varepsilon I_{\mathrm{STED}}^{\mathrm{max}}$ suppressing the peak by $\exp(-\varepsilon I_{\mathrm{STED}}^{\mathrm{max}}/I_{\mathrm{S}})$. Clearly, such peak reductions become important at large $I_{\mathrm{STED}}^{\mathrm{max}}$ and therefore at high resolution. Evaluation of the measurement using Fig. 1b yields $\varepsilon = 7 \times 10^{-4}$, which is due to doughnut imperfections. Note that the effective focal area decreases by a factor of 777.

Importantly, the outstanding photostability of nitrogen-vacancy centres[1] is maintained under the intense STED beams, as made evident in consecutive STED recordings (Fig. 3) in which both the brightness and the tenfold resolution increase remain unchanged. Demonstrating optical nanoscopy without photobleaching, Fig. 3 highlights that with diamond nanoparticles as markers[11,12], STED will enable the use of (biological) fluorescence nanoscopy with countless recordings.

Recording images similar to those in Figs 2 and 3 is impractical with near-field optics, because, being located more than 2–3 μm beneath the surface of the crystal, the colour centres cannot be accessed by a tip. Besides being noninvasive and able to access the interior of the crystal, compared to near-field optics, STED microscopy is easier to put into practice, control and operate, and provides substantially higher resolution. Likewise, alternative nanoscopy strategies that sparsely switch individual emitters (from a dark state to a state emitting a bunch of photons allowing their localization[26–29]) are hard to implement for nitrogen-vacancy colour centres, because at room temperature, blinking or metastable switching between a bright and a dark state is nearly absent. Hence, nitrogen-vacancy centres are ideal for STED and STED is ideal for their imaging. This is likely to apply to many other colour centres in crystals.

Next we used a focal STED beam spot with a *y*-oriented central zero-line with steep peaks $I_{\mathrm{STED}}^{\mathrm{max}}$ along the *x*-axis[16]. Increasing $I_{\mathrm{STED}}^{\mathrm{max}}$ to 8.6 GW cm^{-2} squeezes the FWHM of the PSF from $\Delta x = 223$ nm down to 6 nm (Fig. 4a). The increase in resolution follows the anticipated inverse square-root law[15,16]. An exemplary super-resolved PSF of a single nitrogen-vacancy centre is shown in Fig. 4b and has a measured $\Delta x = 5.8 \pm 0.8$ nm. This value is 133-fold below the responsible wavelength and represents a new regime of obtainable all-physics-based resolution using conventional optics.

Despite the leaps and bounds STED microscopy has made, its limits have not yet been reached. Applying a shorter λ_{STED} entailing a larger σ should decrease Δx,Δy even further. Implemented with a deep zero ($\varepsilon \ll 1 \times 10^{-4}$), the initially desired nearly 'rectangular' depletion curve[13] should enable a further 'spot sharpening' by more than a factor of 10, which may surpass the dimensions of the electron cloud and, leaving the dipole approximation behind, open up the fascinating prospect of sensing the (size of the) cloud and its immediate environment. It would also be desirable to investigate STED on nitrogen-vacancy centres subject to magnetic and microwave fields. In particular, reading out nitrogen-vacancy centres and hence local magnetic fields on the nanoscale should be easier

with STED and conventional lenses than with nanosized optical tips. Thus, STED microscopy may greatly simplify magnetic imaging at the nanoscale[9,10]. Likewise it will be interesting to apply STED nanoscopy to other colour centres and crystals. Finally, the achieved and future gains in all-physics-based resolution should stimulate novel explorations in applied and fundamental (quantum) optics.

Methods

The cylindrical doughnut focal spot used for generating the data of Figs 2 and 3 was produced by inserting a glass waveplate (RPC Photonics), inducing an azimuthal linear helical phase ramp from 0 to 2π on the initially flat wavefront of the STED beam. In these experiments both the excitation and the STED beam were circularly polarized. The bandwidth of the STED beam was <10 GHz.

The data of Fig. 4 were produced with linearly polarized excitation and STED beams. A phase shift of π, resulting in the *y*-oriented line-shaped valley, was produced by inserting a home-built phase-shifter consisting of tilted optical flats. In this case, the polarization of both beams was oriented along the direction of the line-shaped valley. Images in Fig. 2a,b were taken from a diamond sample with a higher density of nitrogen-vacancy centres than the crystal used for the measurements shown in Figs 2e and 4a,b.

The intensity values refer to spatial and temporal peak intensities assuming aberration-free focusing and rectangular laser pulses, with the transmission of the objective lens 70% at 775 nm. A 95% transmission was assumed at the interface between the immersion oil and the diamond crystal. In all recordings, background noise was reduced to 120 counts s^{-1} by gated detecting within a 40-ns window after the STED pulse.

The stimulated emission cross-section was calculated using $\sigma \equiv hc/(\lambda_{STED} I_S \tau_p)$ under the approximation that the change in population of the excited state of the nitrogen-vacancy centre was negligible during the duration τ_p of the STED pulse. The cross-section was also derived from the emission spectrum $E(\lambda)$ of a single defect normalized to the quantum yield[3,30] ($Q = 0.7 = \int E(\lambda)\, d\lambda$) using $\sigma = \lambda^4 E(\lambda)/8\pi c n^2 \tau_{fl}$, with the speed of light in vacuum c and the refractive index of diamond $n = 2.417$.

The STED image of Fig. 2b was generated by summing 97 STED images of the same region. Alignment was ensured by introducing subpixel translational shifts to maximize the spatial correlation between the images. This corrects exclusively translational drift between consecutive images. The central positions of the defects in the registered images were stochastically distributed with a variance close to the expected localization accuracy, supporting the notion that no further substantial corrections were required in this case. The centroids were determined by Gaussian fits.

Data points within Fig. 4a were fitted with the general expression[22] $\Delta x \approx x_c / \sqrt{(1 + x_c^2 a^2 I_{STED}^{max} / (I_S \ln 2))}$, where x_c is the FWHM for $I_{STED}^{max} = 0$ and a is the steepness of the STED intensity pattern $I_{STED}(x) \equiv 4 I_{STED}^{max} a^2 x^2$, giving $a = 1.76\ \lambda/NA$. The measured STED PSF independently yielded a steepness $a = 1.75\ \lambda/NA$. The line profile of Fig. 4b represents eight consecutive *x*-scans over the same nitrogen-vacancy defect, revealing an average measured FWHM of the scans of 5.8 nm, with a standard deviation of 0.8 nm.

Received 6 November 2008; accepted 20 January 2009; published online 22 February 2009

References

1. Gruber, A. *et al.* Scanning confocal optical microscopy and magnetic resonance on single defect centers. *Science* **276,** 2012–2014 (1997).
2. Jelezko, F. & Wrachtrup, J. Single defect centres in diamond: a review. *Phys. Status Solidi A* **203,** 3207–3225 (2006).
3. Wrachtrup, J. & Jelezko, F. Processing quantum information in diamond. *J. Phys. Condens. Matter* **18,** S807–S824 (2006).
4. Kurtsiefer, C., Mayer, S., Zarda, P. & Weinfurter, H. Stable solid-state source of single photons. *Phys. Rev. Lett.* **85,** 290–293 (2000).
5. Beveratos, A. *et al.* Single photon quantum cryptography. *Phys. Rev. Lett.* **89,** 187901 (2002).
6. Gaebel, T. *et al.* Room-temperature coherent coupling of single spins in diamond. *Nature Phys.* **2,** 408–413 (2006).
7. Gurudev Dutt, M. V. *et al.* Quantum register based on individual electronic and nuclear spin qubits in diamond. *Science* **316,** 1312–1316 (2007).
8. Hanson, R., Dobrovitski, V. V., Feiguin, A. E., Gwyat, O. & Awschalom, D. D. Coherent dynamics of a single spin interacting with an adjustable spin bath. *Science* **320,** 352–355 (2008).
9. Balasubramanian, G. *et al.* Nanoscale imaging magnetometry with diamond spins under ambient conditions. *Nature* **455,** 648–651 (2008).
10. Maze, J. R. *et al.* Nanoscale magnetic sensing with an individual electronic spin in diamond. *Nature* **455,** 644–647 (2008).
11. Fu, C. C. *et al.* Characterization and application of single fluorescent nanodiamonds as cellular biomarkers. *Proc. Natl Acad. Sci. USA* **104,** 727–732 (2007).
12. Chao, J. I. *et al.* Nanometer-sized diamond particle as a probe for biolabeling. *Biophys. J.* **93,** 2199–2208 (2007).
13. Hell, S. W. & Wichmann, J. Breaking the diffraction resolution limit by stimulated emission: stimulated emission depletion fluorescence microscopy. *Opt. Lett.* **19,** 780–782 (1994).
14. Klar, T. A. & Hell, S. W. Subdiffraction resolution in far-field fluorescence microscopy. *Opt. Lett.* **24,** 954–956 (1999).
15. Hell, S. W. Toward fluorescence nanoscopy. *Nature Biotechnol.* **21,** 1347–1355 (2003).
16. Westphal, V. & Hell, S. W. Nanoscale resolution in the focal plane of an optical microscope. *Phys. Rev. Lett.* **94,** 143903 (2005).
17. Dyba, M. & Hell, S. W. Focal spots of size $\lambda/23$ open up far-field fluorescence microscopy at 33 nm axial resolution. *Phys. Rev. Lett.* **88,** 163901 (2002).
18. Donnert, G. *et al.* Macromolecular-scale resolution in biological fluorescence microscopy. *Proc. Natl Acad. Sci. USA* **103,** 11440–11445 (2006).
19. Westphal, V. *et al.* Video-rate far-field optical nanoscopy dissects synaptic vesicle movement. *Science* **320,** 246–249 (2008).
20. Manson, N. B., Harrison, J. P. & Sellars, M. J. Nitrogen-vacancy center in diamond: Model of the electronic structure and associated dynamics. *Phys. Rev. B* **74,** 104303 (2006).
21. Kühn, S., Hettich, C., Schmitt, C., Poizat, J. P. H. & Sandoghdar, V. Diamond colour centres as a nanoscopic light source for scanning near-field optical microscopy. *J. Microsc.* **202,** 2–6 (2001).
22. Harke, B. *et al.* Resolution scaling in STED microscopy. *Opt. Express* **16,** 4154–4162 (2008).
23. Heisenberg, W. *The Physical Principles of the Quantum Theory* (Chicago Univ. Press, 1930).
24. Bobroff, N. Position measurement with a resolution and noise-limited instrument. *Rev. Sci. Instrum.* **57,** 1152–1157 (1986).
25. Yildiz, A. *et al.* Myosin V walks hand-over-hand: single fluorophore imaging with 1.5-nm localization. *Science* **300,** 2061–2065 (2003).
26. Gordon, M. P., Ha, T. & Selvin, P. R. Single-molecule high-resolution imaging with photobleaching. *Proc. Natl Acad. Sci. USA* **101,** 6462–6465 (2004).
27. Betzig, E. *et al.* Imaging intracellular fluorescent proteins at nanometer resolution. *Science* **313,** 1642–1645 (2006).
28. Rust, M. J., Bates, M. & Zhuang, X. Sub-diffraction-limit imaging by stochastic optical reconstruction microscopy (STORM). *Nature Meth.* **3,** 793–796 (2006).
29. Fölling, J. *et al.* Fluorescence nanoscopy by ground-state depletion and single-molecule return. *Nature Meth.* **5,** 943–945 (2008).
30. Rittweger, E., Rankin, B. R., Westphal, V. & Hell, S. W. Fluorescence depletion mechanisms in super-resolving STED microscopy. *Chem. Phys. Lett.* **442,** 483–487 (2007).

Acknowledgements

We acknowledge motivating discussions with R. Walsworth and M. Lukin about magnetic imaging and also with F. Jelezko, who provided us with the nitrogen-vacancy diamond crystals. Furthermore, we thank A. Schönle for support with the software ImSpector, and J. Keller and M. Lauterbach for help with data analysis software. S.E.I. and K.Y.H gratefully acknowledge support from the Natural Sciences and Engineering Research Council of Canada and from the Korea Research Foundation Grant funded by the Korean Government (MOEHRD), respectively. K.Y.H. is on leave from the Department of Chemistry, Seoul National University, Korea.

Additional information

Reprints and permission information is available online at http://npg.nature.com/reprintsandpermissions/. Correspondence and requests for materials should be addressed to S.W.H.

nature photonics

LETTERS

PUBLISHED ONLINE: 22 FEBRUARY 2009 | DOI: 10.1038/NPHOTON.2009.3

A metamaterial solid-state terahertz phase modulator

Hou-Tong Chen[1]*, Willie J. Padilla[2], Michael J. Cich[3], Abul K. Azad[1], Richard D. Averitt[4] and Antoinette J. Taylor[1]

Over the past two decades, terahertz time-domain spectroscopy[1] and quantum-cascade lasers[2] have been two of the most important developments in terahertz science and technology. These technologies may contribute to a multitude of terahertz applications that are currently under investigation globally[3]. However, the devices and components necessary to effectively manipulate terahertz radiation require substantial development beyond what has been accomplished to date. Here we demonstrate an electrically controlled planar hybrid metamaterial device that linearly controls the phase of terahertz radiation with constant insertion loss over a narrow frequency band. Alternatively, our device may operate as a broadband terahertz modulator because of the causal relation between the amplitude modulation and phase shifting. We perform terahertz time-domain spectroscopy, in which our hybrid metamaterial modulator replaces a commercial mechanical optical chopper, demonstrating comparable broadband performance and superior high-speed operation.

The controllable properties of engineered metamaterials facilitate novel opportunities for manipulating electromagnetic radiation[4]. Electromagnetic phenomena achieved with metamaterials include negative index of refraction[5,6], super-resolution in optical imaging[7,8], and electromagnetic invisibility[9]. The resonant electromagnetic response originates from patterned metallic subwavelength structures, in which the dimensions can be appropriately scaled to operate at terahertz frequencies[10,11] where natural material response is somewhat rare. As such, metamaterials provide the basis for the construction of novel terahertz devices. Terahertz metamaterial devices have been demonstrated as state-of-the-art frequency-agile far-infrared filters[12,13], all-optical switches and modulators[14,15], and perfect absorbers[16,17]. Room-temperature, voltage-controlled metamaterial devices consisting of a single unit cell layer in the propagation direction have also been shown and are of particular interest here[18,19].

Despite the rapid progress in terahertz technology generally, a component largely unavailable as yet is an efficient terahertz phase shifter. Its counterparts at microwave and optical frequencies have many important applications, including, for example, phased array antennas and high-speed Mach–Zehnder modulators. However these configurations are, in general, difficult to extend to the terahertz regime. There have been a few attempts to demonstrate terahertz phase shifters, including using semiconductor quantum-well structures at cryogenic temperatures[20,21], or liquid crystals with very low speed[22]. The single-layer planar hybrid metamaterial phase modulator presented in this paper overcomes these shortcomings. Although phase shifting of terahertz radiation may be inferred from our earlier work[13,18], where frequency tuning of a metamaterial resonance and amplitude modulation were reported, phase modulation was not explicitly discussed or explored. Here we present the first experimental demonstration of a room-temperature solid-state phase modulator at terahertz frequencies as well as an investigation of its potential applications. Our new device achieves a voltage-controlled linear phase shift of $\sim\pi/6$ radians at 16 V. Moreover, the causal relation between amplitude switching and phase shifting enables broadband modulation.

A single unit cell of the device is illustrated schematically in Fig. 1a. Metallic electric split-ring resonators (SRRs)[23] were patterned to form a square array and connected by metal wires. They were fabricated on a 1-μm-thick epitaxial *n*-doped GaAs layer with an electron density of $2 \times 10^{16}\,\mathrm{cm}^{-3}$ grown on an intrinsic GaAs wafer. The SRRs and semiconductor form the Schottky diode structure that can, upon application of an external voltage, actively modify the depletion zone (see Supplementary Information). The control of the carrier density in the depletion zone permits tuning of the local dielectric properties near the gaps of the SRRs. This results in changes of the transmission (amplitude, phase, or both) of the metamaterial device. The micro-fabrication of the device has been described previously[18,19]; an optical microscopy image is shown in Fig. 1b. For this design, the SRR gaps are located at the four outer corners and are directly connected to the ohmic contact through the *n*-GaAs epilayer. This maximizes depletion of electrons near the metamaterial gaps upon application of bias voltage, which is essential to control the metamaterial resonances. In an earlier metamaterial switch[18], the split gap was located at the centre of an electric SRR and was surrounded by a closed outer ring. This reduced the voltage available for effective charge depletion within the split gap, which limited device performance. (See Supplementary Information for further details of the device.)

Conventional terahertz time-domain spectroscopy[24] (see Supplementary Information) was used to characterize the device. Resonances at 0.81 and 1.7 THz (driven by the electrical component of the terahertz radiation as indicated in Fig. 1b) are obtained as shown in Fig. 2a and b. The resonance at 0.81 THz arises from the individual SRRs and is due to the inductive–capacitive coupling of the circulating currents (Fig. 1c), while the resonance at 1.7 THz originates from a collective dipolar resonance (Fig. 1d), where the resonance frequency also depends on the SRR periodicity[25]. At zero voltage bias the resonances are weak because carriers in the substrate shunt the metamaterial capacitive gaps, thereby damping the response. Under reverse bias voltage an increase in depletion occurs, reducing the damping and causing an increase in oscillator strength for both resonances. The depletion near the split gaps plays

[1]Center for Integrated Nanotechnologies, Materials Physics & Applications Division, Los Alamos National Laboratory, Los Alamos, New Mexico 87545, USA, [2]Department of Physics, Boston College, 140 Commonwealth Avenue, Chestnut Hill, Massachusetts 02467, USA, [3]Sandia National Laboratories, MS1085, Albuquerque, New Mexico 87185, USA, [4]Department of Physics, Boston University, 590 Commonwealth Avenue, Boston, Massachusetts 02215, USA; *e-mail: chenht@lanl.gov

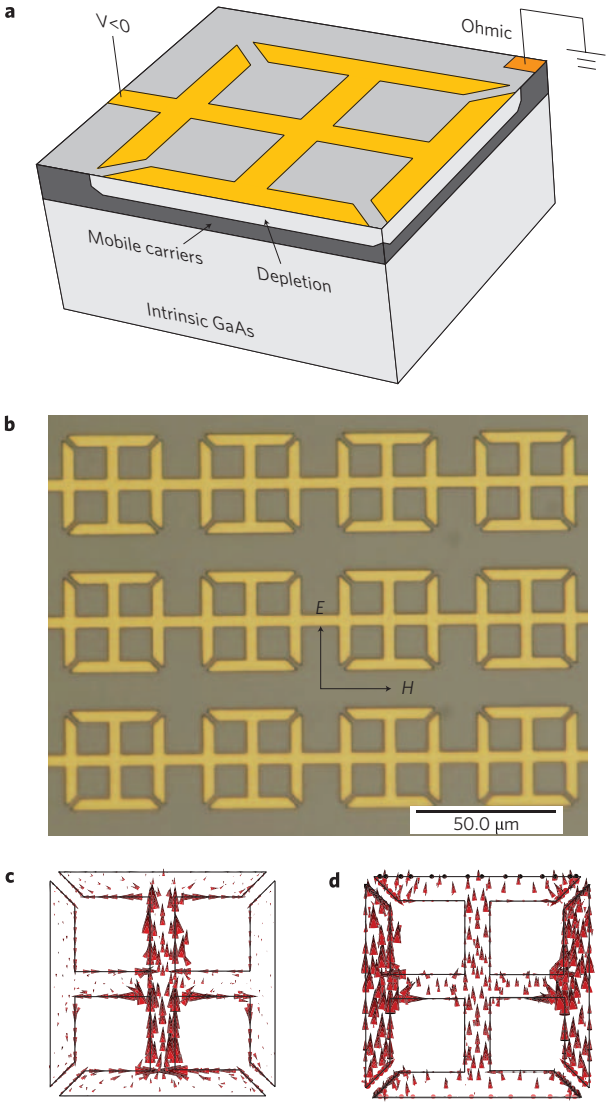

Figure 1 | Design of the electrically driven terahertz metamaterial phase shifter. a, Schematic of device unit cell and its cross-section, indicating the principle of operation. **b**, Optical microscopy image of the active area of the device with gold thickness 200 nm, linewidth 4 μm, split gap spacing 2 μm, outer dimension 36 μm, and period 50 μm. The polarization of the normally incident terahertz radiation is also indicated. **c**,**d**, Numerical simulations of surface current density excited from the inductive–capacitive (**c**) and collective dipolar (**d**) resonances at 0.81 and 1.7 THz, respectively.

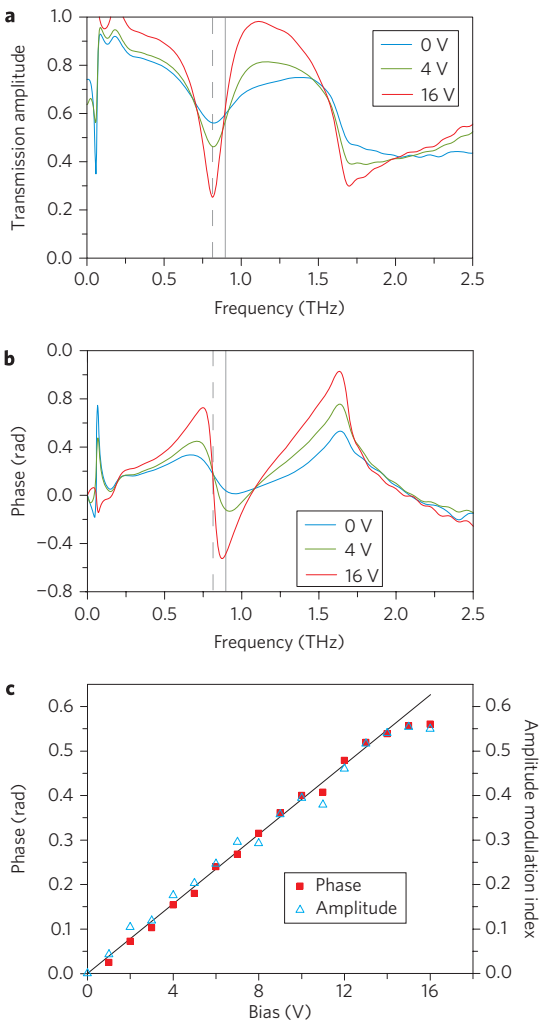

Figure 2 | Electrically controllable terahertz transmission spectra. **a**,**b**, Transmission amplitude (**a**) and phase spectra (**b**) at 0 V and reverse bias voltages of 4 and 16 V. The solid vertical line indicates the frequencies having a large phase shift and unchanged amplitude, and the dashed vertical line indicates the frequencies having maximum amplitude switching and minimum phase shifting. **c**, Voltage dependence of the phase shift at 0.89 THz and amplitude switching (modulation depth) at 0.81 THz. The straight line is to guide the eye and indicates a linear dependence.

a critical role in restoring resonances, as illustrated in Fig. 1c and d of the resonant surface current density.

In comparison to previously published results on metamaterial switches[18], this device has a higher modulation index of the transmission amplitude. At 16 V, the amplitude of the transmitted terahertz electric field at 0.81 THz, indicated by the dashed vertical line, has decreased from $t_{0V} = 0.56$ to $t_{16V} = 0.25$, a change of 55% (intensity change of 80%), as shown in Fig. 2a. This is an 83% performance improvement over the earlier demonstration. The transmission amplitude at 1.7 THz has decreased from $t_{0V} = 0.48$ to $t_{16V} = 0.30$. Between the two resonances the reverse voltage bias significantly increases the terahertz transmission amplitude. In short, the improved device performance results from more effective depletion of charge carriers in the split gaps under an external voltage bias.

Voltage switching of the metamaterial device yields another important functionality—phase shifting of the terahertz radiation. As shown in Fig. 2b, at 0.89 THz, indicated by the solid vertical line, the phase of terahertz transmission is $\phi_{16V} = -0.51$ rad under a reverse bias voltage of 16 V as compared to $\phi_{0V} = 0.05$ rad with no voltage bias, resulting in a shift of $\Delta\phi = 0.56$ rad. The phase shift occurs over a bandwidth of ~23 GHz (that is, 0.880–0.903 THz) with a change in amplitude of less than 10% over this range. This phase change occurs within a single metamaterial unit cell in the propagation direction. A multi-layer phase shifter based on our design would enable the ultimate goal of a 2π phase shifter. Additionally, at the operational frequency of the phase shifter, the terahertz transmission amplitude is near 60% without consideration of the substrate insertion loss and is almost independent of the applied voltage bias. This is advantageous because the terahertz phase shifter can operate with reasonably high and constant terahertz transmission amplitude. The substrate insertion loss could be lowered with metamaterial impedance-matched layers[26].

Various interconnect schemes would permit addressing individual SRR elements, thus permitting application of, for example, a voltage

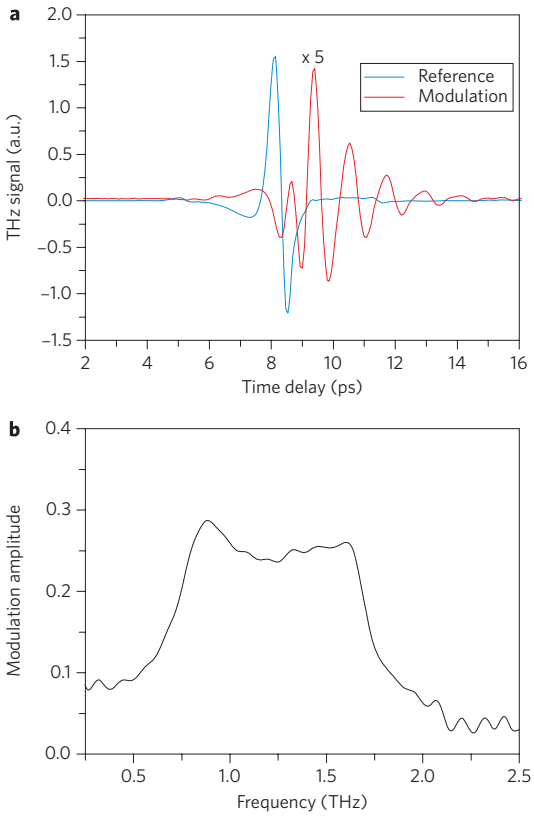

Figure 3 | Broadband modulation of terahertz radiation. a, Time-domain measurements of the terahertz modulation (differential) signal with a square-wave voltage bias alternating between 0 and 16 V. The reference terahertz signal is measured through a bare substrate using the terahertz time-domain system with a mechanical chopper. **b**, After Fourier transformation, the complex modulation in frequency domain is divided by the reference so that the modulation amplitude spectrum is obtained. In the frequency range roughly between the two resonances, the terahertz signal is most effectively modulated.

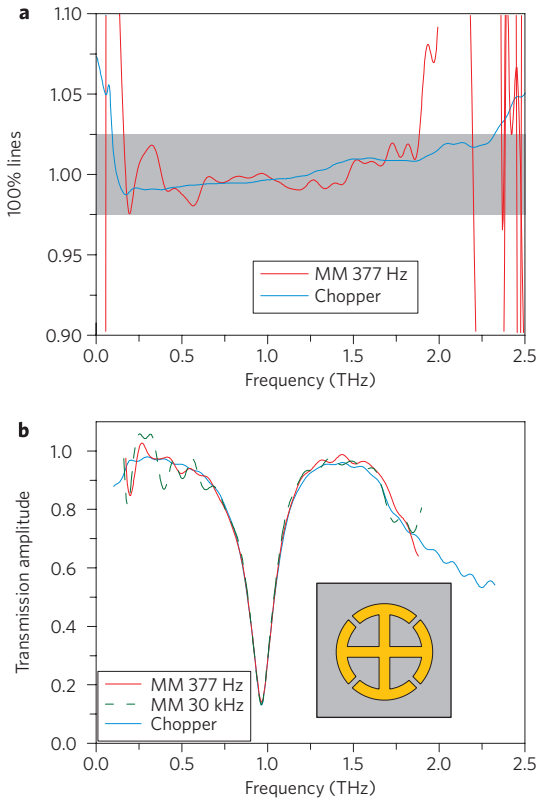

Figure 4 | Terahertz time-domain spectroscopy using the broadband metamaterial modulator. a, Amplitude spectral ratio of two subsequent measurements (100% lines) using the metamaterial device or a mechanical optical chopper as the modulator in a terahertz time-domain system, both at a modulation frequency of 377 Hz. The grey shaded area indicates the $\pm$ 2.5% noise deviation. **b**, Terahertz transmission amplitude spectra through a second metamaterial sample (unit cell shown in the inset) using the metamaterial modulator (377 Hz and 30 kHz) or a mechanical optical chopper (377 Hz).

gradient (and associated phase shift) to the array. This would allow for real-time beam steering, focusing and other manipulations of terahertz radiation for applications such as personnel screening in airports, or locking a terahertz beam from a moving satellite to a specific receiver. Therefore, it is important to characterize the phase shift, $\Delta\phi(\omega) = |\phi_V(\omega) - \phi_{0V}(\omega)|$ as a function of the applied bias voltage. Figure 2c reveals a linear phase shift as a function of the bias voltage over the range 0–16 V at 0.89 THz. Saturation sets in at higher voltage as the resonance is restored, and because of a reduction in the Schottky resistance resulting from increased leakage currents. In Fig. 2c we also plot the voltage-dependent amplitude modulation index, $M = |t_V(\omega) - t_{0V}(\omega)|/t_{0V}(\omega)$ at 0.81 THz, which reveals a similar linear dependence. We note that the metamaterial device directly manipulates terahertz waves. This is an important distinction because alternative methods yield modulation during the terahertz generation process[27,28], that is, modulated sources. Thus our metamaterial device is a true 'terahertz component', and can be combined with various terahertz sources such as backward wave oscillators or terahertz quantum-cascade lasers.

We now turn towards a demonstration of our metamaterial device as a terahertz modulator by replacing a commercial modulator (that is, a mechanical optical chopper) in a terahertz time-domain spectroscopic system. Figure 2 indicates that amplitude switching and phase shifting in our terahertz metamaterial device are inherently narrowband—a result of the resonant nature of metamaterials. However, as shown in Fig. 2a and b, the transmission amplitude and phase are not independent of each other, but are causally connected, as manifested by Kramers–Kronig (KK) relations[29]. Specifically, the phase is proportional to the derivative of the amplitude with respect to the frequency. Near frequencies where the amplitude is not strongly dependent on the applied bias voltage, but its slope is, the phase experiences a maximum shift, and vice versa. Thus, although the amplitude modulation and phase shifting response are inherently narrowband and strongly frequency dependent, the KK relations specify that the metamaterial depicted in Fig. 1a will modulate over an extended range. Thus, our device can be used as a broadband modulator.

The frequency-dependent modulation of terahertz transmission is given by

$$|\Delta\tilde{t}(\omega)| = \left| t_{V1}(\omega)e^{i\phi_{V1}(\omega)} - t_{V2}(\omega)e^{i\phi_{V2}(\omega)} \right| \qquad (1)$$

showing that the amplitude and phase contribute to the modulation. Figure 3a presents the experimental results of the metamaterial device acting as a broadband modulator. The time-domain waveform of the terahertz modulation (differential) signal is shown as the red curve for application of a square-wave voltage bias alternating between 0 and 16 V. The mechanical optical chopper has been removed from the terahertz time-domain system. As a reference, the terahertz transmission signal through a bare GaAs substrate is also measured. The modulated terahertz spectrum produced by the metamaterial device is shown in Fig. 3b and displays a broadband

and rather flat response of $\Delta t(\omega) \approx 25\%$ between 0.8 and 1.7 THz, beyond which the terahertz radiation is also modulated but with decreasing modulation depth. These frequencies correspond to the two metamaterial resonances shown in Fig. 2. By using methods to increase the frequency span between the two resonances[30], it is possible to further broaden the modulation bandwidth.

This terahertz modulator can be implemented into a terahertz time-domain spectrometer, replacing the typical mechanical optical chopper. To further evaluate the performance, in Fig. 4a we plot the division of two subsequent measurements, a so-called 100% line, at the modulation frequency of 377 Hz. This quantity represents the frequency-dependent noise of the system as deviations from 100%. We take as our evaluation point deviations of $\pm 2.5\%$, indicated by the grey area of Fig. 4a. The same procedure is also performed for a mechanical optical chopper at the same modulation frequency. The mechanical chopper yields a range from 93 GHz to 2.32 THz in this particular terahertz system, where the noise is mainly from the long-term system stability. The metamaterial modulator range is from 161 GHz to 1.88 THz. For a more restrictive criterion of $\pm 1\%$, the metamaterial device achieves a modulation range from 0.61 to 1.69 THz, roughly between the two resonance frequencies. The signal-to-noise ratio is not as good as the mechanical chopper, which achieves a 100% modulation depth with no insertion loss, and has, in principle, infinite bandwidth. We also note that operating this device as a broadband modulator requires phase-sensitive detection. However, the compact metamaterial modulator has no moving parts, is only 1 μm thick (one layer of active material), and has been demonstrated to operate up to 2 MHz (ref. 19), which can reduce the signal acquisition time. In contrast, mechanical optical choppers are bulky and are limited to kilohertz modulation rates.

As a further test, we performed terahertz transmission measurements through a second metamaterial sample (see inset to Fig. 4b) using our metamaterial device as a chopper (377 Hz). In Fig. 4b the transmitted amplitude spectra are shown, clearly identifying the metamaterial resonance near 1 THz. The results are comparable to those measured using a mechanical chopper (377 Hz). The agreement in Fig. 4 confirms the applicability of this metamaterial modulator as a functional device. Figure 4b also shows results at 30 kHz, significantly exceeding the operational frequency of mechanical choppers. Comparable performance to the results obtained at 377 Hz demonstrates the high-speed modulation capability.

In conclusion, we have demonstrated a single-layer, electrically controllable terahertz metamaterial phase shifter yielding up to $\Delta\phi = 0.56$ rad with constant insertion loss. The phase shifting, as well as the amplitude modulation index, reveal a linear dependence on the applied voltage bias. It is possible to individually address the metamaterial elements, which could be useful for future terahertz devices such as voltage-controlled arrays for active beam steering and focusing. This metamaterial device has been shown to modulate a complex transmission signal, and we have demonstrated its use as a high-speed broadband modulator in a terahertz time-domain spectrometer.

Received 24 November 2008; accepted 20 January 2009; published online 22 February 2009

References

1. Grischkowsky, D., Keiding, S., van Exter, M. & Fattinger, Ch. Far-infrared time-domain spectroscopy with terahertz beams of dielectrics and semiconductors. *J. Opt. Soc. Am. B* **7,** 2006–2015 (1990).
2. Köhler, R. *et al.* Terahertz semiconductor-heterostructure lasers. *Nature* **417,** 156–159 (2002).
3. Tonouchi, M. Cutting-edge terahertz technology. *Nature Photon.* **1,** 97–105 (2007).
4. Smith, D. R., Pendry, J. B. & Wiltshire, M. C. K. Metamaterials and negative refractive index. *Science* **305,** 788–792 (2004).
5. Veselago, V. G. The electrodynamics of substances with simultaneously negative values of ε and μ. *Sov. Phys. Usp.* **10,** 509–514 (1968).
6. Shelby, R. A., Smith, D. R. & Schultz, S. Experimental verification of a negative index of refraction. *Science* **292,** 77–79 (2001).
7. Pendry, J. B. Negative refraction makes a perfect lens. *Phys. Rev. Lett.* **85,** 3966–3969 (2000).
8. Fang, N., Lee, H., Sun, C. & Zhang, X. Sub-diffraction-limited optical imaging with a silver superlens. *Science* **308,** 534–537 (2005).
9. Schurig, D. *et al.* Metamaterial electromagnetic cloak at microwave frequencies. *Science* **314,** 977–980 (2006).
10. Yen, T. J. *et al.* Terahertz magnetic response from artificial materials. *Science* **303,** 1494–1496 (2004).
11. Azad, A. K., Dai, J. & Zhang, W. Transmission properties of terahertz pulses through subwavelength double split-ring resonators. *Opt. Lett.* **31,** 634–636 (2006).
12. Chen, H.-T. *et al.* Complementary planar terahertz metamaterials. *Opt. Express* **15,** 1084–1095 (2007).
13. Chen, H.-T. *et al.* Experimental demonstration of frequency-agile terahertz metamaterials. *Nature Photon.* **2,** 295–298 (2008).
14. Padilla, W. J., Taylor, A. J., Highstrete, C., Lee, M. & Averitt, R. D. Dynamical electric and magnetic metamaterial response at terahertz frequencies. *Phys. Rev. Lett.* **96,** 107401 (2006).
15. Chen, H.-T. *et al.* Ultrafast optical switching of terahertz metamaterials fabricated on ErAs/GaAs nanoisland superlattices. *Opt. Lett.* **32,** 1620–1622 (2007).
16. Landy, N. I., Sajuyigbe, S., Mock, J. J., Smith, D. R. & Padilla, W. J. Perfect metamaterial absorber. *Phys. Rev. Lett.* **100,** 207402 (2008).
17. Tao, H. *et al.* A metamaterial absorber for the terahertz regime: Design, fabrication and characterization. *Opt. Express* **16,** 7181–7188 (2008).
18. Chen, H.-T. *et al.* Active terahertz metamaterial devices. *Nature* **444,** 597–600 (2006).
19. Chen, H.-T. *et al.* Hybrid metamaterials enable fast electrical modulation of freely propagating terahertz waves. *Appl. Phys. Lett.* **93,** 091117 (2008).
20. Libon, I. H. *et al.* An optically controllable terahertz filter. *Appl. Phys. Lett.* **76,** 2821–2823 (2000).
21. Kersting, R., Strasser, G. & Unterrainer, K. Terahertz phase modulator. *Electron. Lett.* **36,** 1156–1158 (2000).
22. Hsieh, C.-F., Pan, R.-P., Tang, T.-T., Chen, H.-L. & Pan, C.-L. Voltage-controlled liquid-crystal terahertz phase shifter and quarter-wave plate. *Opt. Lett.* **31,** 1112–1114 (2006).
23. Padilla, W. J. *et al.* Electrically resonant terahertz metamaterials: Theoretical and experimental investigations. *Phys. Rev. B* **75,** 041102(R) (2007).
24. O'Hara, J. F., Zide, J. M. O., Gossard, A. C., Taylor, A. J. & Averitt, R. D. Enhanced terahertz detection via ErAs:GaAs nanoisland superlattices, *Appl. Phys. Lett.* **88,** 251119 (2006).
25. Acuna, G. *et al.* Surface plasmons in terahertz metamaterials. *Opt. Express* **16,** 18745–18751 (2008).
26. Lee, J. W. *et al.* Invisible plasmonic meta-materials through impedance matching to vacuum. *Opt. Express* **13,** 10681–10687 (2005).
27. Zhao, G., Schouten, R. N., van der Valk, N., Wenckebach, W. Th. & Planken, P. C. M. Design and performance of a THz emission and detection setup based on a semi-insulating GaAs emitter. *Rev. Sci. Instrum.* **73,** 1715–1719 (2002).
28. Cai, Y. *et al.* Coherent terahertz radiation detection: Direct comparison between free-space electro-optic sampling and antenna detection. *Appl. Phys. Lett.* **73,** 444–446 (1998).
29. Jackson, J. D. *Classical Electrodynamics* 3rd edn (John Wiley & Sons, 1998).
30. Azad, A. K., Taylor, A. J., Smirnova, E. & O'Hara, J. F. Characterization and analysis of terahertz metamaterials based on rectangular split-ring resonators. *Appl. Phys. Lett.* **92,** 011119 (2008).

Acknowledgements

We thank I. Brener for coordinating the sample fabrication, J.F. O'Hara for discussions and the use of the terahertz system, and D. Lippens for useful discussions. We acknowledge support from the Los Alamos National Laboratory LDRD Program. This work was performed, in part, at the Center for Integrated Nanotechnologies, a US Department of Energy, Office of Basic Energy Sciences Nanoscale Science Research Center operated jointly by Los Alamos and Sandia National Laboratories. Los Alamos National Laboratory, an affirmative action/equal opportunity employer, is operated by Los Alamos National Security, LLC, for the National Nuclear Security Administration of the US Department of Energy under contract DE-AC52-06NA25396.

Additional information

Supplementary Information accompanies this paper at www.nature.com/naturephotonics. Reprints and permission information is available online at http://npg.nature.com/reprintsandpermissions/. Correspondence and requests for materials should be addressed to H.T.C.

nature photonics

LETTERS

PUBLISHED ONLINE: 22 FEBRUARY 2009 | DOI: 10.1038/NPHOTON.2009.22

Terahertz field enhancement by a metallic nano slit operating beyond the skin-depth limit

M. A. Seo[1], H. R. Park[1], S. M. Koo[2], D. J. Park[1], J. H. Kang[3], O. K. Suwal[4], S. S. Choi[4], P. C. M. Planken[5], G. S. Park[1], N. K. Park[2], Q. H. Park[3]* and D. S. Kim[1]*

The unique optical properties of metals are at the core of many areas of research and applications, including plasmonics[1–4], metamaterials[5,6], superlensing and subdiffraction focusing[7–10], optical antennas[11–14] and surface enhanced Raman scattering[15]. One important length scale inherent in metamaterials and plasmonics research activities in the microwave[5,16], terahertz[17–19], infrared[20,21], visible[22] and ultraviolet ranges[7] is the skin depth of metal, which remains at the submicrometre level throughout the broad spectral range. One prominent question is whether terahertz electromagnetic waves can be controlled on the nanoscale to achieve new functionalities in the sub-skin-depth regime. Here, we show that a $\lambda/30{,}000$ slit on metal film acts as a nanogap-capacitor charged by light-induced currents, enhancing the electric field by orders of magnitudes.

Feature sizes of metamaterials tailored for specific electric or magnetic properties in the terahertz and microwave regions are much smaller than the wavelength, but are nonetheless much larger than the skin depth. Subwavelength metallic structures, in the form of apertures, can focus an electric field and enhance light transmission with plasmonic, half-wavelength, or Fabry–Perot resonances[1–3,18,23–28]. Resonance focusing has been previously investigated at length scales smaller than the wavelength, but far greater than the skin depth. In this regime, perfect conductor approximation has been used to describe field enhancement in one- and two-dimensional apertures[23,25–27], where it has been shown that the field enhancement keeps increasing with decreasing gap widths. The following question arises. When the width decreases to such an extent that it enters the new regime of a nanogap, with a width smaller than the skin depth, will the electric field inside the gap keep increasing?

To probe field enhancement at sub-skin-depth nanogaps, terahertz time-domain spectroscopy[29–31] was performed for a frequency range of 0.1 – 1.1 THz (wavelength of 3 – 0.27 mm). It was found that the presence of the nanogap profoundly modifies the transmittance, which now shows resonance-lacking $1/f$-type dependence, where f is frequency. The area-normalized amplitude, equivalent to the level of field enhancement[23,32,33], keeps increasing with decreasing gap width because charges concentrate near the gap, increasing the charge density and so enhancing the electric field. The enhancement reaches a maximum value of 800 at 0.1 THz for the narrowest gap width of 70 nm, smaller by a factor of three than the skin depth, which is 250 nm for gold at this frequency. The enhanced field in the nanogap fully scatters towards the far-field because no cut-off exists. With the broad $1/f$ spectral response, a maximum $|E|^2$ enhancement of 10^5, and a nonlinear $|E|^4$ enhancement of 10^{11}, this nanogap structure is an excellent launching pad for inducing terahertz nonlinearity, small terahertz signal detection in astronomy and nanoparticle detection.

When an electromagnetic wave impinges on a conducting plane at normal incidence, current is induced on the surface, which reflects light back, with no charge accumulating anywhere. When this plane is cut into two Sommerfeld half planes that are perfectly conducting, charges accumulate at the edges with a length scale of one wavelength, so that the surface charge density has the following dependence as a function of time for small values of $x \ll \lambda$:

$$\sigma(x,t) = \frac{\varepsilon_0 E_0}{\sqrt{2\pi}} \sqrt{\frac{\lambda}{x}} e^{-i\omega t} e^{-(\pi i/4)}$$

Here, ε_0 and E_0 represent the vacuum permittivity and the incident electric field, respectively, and ω and x are the angular frequency and distance from the edge, respectively[34]. The charge singularity at $x = 0$ for this half plane is not strong, for it disappears with integration.

For a case in which the two metallic half planes are brought back together so that the charges begin to feel the pull of their opposite members across the gap, it is expected that the charges will move closer towards the edge, creating a stronger electric field. As the gap continues to close towards the sub-skin depth and below, light-induced currents will keep flowing towards the gap, which induces even more concentrated charges at the edges (Fig. 1a). Although qualitative, our simple picture of an effective line-capacitor (Fig. 1a) driven by light-induced alternating currents already suggests that the field enhancement will keep increasing even when the gap size becomes smaller than the skin depth.

A nearly free-standing 60-nm-thick gold film deposited onto a 1.2-μm-thick layer of SiO_2 followed by a 0.5-μm-thick layer of SiN (Fig. 1b) was prepared. Figure 1c presents a schematic of our experiment. The sample consisted of a nanogap (width, $a = 70$ nm) fabricated using a focused ion beam (FIB) apparatus (FIB200, FEI) on the gold film. Electro-optic sampling terahertz time-domain spectroscopy was used to measure the transmitted far-field amplitude, which was connected to the enhanced near-field amplitude at the gap through vector diffraction theory. Figure 2a shows the measured electro-optic signal through the nanogap sample (top, red line), and through the unpatterned gold on the SiN/SiO_2 membrane (middle, yellow line). The reference signal through a reference aperture of 2 mm × 2 mm on the substrate only is shown as the black line. The small but non-negligible direct transmission through the unpatterned gold film reflects the fact that our film thickness is of the order of the skin depth. The contribution of this direct transmission, which is

[1]Center for Subwavelength Optics and Department of Physics and Astronomy, Seoul National University, Seoul 151-747, Korea, [2]Photonic Systems Laboratory, School of EECS, Seoul National University, Seoul 151-744, Korea, [3]Department of Physics, Korea University, Seoul 136-701, Korea, [4]Department of Physics and Advanced Materials Science, Sun Moon University, Asan 336-708, Korea, [5]Faculty of Applied Sciences, Delft University of Technology, Lorentzweg 1, 2628 CJ Delft, The Netherlands; *e-mail: dsk@phya.snu.ac.kr; qpark@korea.ac.kr

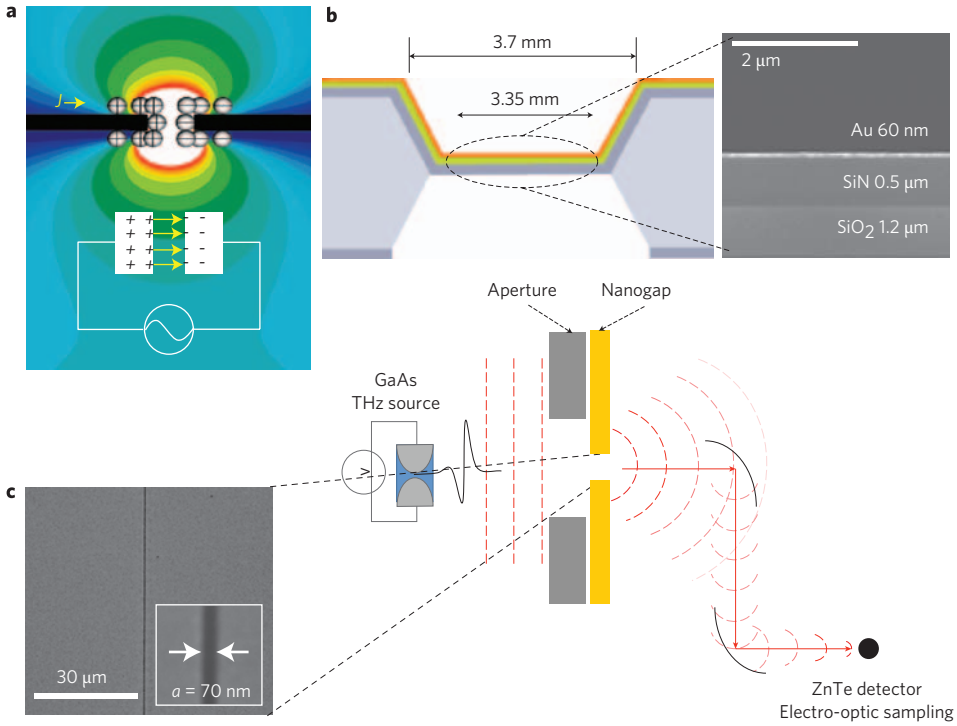

Figure 1 | Terahertz nanogap concept and time-domain spectroscopy. a, Light-induced alternating current J charges the nanogap, thereby enhancing the electric field as represented by the gradual colour contour. The white schematic below represents an equivalent circuit. **b**, A cross-section of the nearly free-standing sample structure before FIB processing of the nanogap. To the right is a scanning electron microscopy (SEM) image of the area indicated in the main panel. **c**, An SEM image shows the geometry and dimensions of the nanogap: a 70-nm-width nanogap perforated on gold film. Terahertz time-domain spectroscopy using electro-optic sampling measures far-field transmitted amplitudes at a ZnTe detector through both a normalizing aperture and the nanogap.

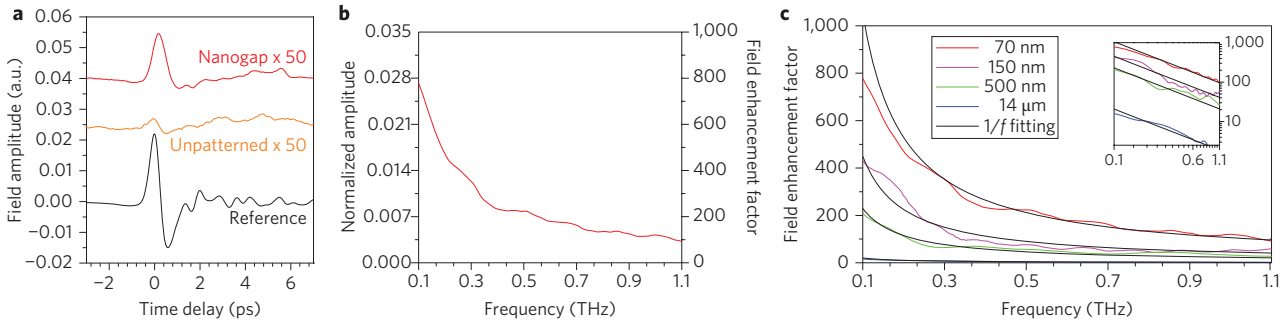

Figure 2 | Terahertz time-domain spectroscopy through nearly free-standing nanogaps. a, Electro-optic sampling signal in the time domain, through the 70-nm gap (top, red trace), the unpatterned gold (middle, yellow trace), and the 2 mm × 2 mm aperture-only reference signal (bottom, black trace). **b**, Amplitude α (ω), normalized against the aperture. The field enhancement α (ω)/β is shown on the right axis. **c**, Field enhancement through samples with various nanogap widths: $a = 70$ nm (red trace), 150 nm (pink), 500 nm (green) and 14 μm (blue), where $h = 60$ nm, 150 nm, 60 nm and 17 μm, respectively. The fits (black lines) indicate $1/f$ dependence. Inset: Log–log plot of the field enhancement.

consistent with a skin depth of ~250 nm at 0.1 THz and 80 nm at 1 THz (refs 35,36), needs to be and has been subtracted when estimating the field enhancement at the nanogap. Applying a Fourier transform of time traces and dividing them by the reference signal, we obtain the reference aperture-normalized amplitude spectrum $\alpha(\omega)$.

Figure 2b presents $\alpha(\omega)$ for the 70-nm nanogap sample, featuring a $1/f$ type frequency dependence, reaching $\alpha(\omega) = 2.7\%$ at the lowest frequency of 0.1 THz. It is important to note that α (0.1 THz) is much larger, by a factor of 800, than the nanogap-to-aperture area ratio β = width (nanogap)/width (aperture), which is only 0.0035% = 70 nm/2 mm. Noting that an unperturbed incident field amplitude at the nanogap should have resulted in a constant amplitude of $\alpha(\omega: E_{\text{inc unperturbed}}) = \beta = 0.0035\%$, it is evident that the experimentally observed $1/f$ dependence and enhanced $\alpha(\omega)$ originates from the edge charge enhanced field at the capacitor-like nanogap (see Methods for further detail).

Figure 2c shows field enhancement factors $\alpha(\omega)/\beta$, measured for three nanogaps: $a = 70$ nm ($h = 60$ nm), 150 nm ($h = 150$ nm) and 500 nm ($h = 60$ nm), where h is the film thickness. For comparison, data for an $a = 14$ μm sample with $h = 17$ μm are shown (blue). Displayed in the inset are the log–log plots of the field enhancement for the four samples. For all the samples, the field enhancement keeps increasing with decreasing frequency, describing a $1/f$-type frequency dependence denoted as black lines. This resonance-lacking $1/f$ frequency dependence of the field enhancement implies a capacitor-like charging of the nanogap by an alternating current

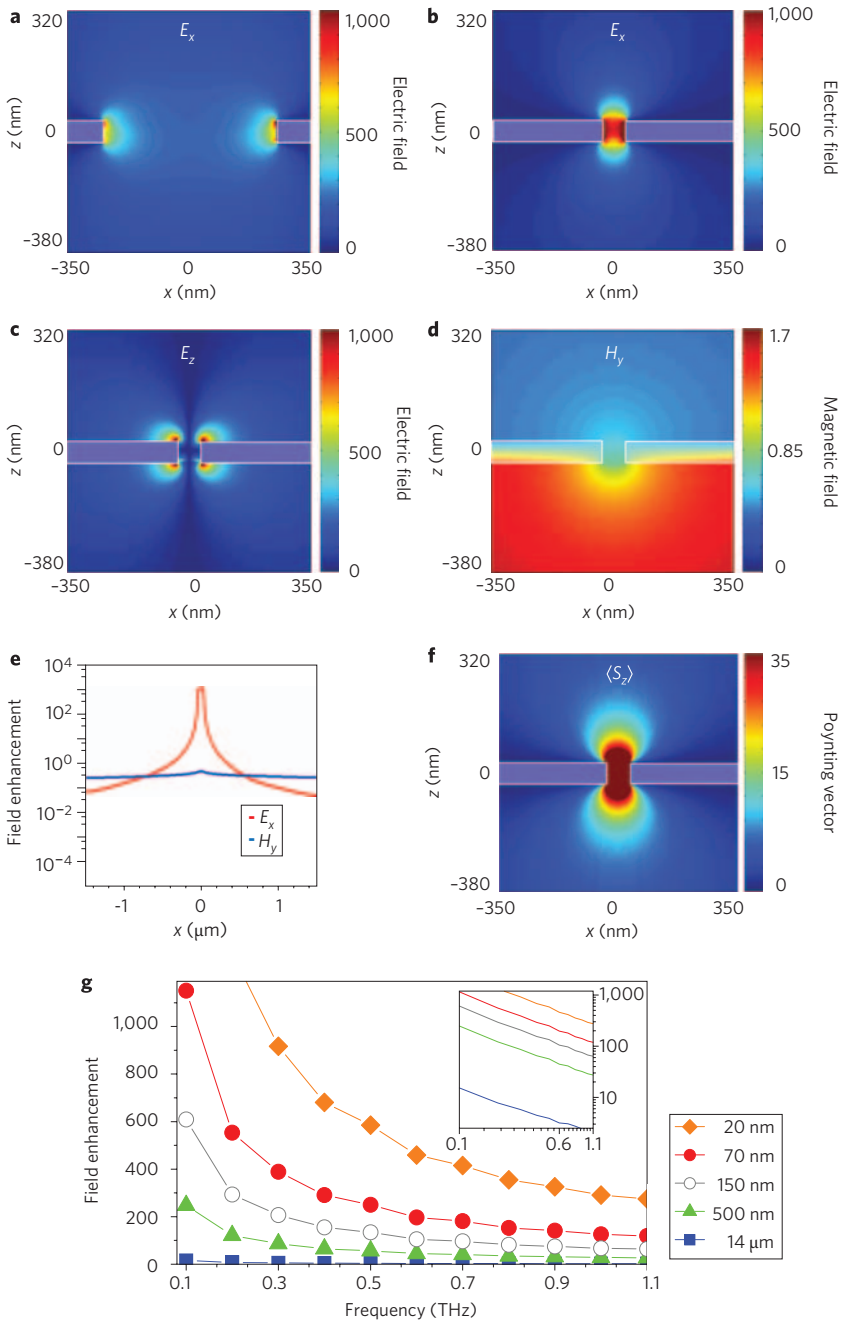

Figure 3 | The FDTD analysis of fields around nanogaps. a, Simulated horizontal electric field around a 500-nm gap with an area of 700 nm × 700 nm at 0.1 THz. **b**, Horizontal electric field around a 70-nm gap. **c**, Vertical electric field around the 70-nm gap. **d**, Simulated magnetic field around the 70-nm gap. **e**, Cross-sectional plot of the horizontal electric and magnetic fields at the exit side. **f**, Time-averaged Poynting vector component $\langle S_z \rangle$. **g**, Frequency-dependent horizontal electric field at the exit plane measured mid-gap for gap widths of 20 nm, 70 nm, 150 nm, 500 nm and 14 μm ($h = 60$ nm, 60 nm, 150 nm, 60 nm and 17 μm, respectively).

source, where the electric field is proportional to the charging time or equivalently $1/f$. We also note that the field enhancement for the 14-μm gap sample is at best 10, even at the lowest frequency where the enhancement is the largest, consistent with earlier works[23,27]. The enhancement is the largest for the smallest gap size $a = 70$ nm, reaching the value of 800 at 0.1 THz. The field enhancement implied in Fig. 2c for the nanogap is much larger than those in micrometre- and millimetre-sized gaps in terahertz and microwave ranges[16,27,32], and nanogaps in the optical range[37,38], because both the gap width and the thickness are in the $\lambda/10{,}000$ range.

The nanogap parameters—film thickness h and width a—are of the order of the skin depth or smaller, so the assumption of a perfect conductor as normally used for terahertz metamaterials may not apply. For a better understanding and optimization of our nanogap structure, two-dimensional finite-difference time-domain (FDTD) analysis was carried out. It is important to note that, regarding the problem of extending the size from the centimetre scale (sample dimension) down to nanometre (metal grid) ranges, asymptotically varying grid sizes[39] were used. For the highly varying field inside the metal and at the nanogap, a 2.5-nm grid size was used, which gradually becomes larger as the process shifts away from the metal/nanogap region, up to 25 μm for fields in air. Convergence of this asymptotic grid size control was also confirmed by testing different grid densities (in a factor of 2 for each axis) in the two-dimensional FDTD, to verify

field amplitudes converging to the solution with less than 2% of errors over the whole simulation space (10×2.5 mm^2). To implement the response of real metal in the FDTD analysis within the frequency range of interest, the Drude model was adopted for the calculation of the dielectric parameters of the metal (gold)[35]:

$$\varepsilon(\omega) = \varepsilon_\infty - \frac{\omega_p^2}{\omega(\omega + i\gamma)}$$

where $\varepsilon_\infty = 1$, plasma frequency $\omega_p = 1.37 \times 10^4$ THz and $\gamma = 40.7$ THz for gold. Notably, the skin depth at 0.1 THz is 250 nm, clearly larger than the 70-nm gap width or the 60-nm film thickness.

Figure 3a shows the horizontal electric field pattern obtained from full-scale numerical analysis at 0.1 THz (wavelength 3 mm), zoomed-in on an area of 700×700 nm^2 with a 500-nm gap sample ($h = 60$ nm). The field enhancement at the gap is ~200 relative to the unperturbed incident field. We now narrow the gap to 70 nm, as shown in Fig. 3b. The field enhancement is much stronger here than with a 500-nm gap; it is more than 1,000 at its maximum. This prediction of an increasing field enhancement with a decreasing gap beyond the skin depth regime is consistent with the simple concept here of charges concentrating towards the gap region as the gap closes. It is also in good agreement with the experimentally obtained field enhancement of 800. It is worth noting that the field is completely concentrated at the nanogap without penetrating into the metal, even with the nanogap size of 70 nm, which is much smaller than the skin depth of 250 nm. This is because the horizontal electric field at the gap is normal to the gap wall, at which point it is terminated by surface charges. The vertical electric field shown in Fig. 3c is also concentrated on the immediate vicinity of the gap and is terminated by surface charges on the metal plane. Note that the size of the surface charge spread is close to the gap width, consistent with our picture that charges move closer and closer to the edges as the gap narrows, most likely due to the attraction of opposite charges.

In stark contrast to the strong horizontal electric field that is focused on the gap region, the magnetic field H_y (Fig. 3d) is much more spread out, with essentially no enhancement. It also penetrates deeply into the metallic region, consistent with the skin depth. Figure 3e shows the E_x and H_y fields calculated at an effective distance of 2.5 nm above the exit plane (in logarithmic scale). Although the magnetic field stays mostly constant in this length scale, of order 1, the horizontal electric field at the gap is orders of magnitudes stronger than the magnetic field. Once we move away from the centre of the nanogap into the top of the metallic surface, the electric field becomes weaker than the magnetic field. To demonstrate the energy flow through the nanogap, Fig. 3f shows a plot of the time-averaged Poynting vector $\langle S_z \rangle$, where concentration of light energy at the sub-skin-depth gap is apparent. What is striking is that the Poynting vector enhancement is much smaller than what simple multiplication of electric and magnetic fields suggests, indicating that the phase difference between the enhanced (charge-induced) electric field and impinging magnetic fields is close to 90° in this quasi-static regime.

Finally, the frequency and width dependence of the average electric field enhancement at the gap $\langle E_{near} \rangle / E_{inc}$, shown in Fig. 3g, reproduce the experimentally observed field enhancement well, quantitatively as well as qualitatively, including the $1/f$-type dependence and the increasing enhancement with decreasing a. The film thickness was 60 nm for $a = 70$ nm and $a = 500$ nm, 150 nm for $a = 150$ nm, and 17 μm for $a = 14$ μm. In simulation, a nanogap of size 20 nm was also considered to probe the possibility of enhancing the nanogap performance with smaller gap width. Indeed, larger enhancement is seen with the 20-nm gap ($h = 60$ nm), still maintaining the $1/f$ dependence, indicating that our scheme would work for even smaller gap sizes. Analysing the current distribution inside the conductor and the surface charge distribution near the nanogap shows that while the current distribution is nearly frequency-independent apart from the trivial $e^{-i\omega t}$ dependence, the surface charges at the nanogap contain the necessary $1/f$ term. This dependence, which is universal in any capacitor problem with an alternating current source, is therefore consistent with the terahertz light field-induced, harmonically oscillating currents charging the nanogap, with the charging time inversely proportional to the driving frequency.

As made evident by these findings, because millimetre waves can concentrate onto a nanogap smaller than the skin depth, it should be possible to enhance the electric field further by closing the gap some more. The ultimate gap size may be determined at the charge-screening length scale of metal, which is the Thomas–Fermi screening length, typically below 1 nm. Focusing of terahertz electromagnetic waves at the nanometre scale and below could result in a field enhancement of ~10,000, which would find applications in, for instance, terahertz nonlinearity. Even with the present gap size, which enables field enhancement of 1,000, it should be possible to reach the field amplitude of ~1–10 kV cm^{-1} necessary to induce nonlinearity at semiconductor nanostructures[40] without using amplification stages or using only continuous-wave sources such as Gunn diodes. It should also be possible, because we can obtain a field enhancement of nearly three orders of magnitudes without resonance, to increase it even further with resonance such as found in half-wavelength antenna. With such a design, the use of terahertz radiation to detect nanoparticles inside nanogaps or to detect the existence of a bridge become feasible.

In conclusion, we have shown that a $\lambda/30{,}000$ nanogap focuses terahertz electromagnetic waves with wavelengths in the range of millimetres, resulting in enormous field enhancement. Metallic nanostructures tailored for terahertz operations would find wide-ranging applications as sub-skin-depth field-enhancing and focusing devices and as an enabling structure for subnanometre optics in the Thomas–Fermi length scale.

Methods

Sample fabrication. A 60-nm-thick, nearly free-standing, gold film was fabricated using photolithography (Fig. 1b). The silicon substrate was first coated with two photoresist strips and the facet of this pattern was processed using chemical etching. Following thermal wet oxidation and back-side etching, leaving 50 μm silicon, the substrate was nitride deposited. One more back-side etching step was performed to reduce the total film thickness to 1.7 μm. Gold film was deposited, after which FIB milling was used to define the nanogap structure.

Terahertz time-domain measurement and field-enhancement estimate. We used a single-cycle terahertz source generated from a 2 kV cm^{-1} biased semi-insulating GaAs emitter illuminated by a femtosecond Ti:sapphire laser pulse train of wavelength 780 nm, 76 MHz repetition rate and 150-fs pulse width. An electro-optic sampling method was used to detect the transmitted terahertz waves in the time domain, in which an optical probe pulse undergoes a slight polarization rotation by the synchronized terahertz beam in a (110) oriented ZnTe crystal, detecting the horizontal electric field.

We first measured the transmitted electric field $E_{far}^{aperture}(\omega)$ at the detector through the substrate only with a 2 mm × 2 mm reference aperture. The measured electric field for the nanogap sample after subtracting the direct transmission is denoted $E_{far}^{gap}(\omega)$. We define the amplitude $\alpha(\omega)$ normalized against the aperture field as the ratio between the two measured amplitudes:

$$\alpha(\omega) = |E_{far}^{gap}(\omega)/E_{far}^{aperture}(\omega)|$$

In what follows, we show that the near-field enhancement corresponds to $\alpha(\omega)/\beta$, where β is the nanogap-to-aperture width ratio. We assumed that the 2-mm aperture is macroscopic enough to have essentially the same electric field as the incident one, E_{inc}, as confirmed by the FDTD simulation. To relate the far-field amplitude E_{far} at the detector with the near-field amplitude E_{near} for the aperture (or nanogap), we used the vector diffraction theory for normal incidence and forward detection[41]. We arrived at $E_{far}^{aperture} = (e^{ikR}/i\lambda R)\int_0^b\int_0^b E_{inc}\,dx\,dy = (e^{ikR}/i\lambda R)E_{inc}b^2$, where b is the aperture width (2 mm) and R is the distance from the aperture to the detector. Likewise, $E_{far}^{gap} = (e^{ikR}/i\lambda R)\int_0^b\int_0^a E_{near}\,dx\,dy = (e^{ikR}/i\lambda R)\langle E_{near}\rangle ab$ where a is the gap width and $\langle E_{near}\rangle$ is the average gap field $a^{-1}\int_0^a E_{near}(x)dx$. Dividing the two relations, and with $\beta = a/b$, we obtain the desired near-field enhancement factor $\langle E_{near}\rangle/E_{inc} = \alpha/\beta$. One assumption here is that the horizontal field concentrates

almost entirely at the gap, again verified by the FDTD simulation (Fig. 3b). We also considered the effect of collection optics with finite numerical aperture, which was found negligibly small in our frequency range.

Received 22 September 2008; accepted 4 February 2009; published online 22 February 2009

References

1. Ebbesen, T. W., Lezec, H. J., Chaemi, H. F., Thio, T. & Wolff, P. A. Extraordinary optical transmission through sub-wavelength hole arrays. *Nature* **391,** 667–669 (1998).
2. Pendry, J. B., Martin-Moreno, L. & Garcia-Vidal, F. J. Mimicking surface plasmons with structured surfaces. *Science* **305,** 847–848 (2004).
3. Barnes, W. L., Dereux, A. & Ebbesen, T. W. Surface plasmon subwavelength optics. *Nature* **424,** 824–830 (2003).
4. Ozbay, E. Plasmonics: Merging photonics and electronics at nanoscale dimensions. *Science* **13,** 189–193 (2006).
5. Smith, D. R., Pendry, J. B. & Wiltshire, M. C. K. Metamaterials and negative refractive index. *Science* **305,** 788–792 (2004).
6. Lezec, H. J., Dionne, J. A. & Atwater, H. A. Negative refraction at visible frequencies. *Science* **316,** 430–432 (2007).
7. Fang, N., Lee, H., Sun, C. & Zhang, X. Sub-diffraction-limited optical imaging with a silver superlens. *Science* **308,** 534–537 (2005).
8. Melville, D. O. S. & Blaikie, R. J. Super-resolution imaging through a planar silver layer. *Opt. Express* **13,** 2127–2134 (2005).
9. Grbic, A., Jiang, L. & Merlin, R. Near-field plates: subdiffraction focusing with patterned surfaces. *Science* **320,** 511–513 (2008).
10. Maier, S. A., Andrews, S. R., Martín-Moreno, L. & García-Vidal, F. J. Terahertz surface plasmon–polariton propagation and focusing on periodically corrugated metal wires. *Phys. Rev. Lett.* **97,** 176805 (2006).
11. Mühlschlegel, P., Eisler, H.-J., Martin, O. J. F., Hecht, B. & Pohl, D. W. Resonant optical antenna. *Science* **308,** 1607–1609 (2005).
12. Kim, S. *et al.* High-harmonic generation by resonant plasmon field enhancement. *Nature* **453,** 757–760 (2008).
13. Alu, A. & Engheta, N. Tuning the scattering response of optical nanoantennas with nanocircuit loads. *Nature Photon.* **2,** 307–310 (2008).
14. Hill, M. T. *et al.* Lasing in metallic-coated nanocavities. *Nature Photon.* **1,** 589–594 (2007).
15. Nie, S. & Emory, S. R. Probing single molecules and single nanoparticles by surface-enhanced Raman scattering. *Science* **275,** 1102–1106 (1997).
16. Hibbins, A. P., Evans, B. R. & Sambles, J. R. Experimental verification of designer surface plasmons. *Science* **308,** 670–672 (2005).
17. Chen, H.-T. *et al.* Active terahertz metamaterials devices. *Nature* **444,** 597–600 (2006).
18. Matsui, T., Agrawal, A., Nahata, A. & Vardeny, Z. V. Transmission resonances through aperiodic arrays of subwavelength apertures. *Nature* **446,** 517–521 (2007).
19. Kawano, Y. & Ishibashi, K. An on-chip near-field terahertz probe and detector. *Nature Photon.* **2,** 618–621 (2008).
20. Dolling, G., Enkrich, C., Wegener, M., Soukoulis, C. M. & Linden, S. Simultaneous negative phase and group velocity of light in a metamaterial. *Science* **312,** 892–894 (2006).
21. Hillenbrand, R., Taubner, T. & Keilmann, F. Phonon-enhanced light–matter interaction at the nanometre scale. *Nature* **418,** 159–162 (2002).
22. Shalaev, V. M. Optical negative-index metamaterials. *Nature Photon.* **1,** 41–48 (2006).
23. Lee, J. W. *et al.* Terahertz electromagnetic wave transmission through random arrays of single rectangular holes and slits in thin metallic sheets. *Phys. Rev. Lett.* **99,** 137401 (2007).
24. García de Abajo, F. J., Gómez-Medina, R. & Sáenz, J. J. Full transmission through perfect-conductor subwavelength hole arrays. *Phys. Rev. E* **72,** 016608 (2005).
25. Garcia-Vidal, F. J., Moreno, E., Porto, J. A. & Martin-Moreno, L. Transmission of light through a single rectangular hole. *Phys. Rev. Lett.* **95,** 103901 (2005).
26. Takakura, Y. Optical resonance in a narrow slit in a thick metallic screen. *Phys. Rev. Lett.* **86,** 5601–5603 (2001).
27. Yang, F. & Sambles, J. R. Resonant transmission of microwaves through a narrow metallic slit. *Phys. Rev. Lett.* **89,** 063901 (2002).
28. Liu, H. & Lalanne, P. Microscopic theory of the extraordinary optical transmission. *Nature* **452,** 728–731 (2008).
29. Van Exter, M., Fattinger, C. & Grischkowsky, D. Terahertz time-domain spectroscopy of water vapor. *Opt. Lett.* **14,** 1128–1130 (1989).
30. Wu, Q., Litz, M. & Zhang, X.-C. Broadband detection capability of ZnTe electro-optic field detectors. *Appl. Phys. Lett.* **68,** 2924–2926 (1996).
31. Lee, J. W. *et al.* Shape resonance omni-directional terahertz filters with near-unity transmittance. *Opt. Express* **14,** 1253–1259 (2006).
32. Lee, J. W. *et al.* Terahertz transparency at Fabry–Perot resonances of periodic slit arrays in a metal plate: experiment and theory. *Opt. Express* **14,** 12637–12643 (2006).
33. Lee, J. W. *et al.* Invisible plasmonic meta-materials through impedance matching to vacuum. *Opt. Express* **13,** 10681–10687 (2005).
34. Born, M. & Wolf, E. *Principles of Optics: Electromagnetic Theory of Propagation, Interference and Diffraction of Light*, 7th edn, ch. 11 (Cambridge Univ. Press, 1999).
35. Ordal, M. A. Optical properties of the metals Al, Co, Cu, Au, Fe, Pb, Ni, Pd, Pt, Ag, Ti and W in the infrared and far infrared. *Appl. Opt.* **22,** 1099–1119 (1983).
36. Azad, A. K. & Zhang, W. Resonant terahertz transmission in subwavelength metallic hole arrays of sub-skin-depth thickness. *Opt. Lett.* **30,** 2945–2947 (2005).
37. Miyazaki, H. T. & Kurokawa, Y. Squeezing visible light waves into a 3-nm-thick and 55-nm-long plasmon cavity. *Phys. Rev. Lett.* **96,** 097401 (2006).
38. Miyazaki, H. T. & Kurokawa, Y. Metal–insulator–metal plasmon nanocavities: analysis of optical properties. *Phys. Rev. B* **75,** 035411 (2007).
39. Taflove, A. & Hagness, S. C. *Computational Electromagnetics: The Finite-Difference Time-Domain Method* 852 (Artech House, 2000).
40. Danielson, J. R. *et al.* Interaction of strong single-cycle terahertz pulses with semiconductor quantum wells. *Phys. Rev. Lett.* **99,** 237401 (2007).
41. Jackson, J. D. *Classical Electrodynamics*, 3rd edn, ch. 10 (John Wiley & Sons, 2001).

Acknowledgements

We acknowledge helpful discussions with J. B. Pendry, D. Grischkowsky and K. J. Ahn. H. Kim is also thanked for discussions concerning diffractive optics correction used in data analysis and for Kirchhoff formalism. This work was supported by the Korea Science and Engineering Foundation (KOSEF) grant funded by the Korea government (MEST), the Korea Research Foundation (KRF), KICOS (GRL, K20815000003) and the Seoul R&BD Program.

Additional information

Reprints and permission information is available online at http://npg.nature.com/reprintsandpermissions/. Correspondence and requests for materials should be addressed to D.S.K.

nature photonics

ARTICLES

PUBLISHED ONLINE: 22 FEBRUARY 2009 | DOI: 10.1038/NPHOTON.2009.4

Stereometamaterials

Na Liu[1], Hui Liu[2], Shining Zhu[2] and Harald Giessen[1]*

The subdiscipline of chemistry that studies molecular structures in three dimensions is called stereochemistry. One important aspect of stereochemistry is stereoisomers: materials with the same chemical formula but different spatial arrangements of atoms within molecules. The relative positions of atoms have great influence on the properties of chemical substances. Here, in analogy to stereoisomers in chemistry, we propose a new concept in nanophotonics, namely stereometamaterials, which refer to metamaterials with the same constituents but different spatial arrangements. As a model system of stereometamaterials, we theoretically and experimentally study meta-dimers, which consist of a stack of two identical split-ring resonators in each unit cell with various twist angles. The interplay of electric and magnetic interactions plays a crucial role for the optical properties. Specifically, the influence of higher-order electric multipoles becomes clearly evident. The twisting of stereometamaterials offers a way to engineer complex plasmonic nanostructures with a tailored electromagnetic response.

The word 'stereo' in Greek means 'relating to space' or 'three-dimensional'. In stereochemistry, the characteristics of organic compounds depend not only on the nature of the atoms comprising the molecules (constitution) but also on the three-dimensional arrangement of these atoms in space (configuration)[1]. For example, the spatial structure of a protein molecule determines its biological activities. In photonics, metamaterials are structured media, consisting of artificial 'atoms' with unit cells much smaller than the wavelength of light[2–4]. Such metamaterial atoms can be designed to yield electric as well as magnetic dipole moments, leading to effective negative permittivity and negative permeability. A medium with simultaneous negative permittivity and negative permeability can exhibit negative refraction and unique reversed electromagnetic properties[5,6]. As well as their applicability in constructing effective media, metamaterials have also been used as prototypes for studying coupling effects between artificial atoms in three-dimensional structures[7–9]. However, the mechanism of interactions arising from different spatial arrangements of such atoms has thus far not been examined. Inspired by the concept of stereochemistry, we now investigate the coupling effects of artificial atoms in three-dimensional metamaterials from a novel perspective. We study a set of stereometamaterials, each having unit cells consisting of two stacked split-ring resonators (SRRs) with identical geometry (same constitution); however, the two SRR atoms are arranged in space using different twist angles to achieve various structures (different configurations). We term these structures stereo-SRR dimers. We theoretically and experimentally demonstrate that the optical properties of these stereo-SRR dimers can be substantially modified by altering the twist angles between the two SRR atoms, arising from the variation of electric and magnetic interactions between them. Specifically, we investigate how the electric and magnetic interactions depend on the spatial arrangement of these SRR constituents. The nontrivial magnetic interaction makes metamaterials more versatile in nanophotonics than stereoisomers in chemistry, where generally only electric interactions are taken into account. Furthermore, we show that the inclusion of the higher-order electric multipolar interactions is essential to understanding the physical implications of the twisting dispersion. A theoretical model based on a Langrangian formalism is used to interpret the evolution of the coupling effects as a function of twist angle.

Stereometamaterial design

Figure 1a illustrates the geometry of the stereo-SRR dimer metamaterials together with their design parameters. Each unit cell consists of two spatially separated SRRs, which are twisted at an angle φ with respect to one another. The SRRs are embedded in a homogeneous dielectric with $\varepsilon = 1$ (that is, air). For excitation of these SRR dimer metamaterials, we use normally incident light with its polarization along the x-direction as shown in Fig. 1a. In order to gain insight into the resonant behaviour as well as coupling mechanisms for various stereo-SRR dimer metamaterials, we first study three specific dimer systems with twist angles $\varphi = 0$, 90 and 180°. The insets of Fig. 1b–d present the schematics of the three structures, in which the vertical distance between two SRRs is set at $s = 100$ nm. Numerical simulations were performed based on a commercial finite-integration time-domain algorithm, and the simulated transmittance spectra are shown in Fig. 1b–d. For each system there are apparently two observable resonances (ω^- and ω^+). To understand these spectral characteristics, current and magnetic field distributions at the relevant resonances are calculated. For the 0° twisted SRR dimer metamaterial, the electric component of the incident light can excite circulating currents along the two SRRs, giving rise to induced magnetic dipole moments in the individual SRRs. As shown in Fig. 2a, the electric dipoles excited in the two SRRs oscillate anti-phase and in-phase at resonances ω_0^- and ω_0^+, respectively. The resulting magnetic dipoles are aligned antiparallel at resonance ω_0^-, whereas they are parallel at resonances ω_0^+. The above phenomenon can be interpreted as the plasmon hybridization[10–12] between the two SRRs due to their close proximity. In the hybridization scheme, each SRR can be regarded as an artificial atom. The two SRR atoms are bonded into an SRR dimer or SRR 'molecule' due to the strong interaction between them. Such interaction leads to the formation of new plasmonic modes, arising from the hybridization of the original state of an individual SRR. For the configuration of the 0° twisted SRR dimer system, the two excited electric dipoles are transversely coupled, while the two magnetic dipoles are longitudinally coupled. In the case of a transverse dipole–dipole interaction, the antisymmetric and symmetric modes are at the lower and higher resonance frequencies, respectively. In contrast, in the

[1]4. Physikalisches Institut, Universität Stuttgart, D-70569 Stuttgart, Germany, [2]Department of Physics, Nanjing University, Nanjing 210093, People's Republic of China; *e-mail: Giessen@physik.uni-stuttgart.de

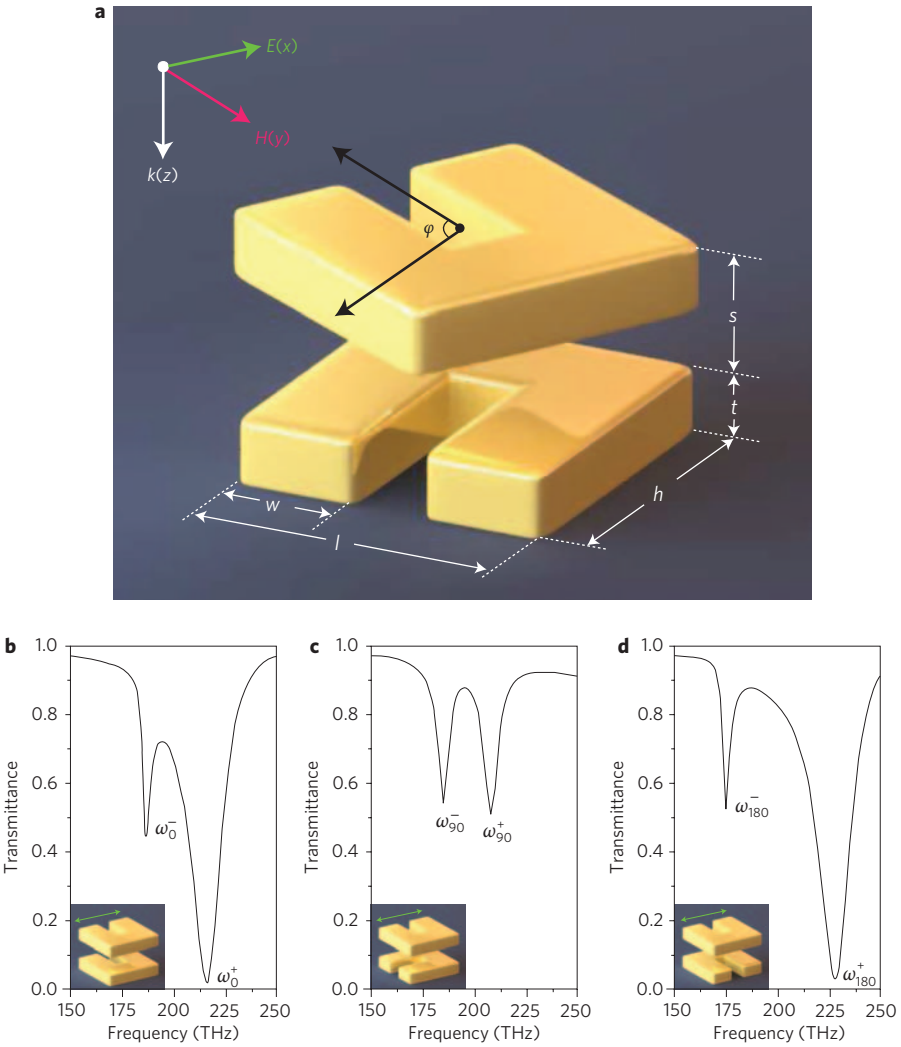

Figure 1 | Structural geometry and numerical simulation. a, Schematic of the stereo-SRR dimer metamaterials with definitions of the geometrical parameters: $l = 230$ nm, $h = 230$ nm, $w = 90$ nm, $t = 50$ nm, and $s = 100$ nm. The periods in both x and y directions are 700 nm. **b**–**d**, Simulated transmittance spectra for the 0° (**b**), 90° (**c**) and 180° (**d**) twisted SRR dimer metamaterials. All the structures are embedded in air.

case of longitudinal dipole–dipole interaction, the two magnetic dipoles should align parallel at the lower resonance frequency and antiparallel at the higher resonance frequency[12]. It is evident that for the 0° twisted SRR dimer system (see Fig. 2a), the resonance levels are determined according to the picture of transverse electric dipole–dipole interaction, with the antisymmetric (symmetric) mode having the lower (higher) resonance frequency. In essence, the two coupling mechanisms, that is, the electric and magnetic dipolar interactions, counteract one another and the electric interaction dominates in this system.

For the 90° twisted SRR dimer metamaterial, circular currents in the underlying SRR cannot be directly excited by the incident light due to its orientation with respect to the external electric field. In a sense, the underlying SRR can be regarded as a 'dark atom' at the resonant frequency of the ring[13]. Nevertheless, for the coupled dimer system, on resonance, excitation from the upper SRR can be transferred to the underlying one by the interaction between the two SRRs, which can also lead to the formation of new plasmonic modes (ω_{90}^- and ω_{90}^+). Interestingly, because the electric fields in the slit gaps of the two SRRs are perpendicular to one another, the electric dipole–dipole interaction equals zero. In addition, as the higher-order multipolar interaction is negligible in a first approximation, the electric coupling in the 90° twisted SRR dimer system can thus be ignored. As a consequence, the resonance levels are determined in line with the picture of longitudinal magnetic dipole–dipole coupling. As shown in Fig. 2b, at resonances ω_{90}^- and ω_{90}^+, the resulting magnetic dipoles in the two SRRs are aligned parallel and antiparallel, respectively.

For the 180° twisted SRR dimer metamaterial, the interaction between the two SRRs results in new plasmonic modes, ω_{180}^- and ω_{180}^+. Notably, from the current and magnetic field distributions as shown in Fig. 2c, resonances ω_{180}^- and ω_{180}^+ are associated with the excitation of the electric dipoles in the two SRRs oscillating anti-phase and in-phase, respectively. The two resulting magnetic dipoles are aligned parallel and antiparallel, accordingly. In essence, the transverse electric and longitudinal magnetic interactions contribute positively in the 180° twisted SRR dimer system. This leads to the largest spectral splitting, which is a direct indication of the coupling strength. Based on the above discussions, we infer that the optical properties of stereometamaterials depend dramatically on the spatial arrangement of metamaterial constituents. Specifically, the possibility of tuning the resonant behaviour by simply varying the relative twist angles makes stereometamaterials particularly interesting as model systems for exploring and comprehending different coupling mechanisms in complex three-dimensional plasmonic structures.

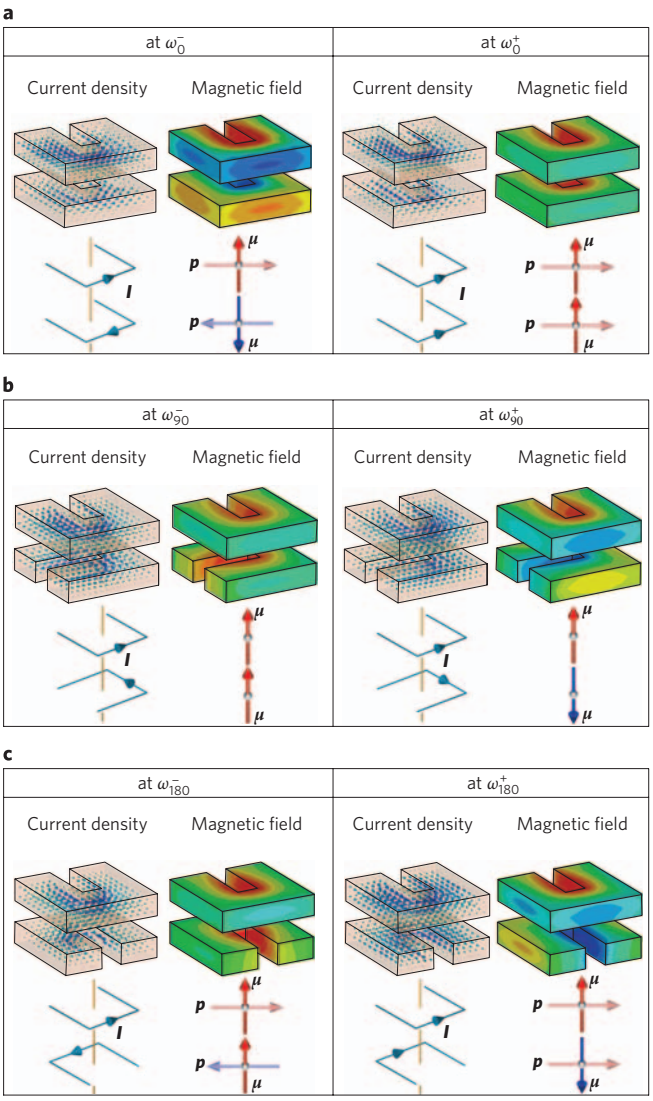

Figure 2 | Numerical current and magnetic field distributions. a–c, Current and magnetic field distributions at respective resonances for the 0° (**a**), 90° (**b**) and 180° (**c**) twisted SRR dimer metamaterials. Lower left: schematics of currents (***I***) in two SRRs. Lower right: schematics of the alignments of the magnetic (μ) and electric ($\boldsymbol{p}$) dipoles. At 0°, transverse electric and longitudinal magnetic interactions work against one another, whereas at 180° they add together. At 90°, only longitudinal magnetic interaction is present.

Twist angle

To provide deeper insight, the dependence of the optical properties of the stereo-SRR dimer metamaterials on twist angle is investigated. Figure 3 presents the simulated twisting dispersion curves (black squares) of these stereometamaterials, in which the resonance positions are extracted from the transmittance spectra of different structures. It is apparent that by increasing the twist angle φ, the two resonance branches first tend to converge, with the ω^+ branch shifting to lower frequencies, while the ω^- branch shifts to higher frequencies. An avoided crossing is observed at φ_t, which is around 60°. Subsequently, the two branches shift away from one another. In order to clarify the underlying physics of the twisting dispersion curves, we introduce a Lagrangian formalism[14]. We start from the analysis of a single SRR and then expand it to coupled stereo-SRR dimer systems. One SRR can be modelled by an equivalent *LC* circuit with a resonance frequency $\omega_f = 1/(LC)^{1/2}$. It consists of a magnetic coil (the metal ring)

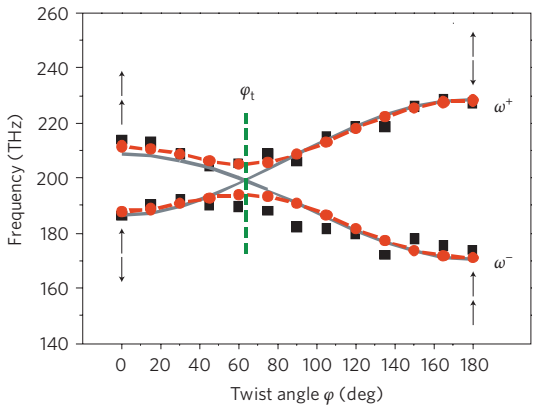

Figure 3 | Twisting dispersion of the stereo-SRR dimer metamaterials. Black squares represent the numerical data. Red lines represent the fitting curves calculated from the Lagrangian model, in which the avoided crossing is clearly visible at φ_t. The black arrows represent the alignment of the magnetic dipoles at lower and higher resonance frequencies at twist angles $\varphi = 0°$ and 180°. The grey lines represent the fitting curves calculated from the Lagrangian model without considering the higher-order electric multipolar interactions. No avoided crossing is observable in this case.

with inductance L and a capacitor (the slit of the ring) of capacitance C. If we define the total charge Q accumulated in the slit as a generalized coordinate, the Lagrangian of an SRR can be written as $\Gamma = (L\dot{Q}^2/2) - (Q^2/2C)$. Here, $L\dot{Q}/2$ refers to the kinetic energy of the oscillations, and $Q^2/2C$ is the electrostatic energy stored in the slit. Consequently, the Lagrangian of the coupled SRR dimer systems is a combination of two individual SRRs with the additional electric and magnetic interaction terms

$$\Gamma = \frac{L}{2}\left(\dot{Q}_1^2 - \omega_f^2 Q_1^2\right) + \frac{L}{2}\left(\dot{Q}_2^2 - \omega_f^2 Q_2^2\right) + M_H \dot{Q}_1 \dot{Q}_2 - M_E \omega_f^2 Q_1 Q_2 \cdot \left(\cos\varphi - \alpha \cdot (\cos\varphi)^2 + \beta \cdot (\cos\varphi)^3\right) \quad (1)$$

Here, Q_1 and Q_2 are oscillating charges in the respective SRRs, and M_H and M_E are the mutual inductances for the magnetic and electric interactions, respectively. Apart from the electric dipole–dipole interaction, the contributions from the higher-order electric multipolar[15] interactions are also included. α and β are the coefficients of the quadrupolar and octupolar plasmon interactions[16], respectively. They serve as correction terms to the electric dipolar interaction. It is straightforward to derive from equation (1) that the major interaction items for 0° and 180° cases are $M_H\dot{Q}_1\dot{Q}_2 - M_E\omega_f^2 Q_1 Q_2$ and $M_H\dot{Q}_1\dot{Q}_2 + M_E\omega_f^2 Q_1 Q_2$, respectively. It is in accord with the above simulation results that the magnetic and electric interactions contribute oppositely and positively for 0° and 180° twisted SRR dimer metamaterials, respectively. For the 90° twisted SRR dimer metamaterial, only the magnetic interaction plays a key role, as represented by the interaction term $M_H\dot{Q}_1\dot{Q}_2$. Subsequently, by solving the Euler–Lagrange equations

$$\frac{d}{dt}\left(\frac{\partial\Gamma}{\partial\dot{Q}_i}\right) - \frac{\partial\Gamma}{\partial Q_i} = 0, \quad i = 1, 2 \quad (2)$$

the eigenfrequencies of these stereo-SRR dimer systems can be obtained as

$$\omega_\pm = \omega_0 \cdot \sqrt{\frac{1 \mp \kappa_E \cdot \left(\cos\varphi - \alpha \cdot (\cos\varphi)^2 + \beta \cdot (\cos\varphi)^3\right)}{1 \mp \kappa_H}} \quad (3)$$

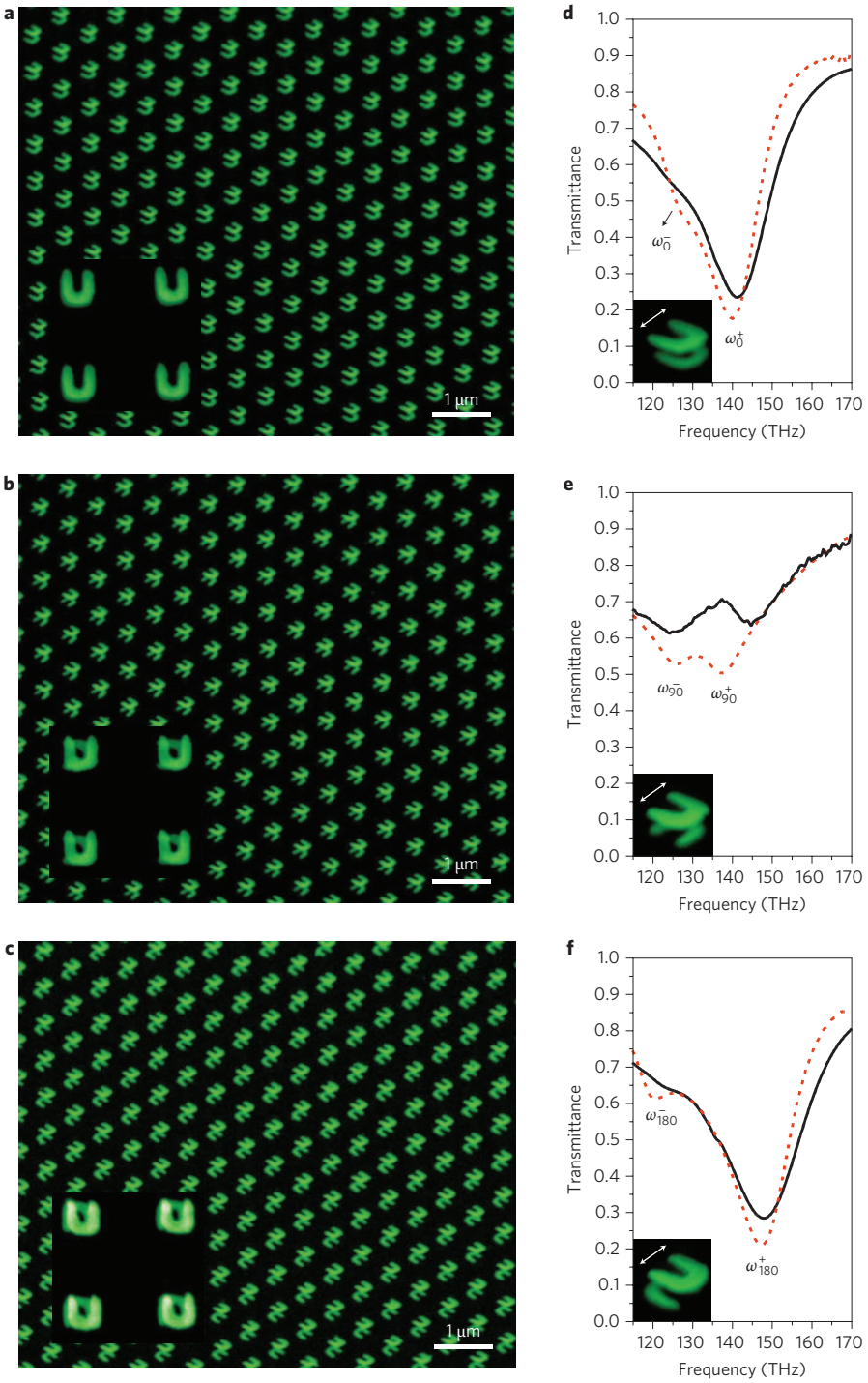

Figure 4 | Field-emission electron microscopy images and experimental measurement. a–c, Oblique views of the 0° (**a**), 90° (**b**) and 180° (**c**) twisted gold SRR dimer metamaterials. Insets: normal views. The structures were fabricated on a glass substrate. The SRRs were embedded in a photopolymer (PC403), which served as the dielectric spacer. **d–f**, Experimental transmittance spectra for the 0° (**d**), 90° (**e**), and 180° (**f**) twisted SRR dimer metamaterials. The black and red curves represent the experimental and simulated results, respectively. For the 90° twisted SRR dimer structure, an analyser is applied behind the sample, which is rotated by 75° with respect to the polarization of the incident light.

where $\kappa_E = M_E/L$ and $\kappa_H = M_H/L$ are the coefficients of the overall electric and magnetic interactions, respectively. By fitting the twisting dispersion curves, the corresponding coefficients are estimated to be $\kappa_E = 0.14$, $\kappa_H = 0.09$, $\alpha = 0.8$ and $\beta = -0.4$. Notably from Fig. 3, the fitting curves (in red lines) reproduce the numerical data quite well and the avoided crossing is clearly observable around 60°. This shows that the Lagrangian model can quantitatively corroborate the results from the numerical simulations. It is of crucial importance that the higher-order electric multipolar interactions account for the existence of the avoided crossing. Owing to the finite length of the SRR ring, discrete electric plasmon modes characterized by different spatial symmetries can be excited by the incident light. The surface charges in the SRR ring are a superposition of such fundamental plasmon modes of the ring[16].

To reveal the significant role of the higher-order electric multipolar interactions, the grey lines in Fig. 3 display the twisting dispersion curves, in which only the dipolar coupling effect is taken into account; that is, $\alpha = 0$ and $\beta = 0$. The best fit is achieved with $\kappa_E = 0.2$ and $\kappa_H = 0.09$. Obviously, despite the fact that the grey curves can fit most parts of the numerical data, no avoided crossing is predicted. Instead, the ω^+ and ω^- branches converge at φ_t. Therefore, it has to be emphasized that although the electric and magnetic dipolar interactions are the essential mechanisms, the higher-order electric multipolar interactions should also be carefully considered for fully understanding the origin of the spectral characteristics of the stereometamaterial systems.

The angle where the avoided crossing occurs in the twisting dispersion spectrum is correlated with the geometry of the SRRs as well as the vertical distance between the two SRRs. For the specific stereo-SRR dimer metamaterials we investigated here, the avoided crossing appears at ~60°. Based on detailed simulated field distribution studies, we found that this angle is also a transition angle where the higher and lower frequency modes exchange their magnetic dipole alignments from parallel to antiparallel. At angles smaller than angle φ_t, the two magnetic dipoles are aligned parallel (antiparallel) at resonance ω^+ (ω^-). The electric coupling effect dominates in this regime. With continuous increase of the twist angle, due to the displacement of the two SRRs, the electric coupling contributes less effectively. Consequently, the splitting of the two resonance branches starts to decrease. This situation remains until the transition angle is reached, where the electric and magnetic dipole–dipole interactions cancel one another. The higher-order electric multipolar interactions account for the avoided crossing of the two resonance branches. After angle φ_t, the electric coupling continues to decrease. As a result, the resonance levels are determined according to the scheme of magnetic dipole–dipole coupling, that is, the parallel and antiparallel alignments of the magnetic dipoles in the two SRRs correspond to the lower and higher frequency resonances, respectively. When the twist angle reaches 90°, the electric coupling quenches and is negligible. This represents a purely magnetic dipole–dipole coupling situation. Subsequently, with further increase of the twist angle, the displacement of the two SRRs is reduced and the electric coupling comes into play again. Because of the orientation of the two SRRs, the electric and magnetic coupling can contribute positively, giving rise to a larger splitting of the two resonance branches with increasing twist angle. The splitting finally reaches its maximum at $\varphi = 180°$.

The structures of stereometamaterials are compatible with nanofabrication stacking techniques[7,9]. We fabricated three stereo-SRR dimer metamaterials with specific twist angles $\varphi = 0$, 90 and 180°, as illustrated in the insets of Fig. 1b–d. In the experiment, the structures were fabricated on a glass substrate. Gold SRRs were embedded in a photopolymer (PC403), which served as the dielectric spacer. A spacer of $s = 120$ nm was applied in order to achieve surface planarization for stacking the second SRR layer. The electron micrographs of the fabricated SRR dimer metamaterials were obtained by field-emission scanning electron microscopy. Figure 4a–c presents oblique views of the 0, 90 and 180° twisted SRR dimer metamaterials, in which the underlying SRRs are clearly visible. The insets of Fig. 4a–c show the normal views, demonstrating the good accuracy of lateral alignment for the different SRR layers. To experimentally investigate the optical properties of these SRR dimer metamaterials, the near-infrared transmittance spectra of the samples at normal incidence were measured by a Fourier-transform infrared spectrometer with electric field polarization as illustrated in Fig. 1. The measured transmittance spectra are presented by black curves in Fig. 4d–f and the simulated spectra as red dashed curves. The resonance positions are redshifted compared to those of the corresponding resonances in Fig. 1b–d due to the presence of glass substrate and dielectric spacers. For a reasonable comparison with the experiment, in the simulations in Fig. 4d–f, gold with a three times higher damping constant as that used in Fig. 1b–d was used to account for the surface scattering and grain boundary effects in the thin film of the real systems[17]. The overall qualitative agreement between experimental and simulated results is quite good. The discrepancies are most likely due to tolerances in fabrication and assembly, as well as significant broadening in the experiment. For 0° and 180° twisted SRR dimer structures, the lower resonances ω_0^- and ω_{180}^- are less distinctly visible than the higher resonances ω_0^+ and ω_{180}^+, respectively (see spectra in Fig. 4d,f). This is due to the fact that for both dimer structures, the electric coupling plays a key role. At the lower resonance frequencies (ω_0^- and ω_{180}^-), the electric dipoles in the two SRRs oscillate anti-phase. Such resonances are not easily excited by light. On the other hand, at the higher resonance frequencies (ω_0^+ and ω_{180}^+), the electric dipoles in the two SRRs oscillate in-phase. Such resonances can strongly couple to light. For the 90° twisted SRR dimer structure, the splitting of the resonances is clearly observable when an analyser is applied behind the sample, which is rotated by 75° with respect to the polarization of the incident light. This is due to the polarization rotation effect arising from the chirality[18,19] of the 90° twisted structure.

The new concept of stereometamaterials adds a significant degree of freedom through the interplay of electric and magnetic interactions, and tremendously enhances the versatility of nanophotonic structures. Stereometamaterials allow us to use higher-order electric multipolar as well as magnetic interactions, which can be nearly as large as the electric dipolar interaction. This is completely different from molecules, where electric dipolar interaction is the essential contribution determining optical properties. It will also be interesting to study the geometry and distance dependence of the different coupling effects. Our concept can be extended to more complex artificial molecules, such as stereotrimers, stereoquadrumers and so on. The tuneability of the resonant behaviour of these new artificial materials by altering the spatial arrangement of their constituents offers great flexibility for exploring useful metamaterial applications, such as chiral structures with negative refraction[20], invisibility cloaks[21] and magneto-optically active materials[22]. Stereometamaterials open up the potential for optical polarization control, which so far has been dominated by stereoisomers[1] and liquid crystals[23]. (See Supplementary Information for more details on optical stereoisomers as well as left- and right-handed enantiomers.) Stereometamaterials might also serve as artificial nanosystems for emulating the optical properties of complex biomolecules, such as double helix DNA chiral proteins and drug enzymes, which have profound application potentials in biophotonics, pharmacology, as well as diagnostics.

Methods

Structure fabrication. Three (or more) gold alignment marks (size 4 × 100 μm) with a gold thickness of 250 nm were first fabricated using a lift-off process on a quartz substrate. The substrate was then covered with a 50-nm gold film using electron-beam evaporation. Next, SRR structures were defined in negative resist (AR-N, ALLRESIST GmbH) by electron-beam lithography. Ion beam etching (Ar^+ ions) of the gold layer was then performed to generate the gold SRR structures. Subsequently, a 120-nm-thick spacer layer was applied on the first layer by spin-coating. A solidifiable photopolymer, PC403 (JCR), was used as the planarized spacer layer. A pre-baking process in which the baking temperature was continuously increased from 90 to 130 °C was first performed to remove the solvent from the polymer. A sufficiently long bake at a higher temperature (30 min in a 180 °C oven) further hardened the layer. A 50-nm gold film and a spin-coated AR-N resist layer were subsequently deposited on the sample. Next, the stacking alignment using the gold alignment marks was applied to ensure accurate stacking of the second SRR layer. The procedures of in-plane fabrication were repeated with the final layer being PC403. All structures had a total area of 200 × 200 μm.

Optical and structure characterization. Transmittance spectra were measured with a Fourier-transform infrared spectrometer (Bruker IFS 66v/S, tungsten lamp) combined with an infrared microscope (×15 Cassegrain objective, NA = 0.4, liquid

N_2-cooled MCT 77 K detector, infrared polarizer). The measured spectra were normalized with respect to a bare glass substrate.

The simulated transmittance spectra and field distributions were performed using the software package CST Microwave Studio. For the spectra in Fig. 1b–d, the permittivity of bulk gold in the infrared spectral regime was described by the Drude model with plasma frequency $\omega_{pl} = 1.37 \times 10^{16}\ s^{-1}$ and the damping constant $\omega_c = 4.08 \times 10^{13}\ s^{-1}$. For the spectra in Fig. 4d–f, owing to the surface scattering and grain boundary effects in the thin film of the real systems, the simulation results were obtained using a damping constant that was three times larger than the bulk value. The optical parameters were the refractive index of PC403 $n_{PC403} = 1.55$ and the quartz substrate refractive index $n_{glass} = 1.5$.

The electron micrographs of the fabricated structures were taken with an FEI-Nova Nanolab 600 scanning electron microscope.

Received 13 October 2008; accepted 21 January 2009; published online 22 February 2009

References

1. Robinson, M. J. T. *Organic Stereochemistry* (Oxford Univ. Press, 2000).
2. Smith, D. R., Pendry, J. B. & Wiltshire, M. C. K. Metamaterials and negative refractive index. *Science* **305,** 788–792 (2004).
3. Soukoulis, C. M., Linden, S. & Wegener, M. Negative refractive index at optical wavelengths. *Science* **315,** 47–49 (2007).
4. Shalaev, V. M. Optical negative-index metamaterials. *Nature Photon.* **1,** 41–48 (2007).
5. Veselago, V. G. The electrodynamics of substances with simultaneously negative values of ε and μ. *Sov. Phys. Usp.* **10,** 509–514 (1968).
6. Pendry, J. B. Negative refraction makes a perfect lens. *Phys. Rev. Lett.* **85,** 3966–3969 (2000).
7. Liu, N. *et al.* Three-dimensional photonic metamaterials at optical frequencies. *Nature Mater.* **7,** 31–37 (2008).
8. Liu, N. *et al.* Plasmon hybridization in stacked cut-wire metamaterials. *Adv. Mater.* **19,** 3628–3632 (2007).
9. Liu, N., Fu, L. W., Kaiser, S., Schweizer, H. & Giessen, H. Plasmonic building blocks for magnetic molecules in three-dimensional optical metamaterials. *Adv. Mater.* **20,** 3859–3865 (2008).
10. Prodan, E., Radloff, C., Halas, N. J. & Nordlander, P. A hybridization model for the plasmon response of complex nanostructures. *Science* **302,** 419–422 (2003).
11. Wang, H., Brandl, D. W., Le, F., Nordlander, P. & Halas, N. J. Nanorice: a hybrid plasmonic nanostructure. *Nano Lett.* **6,** 827–832 (2006).
12. Nordlander, P., Oubre, C., Prodan, E., Li, K. & Stockman, M. I. Plasmon hybridization in nanoparticle dimers. *Nano Lett.* **4,** 899–903 (2004).
13. Liu, N., Kaiser, S. & Giessen, H. Magnetoinductive and electroinductive coupling in plasmonic metamaterial molecules. *Adv. Mater.* **20,** 4521–4525 (2008).
14. Liu, H. *et al.* Magnetic plasmon hybridization and optical activity at optical frequencies in metallic nanostructures. *Phys. Rev. B* **76,** 073101 (2007).
15. Rockstuhl, C. *et al.* On the reinterpretation of resonances in split-ring-resonators at normal incidence. *Opt. Express* **14,** 8827–8836 (2006).
16. Hao, F. *et al.* Shedding light on dark plasmons in gold nanorings. *Chem. Rev. Lett.* **458,** 262–266 (2008).
17. Zhang, S. *et al.* Demonstration of metal–dielectric negative-index metamaterials with improved performance at optical frequencies. *J. Opt. Soc. Am. B* **23,** 434–438 (2006).
18. Rogacheva, A. V., Fedotov, V. A., Schwanecke, A. S. & Zheludev, N. I. Giant gyrotropy due to electromagnetic-field coupling in a bilayered chiral structure. *Phys. Rev. Lett.* **97,** 177401 (2006).
19. Decker, M., Klein, M. W., Wegener, M. & Linden, S. Circular dichroism of planar chiral magnetic metamaterials. *Opt. Lett.* **32,** 856–858 (2007).
20. Pendry, J. B. A chiral route to negative refraction. *Science* **306,** 1353–1355 (2004).
21. Schurig, D. *et al.* Metamaterial electromagnetic cloak at microwave frequencies. *Science* **314,** 977–980 (2006).
22. Svirko, Y. P. & Zheludev, N. I. *Polarization of Light in Nonlinear Optics* (Wiley, 1998).
23. Scharf, T. *Polarized Light in Liquid Crystals and Polymers* (Wiley, 2007).

Acknowledgements

The authors would like to thank M. Stockman, T. Pfau, F. Giesselmann and M. Dressel for useful discussions and comments. We thank S. Linden for stimulating us to study the twisted SRRs with different angles. We acknowledge S. Hein for his metamaterial visualizations. We gratefully thank M. Hirscher and U. Eigenthaler at the Max-Planck-Institut für Metallforschung for their electron microscopy support. We acknowledge S. Kaiser, H. Graebeldinger and M. Ubl for technical assistance. This work was financially supported by Deutsche Forschungsgemeinschaft (SPP1113 and FOR557), Landesstiftung BW and BMBF (13N9155 and 13N10146). The research of H.L. and S.Z. was financially supported by the National Natural Science Foundation of China (no. 10604029, no. 10704036 and no. 10874081) and the National Key Projects for Basic Researches of China (no. 2009CB930501, no. 2006CB921804 and no. 2004CB619003).

Additional information

Supplementary Information accompanies this paper at www.nature.com/naturephotonics. Reprints and permission information is available online at http://npg.nature.com/reprintsandpermissions/. Correspondence and requests for materials should be addressed to H.G.

nature photonics

ARTICLES

PUBLISHED ONLINE: 22 FEBRUARY 2009 | DOI: 10.1038/NPHOTON.2009.21

III-nitride photonic-crystal light-emitting diodes with high extraction efficiency

Jonathan J. Wierer, Jr[1], Aurelien David[1]* and Mischa M. Megens[2]

Light-emitting diodes are becoming an increasingly attractive alternative to conventional light sources due to their small size, high efficiency and long lifetime. Ongoing research is dedicated to improving their performance through the use of more efficient light-generating and light-extracting structures. Here, we demonstrate light-emitting diodes achieving high extraction efficiency by using photonic crystals. The structures are III-nitride thin-film light-emitting diodes emitting at $\lambda = 450$ nm. The photonic-crystal layer provides superior optical mode control compared to conventional III-nitride light-emitting diodes, efficiently coupling guided modes out of the light-emitting diode. Fabry–Perot and photonic-crystal induced modes are observed in the far-field radiation patterns and are matched to theoretical electromagnetic calculations. The optical mode control results in a high-performance light-emitting diode with an estimated unencapsulated light extraction of ~73%, higher than any unencapsulated III-nitride light-emitting diode measured to date.

Light-emitting diodes (LEDs), and in particular III-nitride LEDs, have progressed from being low-power indicators to high-power light sources. High-efficiency power LEDs are now commercially available with efficacies surpassing those of conventional light sources, bringing the world closer towards the realization of the ultimate lamp[1]. The efficiency breakthroughs are partly due to improvements in the internal quantum efficiency of III-nitrides, although further work is necessary to fix the decrease in efficiency with increased current[2]. The other factor enabling high-efficiency III-nitride LEDs has been the progress in the light extraction and operating power density of LEDs; they have evolved from simple top-emitting structures[3] to flip-chip LEDs[4], and now to thin-film rough-surface LEDs[5,6]. These LEDs are capable of high-power operation (3 W into a device of 1 mm^2 area) with low thermal resistance. Although rough-surface LEDs offer high extraction efficiency, they provide little control on how the textured extracting surface directs the light out of the LED, resulting in Lambertian radiation patterns. In addition, the extraction efficiency, although quite high (~80%) for an encapsulated device, is much lower into air (~65%)[7].

Encapsulating a rough thin-film LED increases the extraction efficiency but presents some drawbacks. First, all currently used encapsulants are organic-based and turn opaque at high flux density, eventually hindering higher power densities. Second, the encapsulant increases the optical size of the source by a factor of approximately two due to its larger index, decreasing the surface brightness of the source. Therefore, a high-extraction-efficiency unencapsulated device is desirable for high-power and high-brightness applications.

Using photonic crystals in LEDs is a possible next step for improved performance. Photonic crystals are dielectric perturbations on the scale of the wavelength, offering control of the way light propagates in the medium[8]. Photonic crystals can be used to increase the extraction efficiency[9,10] and enhance the internal quantum efficiency by means of the Purcell effect[11].

In refs 9 (theory) and 10 (experiment) the so-called bandgap approach is studied; the photonic crystal penetrates through the entire device and is tuned near a photonic bandgap, inhibiting light emission into guided modes and hence increasing extraction efficiency. Although surface recombination is low in III-nitrides compared to other III–V compounds[12], it is still difficult to achieve a working device in which the photonic crystal penetrates through the active region. Besides, obtaining an omnidirectional bandgap is challenging due to the relatively low refractive index of GaN and the thickness of typical epitaxial layers, and so far bandgaps have only been demonstrated in membrane geometries[13].

Most scientific efforts have therefore focused on another approach: using photonic crystals as diffraction gratings. In this scheme, spontaneous emission into guided modes is allowed but these modes are subsequently outcoupled by the diffractive properties of the photonic crystal. The lattice constant of a diffractive photonic crystal is larger than in the bandgap approach—the photonic crystal operates near a high Bragg order rather than at the first Bragg order[14]. Several groups have demonstrated III-nitride LEDs with photonic-crystal diffractive layers on the surfaces of the LEDs, showing an improvement in light extraction[15–18] and in the control of the radiation pattern[16]. In the diffraction grating approach, controlling and extracting all the guided modes is a difficult task. Each guided mode propagates in the GaN at a different angle and therefore interacts with the photonic crystal differently. Having all the modes diffract is non-trivial and requires proper optimization for high extraction efficiency[19].

Although there have been various demonstrations of photonic-crystal LEDs, there has yet to be a photonic crystal LED that competes with the best non-photonic-crystal LEDs. This article demonstrates a high-performance unencapsulated III-nitride thin-film photonic-crystal LED with light extraction efficiency rivalling that of all other unencapsulated III-nitride device designs. The extraction process is explained qualitatively and is confirmed quantitatively by electromagnetic modelling. Finally, a high-efficiency device is demonstrated and its light extraction efficiency estimated.

Mode control and light extraction

The typical emission pattern within a flip-chip LED with InGaN–GaN multi-quantum wells is shown in Fig. 1a. The GaN slab is bonded to a reflector, with multi-quantum wells placed close (approximately one optical thickness) to the reflector. We consider a 700-nm-thick LED for comparison with the experimental data

[1]Advanced Laboratories, Philips Lumileds Lighting Co., 370 W. Trimble Road, San Jose, California 95131, USA, [2]Philips Research, Philips, High Tech Campus 4, 5656 AA Eindhoven, The Netherlands; *e-mail: aurelien.david@philips.com

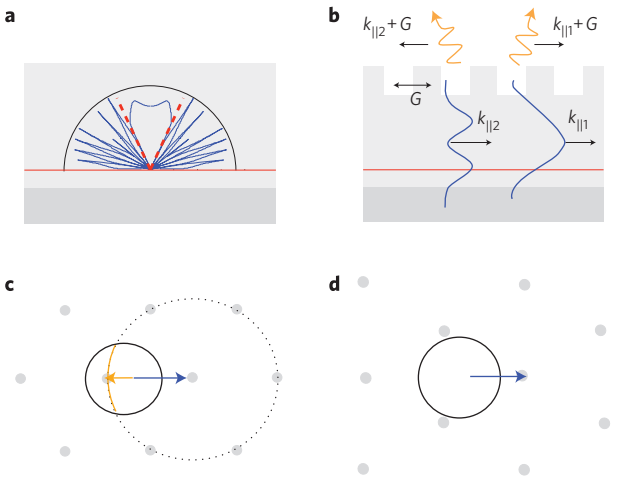

Figure 1 | Light emission and extraction. a, Internal emission pattern (blue line) of the emitting InGaN quantum well in a planar GaN slab with a reflective silver mirror. The emission pattern represents the emission intensity versus polar angle (in log scale). The red dashed lines correspond to the extraction cone. **b**, Guided modes in the same structure with a photonic-crystal layer—here, modes TE1 and TE2 are depicted. Each guided mode possesses a wavevector $k_{||}$ (blue line) that can be coupled to a leaky harmonic $k_{||}+G$ (yellow line). **c**,**d**, Ewald constructions for a mode propagating along the ΓM (**c**) and ΓK (**d**) directions of a photonic crystal, respectively. In **c** the arc of the circle is the locus of the diffracted harmonic when the azimuthal angle of the mode varies.

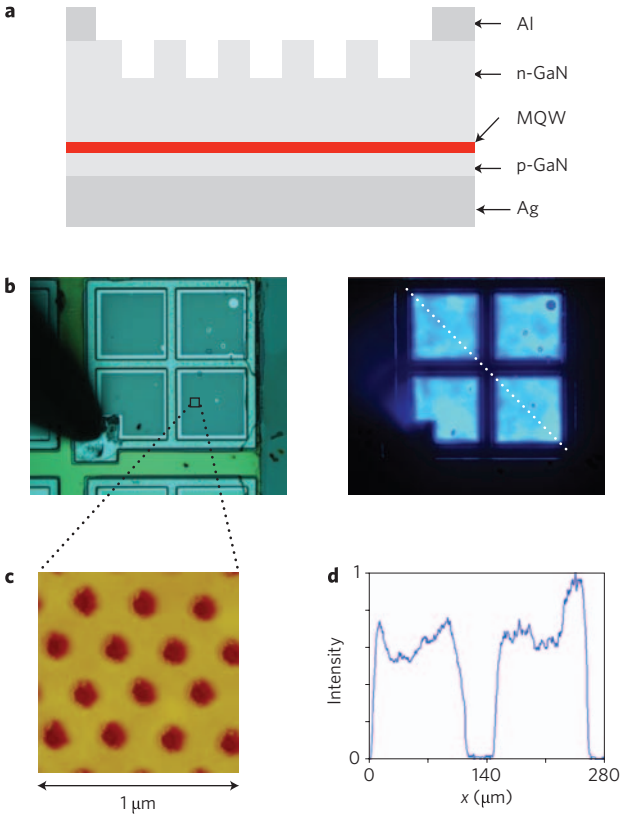

Figure 2 | Device design. a, Schematic cross-section of the device. **b**, Top view of unbiased (left) and biased (right) photonic-crystal LEDs. The LED sides are ~200 μm in length. **c**, Top-view atomic force microscope image of the triangular lattice photonic crystal. **d**, Cross-section of the light intensity profile corresponding to the white dotted line of Fig. 2b (right).

below. The emission pattern comprises two angular regions. The first region is light emitted within the extraction cone (or air cone) defined by

$$\theta_c = \sin^{-1}(n_{\mathrm{air}}/n_{\mathrm{GaN}}) \approx 24.6^{\circ} \quad (1)$$

where n_{air} and n_{GaN} are the indices of air and GaN. The pattern in the extraction cone displays broad-shaped lobes whose peaks correspond to the Fabry–Perot resonances between the GaN–reflector and GaN–air interfaces. These modes will appear as broad resonances in the far-field radiation patterns typical of resonant- (or micro-) cavity LEDs[20]. Outside the extraction cone, light is emitted in a set of sharp guided modes that propagate within the GaN slab. The number of these modes increases with slab thickness and their sharpness (finesse) is a function of the material losses and reflectivity of the interfaces. For a planar LED these guided modes are lost or only collected on the edges of the LED, limiting the light extraction efficiency of a resonant-cavity LED. According to one-dimensional calculations[21], extraction efficiency to air for a resonant-cavity LED is limited to ~30%.

Figure 1b shows how a photonic-crystal layer diffracts these guided modes into air, increasing extraction efficiency. Each of the guided modes can be characterized by an in-plane wavevector ($k_{||m}$), related to the angle of propagation within the GaN (θ_m) by

$$k_{||m} = (2\pi/\lambda)n_{\mathrm{GaN}}\sin(\theta_m) \approx \sqrt{[((2\pi/\lambda)n_{\mathrm{GaN}})^2 - (m\pi/L)^2]} \quad (2)$$

where m is the mode number (1, 2, 3...), λ is the wavelength of light, and L is the thickness of GaN.

In the presence of the photonic crystal, the guided modes become Bloch modes and the wavevectors $k_{||m}$ are now coupled to other harmonics $\{k_{||m}+G\}$ by the reciprocal lattice vectors G. To diffract the guided light into air, the lattice constant a of the photonic crystal needs to satisfy the diffraction condition

$$|k_{||m} + pG_0| < \frac{2\pi}{\lambda} \quad (3)$$

where $G_0 = 2\pi/a$ and p is an integer (determining which harmonic is responsible for diffraction to air). The Bloch mode is then referred to as a leaky mode, because its power leaks to air as it propagates. In air, the radiated harmonic behaves like a plane wave with an angle

$$\theta_{m,\mathrm{air}} = \sin^{-1}((\lambda/2\pi)|k_{||m} + pG_0|) \quad (4)$$

The diffraction condition depends on the wavelength, lattice constant and mode propagation angle. In practice, an LED supports a few to several tens of modes (depending on the GaN thickness) and a wavelength range $\Delta\lambda \approx 20$–50 nm. For high extraction efficiency it is necessary to extract guided light propagating in all azimuthal directions. Therefore, a two-dimensional photonic crystal is required. Figure 1c,d shows a top view of a triangular photonic crystal in reciprocal space (Ewald construction[19]) for the same mode propagating along two azimuthal directions. The grey dots are the reciprocal lattice points of the photonic crystal with the lattice rotated 90° between Fig. 1c and d, and the full circle describes the air extraction cone. For a mode (blue arrow) propagating along the ΓM direction in Fig. 1c the diffraction condition is met: a harmonic falls in the air cone (orange arrow) and the mode becomes leaky. The mode along ΓK in Fig. 1d remains guided because no reciprocal lattice point lies within the air cone. In general, when

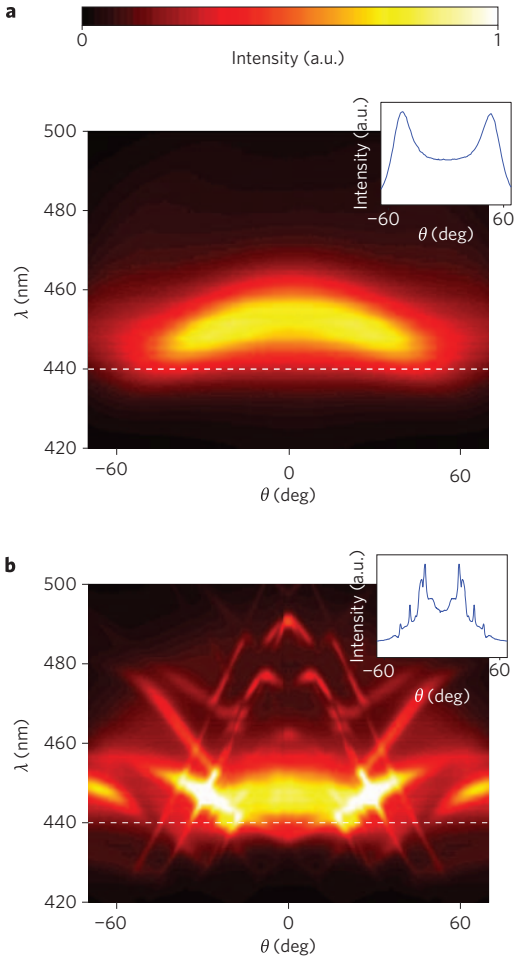

Figure 3 | Wavelength-resolved angular far-field patterns. a, Measured TM-polarized far-field pattern versus angle θ (0° corresponding to vertical emission) and wavelength for a planar LED. **b**, Measured TM-polarized far-field pattern for a photonic-crystal LED in the ΓK direction (pitch $a = 250$ nm). Insets are plots at a single wavelength at 440 nm, marked by dashed lines.

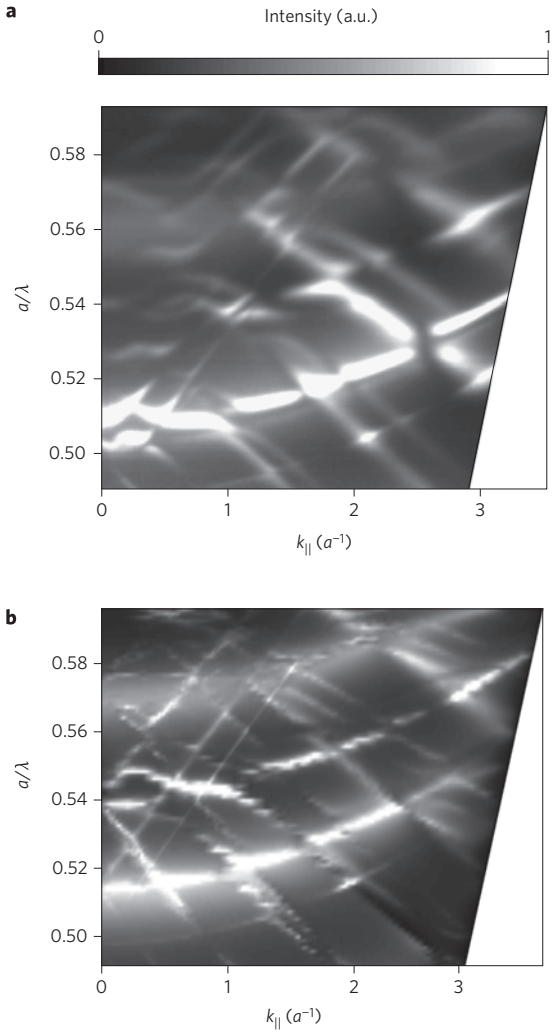

Figure 4 | Normalized band structures. a, Experimental band structure for the photonic-crystal LED of Fig. 3b, obtained after normalization by the LED's lineshape. **b**, Corresponding calculated band structure obtained by the S-matrix method.

the azimuthal angle of the guided mode is varied, reciprocal lattice points describe a circular locus (dashed circle of Fig. 1c). The part of this locus that is inside the air cone can be diffracted, resulting in the arc of the circle in Fig. 1c. Thus the type and lattice constant of the photonic crystal need to be chosen properly, ideally to ensure extraction of all modes at all angles.

All the above considerations are geometrical and aim at ensuring that the diffraction condition is met for as many modes and angles as possible. Another issue is that of the efficiency of the extraction phenomenon. The multimode nature of GaN layers makes this question non-trivial[22,23], and in general the vertical structure has to be engineered to allow good coupling of leaky modes with the photonic crystal. In general, high-order modes are better diffracted than low-order modes because of a higher overlap with the photonic crystal. Here, thin-film LEDs are used to ensure good photonic coupling[18]. As well as the vertical design, extraction efficiency can also be influenced by other parameters such as the depth and size of holes[19].

Photonic characterization of devices

The devices studied in this article are thin-film LEDs with a surface photonic crystal layer, as shown in Fig. 2. The details of their fabrication are described in the Methods. Some LEDs are kept unpatterned for reference.

This section discusses how far-field measurements can be used to measure scattering by the photonic crystal. Such measurements can assist in the design of an efficient photonic-crystal LED: the presence and position of modes reveals which modes undergo diffraction to air (guiding the choice of the photonic-crystal pitch and lattice type), while their intensity indicates how efficient the extraction mechanism is (which can indicate excessive losses in the structure, or poor extraction efficiency of some of the modes).

Figure 3 shows transverse magnetic (TM) polarized angular far-field radiation patterns for both a planar (Fig. 3a) and a photonic-crystal LED (Fig. 3b) in the ΓK crystal direction. Plotted in the insets are the monochromatic radiation patterns at 440 nm. Both LEDs have the same GaN slab thickness and the multi-quantum wells' emission peaks at 450 nm. The lattice constant of the triangular photonic crystal is $a = 250$ nm. For the planar LED, only light emitted directly within the air cone appears in the radiation pattern. As expected from Fig. 1a, the radiation pattern has broad lobes corresponding to the Fabry–Perot resonances within the GaN cavity. These resonances shift with wavelength. Here, one Fabry–Perot resonance is observed within the emission linewidth.

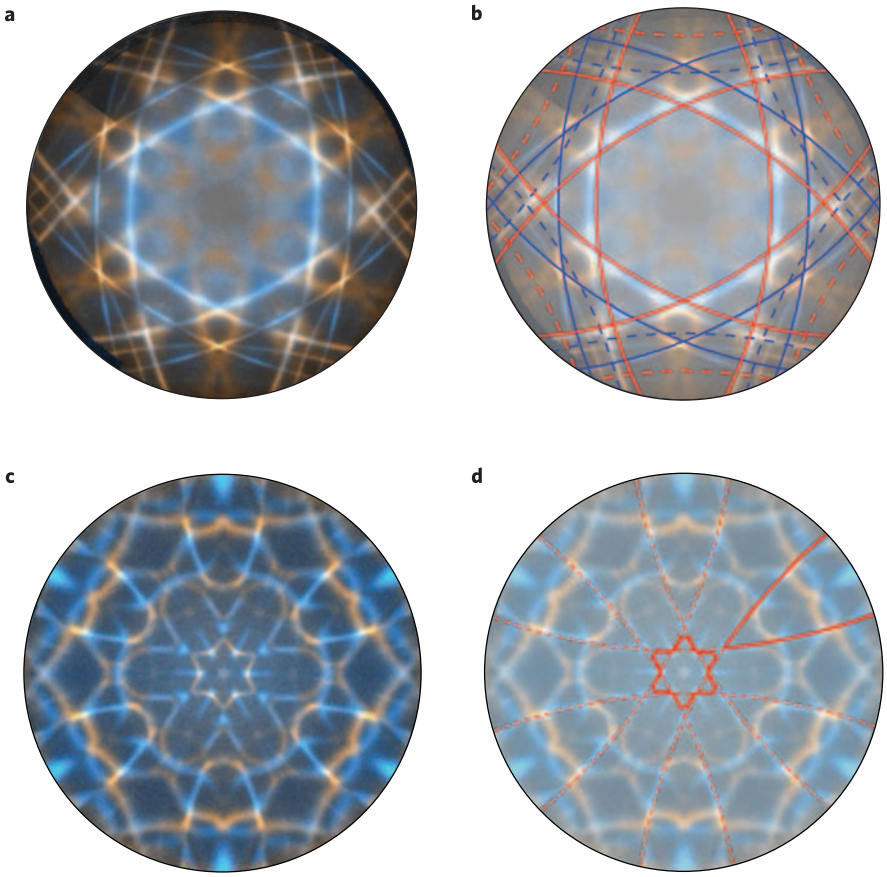

Figure 5 | θ–ϕ resolved experimental far-field patterns of photonic-crystal LEDs at a wavelength of 480 nm. a, Photonic-crystal LED with a lattice constant $a = 315$ nm and weak photonic strength. Blue and yellow lines correspond to TE and TM polarizations. **b**, Same as **a**, with a Ewald construction superimposed considering only two modes (effective indices 2.39 and 2.22). The full lines correspond to folding by the shortest reciprocal lattice vector (ΓM diffraction), and the dashed lines by the second shortest vector (ΓK diffraction). **c**,**d**, Same as **a**,**b** with the LED of Figs 3 and 4, with shorter lattice constant ($a = 250$ nm) and a strong photonic strength. The Ewald construction schematically shows how anti-crossings yield a more complex dispersion in the case of strong photonic coupling.

The photonic crystal LED is markedly different, with sharp peaks superimposed on top of the Fabry–Perot resonances. As described above, each peak corresponds to a guided mode diffracted into air by the photonic crystal. The angles of these modes shift with wavelength following equation (4). The leaky modes tend to be more intense close to the Fabry–Perot resonances, suggesting a resonant effect within the cavity for the diffraction efficiency of the leaky modes.

From these measurements, we derive the photonic band structure (Fig. 4) as described in the Methods section. The same features observed in Fig. 3b are present, namely the contributions of the Fabry–Perot and leaky modes. The dispersion of these modes now appears clearly due to the removal of the effect of the lineshape. For the leaky modes the dispersion is complex, unlike previous work with a small photonic-crystal perturbation[22,23] where the dispersion was simply that of folded free-photon modes. Here rather, the effect on dispersion is strong and manifests stronger photonic coupling, as already observed in ref. 18. For instance, strong anti-crossing of some photonic bands is present.

To quantitatively confirm our understanding of the band structures, numerical modelling was performed using an S-matrix algorithm with an embedded dipole source[24,25]. Unlike previous work where only the position of the leaky modes was matched[18,22,23], this method directly yields the emission pattern of the modelled LED. The result of the calculation is shown in Fig. 4b. Most features of the experimental emission pattern are well reproduced, including the position and dispersion of the Fabry–Perot modes. The slight discrepancy regarding the leaky mode intensity may be attributed to imperfect knowledge of the structure's details (we used nominal thicknesses, only allowing small variations of ± 10 nm to better match the modes' positions). Band anti-crossings also appear, with a magnitude similar to that observed experimentally.

The previous discussion only pertains to the ΓK direction. To characterize the full far-field pattern, θ-dependent patterns similar to those in Fig. 3 are repeated for all values of the azimuthal angle ϕ. These patterns are then collected, giving access to the far-field pattern for all angles and wavelengths. Figure 5a displays such a θ–ϕ pattern at a wavelength of 480 nm, and for a photonic-crystal LED with a triangular lattice ($a = 315$ nm) and a relatively shallow etch depth. The pattern has a sixfold symmetry characteristic of the triangular lattice. The leaky modes are sharp arcs of circles, corresponding to the loci of the reciprocal lattice points, as sketched in Fig. 1c. In Fig. 5b the same Ewald construction as in Fig. 1c is performed: the dispersion of leaky modes is well reproduced by considering two modes (a third mode is faintly seen in the measurement, but not fitted for clarity). Because this LED operates at a high reduced frequency $a/\lambda \approx 0.65$, not only the six nearest neighbours in the reciprocal space (full circles) were considered, but also the six second-nearest neighbours (dashed circles). This LED does not display marked anti-crossings, indicating a weak photonic interaction. On the other hand, when the same measurement was performed on the LED shown in Figs 3 and 4 (at the same

wavelength, with a lattice constant $a = 250$ nm, and a deeper photonic crystal), the pattern becomes more complex, as seen in Fig. 5c. Although the sixfold symmetry is still present, the loci of leaky modes are more intricate due to band anti-crossings, confirming the stronger photonic interaction. Figure 5d qualitatively demonstrates how the dispersion of free photons (dashed lines, similar to the case of Fig. 5b) is split by anti-crossings, yielding a star-shaped monster at the centre of the photonic Fermi surface (see ref. 26 for a similar discussion). In terms of light extraction, the importance of the choice of photonic-crystal pitch is seen here. For the LED with $a = 315$ nm (Fig. 5a) no mode is scattered close to normal incidence; all leaky harmonics are diffracted at the edge of the extraction cone, making a rather inefficient use of the extraction cone. A situation where harmonics are well spread over the cone, such as in Fig. 5c, is more desirable. This happens close to a Bragg condition, when one of the reciprocal lattice points falls near the centre of the extraction cone.

Device performance

Various parameters contribute to device performance, such as the thickness of the epitaxial layers, and the type, depth, filling factor and pitch of the photonic crystal. Deterministic theoretical optimization is hard to achieve in this large parameter space: as soon as more than one or two guided modes are present, a detailed mode-by-mode analysis is tedious, especially with the averaging over azimuthal angles and wavelength.

Therefore, in this work we experimentally spanned a parameter space centred on reasonable parameter values as described in the Methods section. The best LED we measured in our parameter space had a total GaN thickness of ~700 nm; the photonic crystal was an Archimedean A13 lattice[14] with a lattice constant of 455 nm, a filling factor $f \approx 0.3$ and a depth of 250 nm. Figure 6a shows the measured external quantum efficiency η_{eqe} and total output power versus current for this LED emitting into air. The peak η_{eqe} is 47% at ~2 mA (~7.5 A cm^{-2}) and η_{eqe} is 36% at 20 mA (~75 A cm^{-2}). The forward voltage at 20 mA is 4.5 V. This forward voltage is higher than state-of-the-art LEDs due to the thinner n-GaN layers used here, but is comparable to LEDs of the same thickness without the photonic crystal.

Deriving the extraction efficiency C_{ex} requires determination of the internal quantum efficiency η_{int}:

$$C_{ex} = \eta_{eqe}/\eta_{int} \quad (5)$$

where the radiative recombination efficiency and injection efficiency are included in η_{int}. Measuring η_{int} for LEDs is difficult, so two methods are used to determine η_{int}. In both cases, we consider a simple planar geometry where light extraction efficiency can be accurately modelled (within ~1%), so that internal quantum efficiency can be derived from the output power.

The first method uses a small silver p-contact on the GaN LED wafer still containing the sapphire growth substrate. The n-contact is formed by a simple process to complete the device. Power is measured into a known emission angle under electrical injection, enabling estimation of the extraction efficiency and hence the η_{int} of the LED wafer. The result is a peak η_{int} of 60%. The second method measures the power output from a planar resonant-cavity LED neighbouring the best photonic-crystal LED. Its total GaN thickness is the same. Using the resonant-cavity model of ref. 21, we derive a C_{ex} of 27% for this device. Figure 6b shows the η_{eqe}, power and η_{int} versus current density for the thin-film resonant-cavity LED. Using the η_{eqe} from this resonant-cavity LED, the estimated peak η_{int} is 69%. This range of η_{int} (60–69%) is expected from this type of epitaxial structure, and is also compatible with a third method of measuring η_{int}, low-temperature photoluminescence measurements (data not shown).

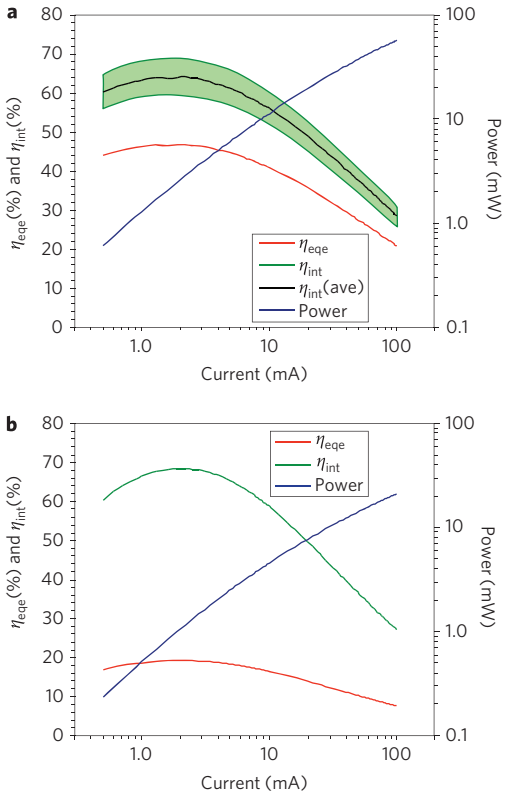

Figure 6 | Performance of devices. a, External quantum efficiency (red line), total light output power (blue line), estimated bounds for the internal quantum efficiency (green area), and average internal quantum efficiency (black line) versus current of a tuned high-performance photonic-crystal LED emitting into air. **b**, External quantum efficiency, total light output power and internal quantum efficiency for a planar resonant-cavity LED neighbouring the photonic-crystal LED of **a**. The internal quantum efficiency is obtained by modelling the light extraction efficiency.

Returning to the best-performing photonic-crystal LED, this value of η_{int} yields a range of $C_{ex} = 68–78\%$, or an average C_{ex} of 73%. Figure 6a shows the two bounds for η_{int} obtained from the two methods above, and the average η_{int}, versus injection current.

Let us now discuss the high performance obtained with this design. The low-loss Ag mirror ensures low metal absorption. The thin GaN layer (700 nm) supports about seven guided modes (as seen in Fig. 1a), and is thin enough that the interaction of these modes with the photonic crystal is expected to be good (all modes overlap well with the photonic-crystal layer, yielding a good extraction efficiency[18]). The pitch is large enough (455 nm) that all modes are located above the air cone (all modes are leaky), no matter what their azimuthal angle of propagation. Therefore, all of the emitted light is prone to light extraction in this structure. Conversely the use of an Archimedean A13 lattice ensures that diffraction mostly happens to 'useful' reciprocal lattice points directed to air, and limits diffractions directed only towards the metallic mirror[14,27]. The precise value of the photonic-crystal pitch, depth and GaN layer further interact in a non-trivial way to yield high performance for the measured device, which warrants our approach based on scanning a parameter space centred on reasonable values (see Supplementary Information for a discussion of the pitch value).

We also model the extraction efficiency for the photonic-crystal LED structure using the same S-matrix method as above. We obtain $C_{ex} \approx 70–75\%$ (the uncertainty being due to imperfect knowledge of the structure), in good agreement with the experimental value.

The simulation also indicates that the non-extracted light is roughly equally divided between re-absorption in the multi-quantum well and the metallic mirror. We note that metal losses are not related to surface plasmon absorption; indeed, the p-layer is ~100 nm thick, which is too large for radiative coupling of the multi-quantum well with plasmons, and the photonic crystal is even farther from the mirror, preventing evanescent coupling to plasmons through the photonic crystal (the typical decay length of plasmons at a GaN/Ag interface is ~20 nm).

The photonic-crystal LED extraction efficiency compares favourably with rough-surface thin-film LEDs, where C_{ex} is ~65% for an unencapsulated device[7]: our best data show a non-encapsulated thin-film photonic-crystal LED design that is capable of higher extraction efficiencies than any unencapsulated III-nitride LED demonstrated to date. This is an encouraging result for encapsulation-free devices, for which reliability risks and degradation of organic-based encapsulants are no longer issues. An unencapsulated design is also of interest for its high brightness (the optical source size is reduced by n^2). Compared with an encapsulated rough-surface LED where the extraction efficiency is 80%, the brightness is increased by a factor of 2 in our best performing photonic-crystal device.

Conclusion

Superior optical mode control is demonstrated by combining thin-film and photonic-crystal layers in III-nitride LEDs. The thin film enables control of the emission into the extraction cone, and the photonic crystal allows for extraction of guided modes. Measured far-field radiation patterns are fit using an S-matrix calculation to demonstrate how the modes are controlled and extracted from the structure. Within the parameter range investigated, the best photonic-crystal LED has a very high light extraction efficiency (73%) without using encapsulants, demonstrating another significant step forward in high-performance LEDs for solid-state lighting applications.

Methods

Device structure. The III-nitride epitaxial structure comprised an InGaN–GaN multi-quantum-well heterostructure grown on (0001) sapphire. It contained two InGaN quantum wells in which the In composition was tuned for an emitting peak wavelength of 450 nm. Silver was used as a p-contact and reflector. The sapphire substrate was removed by a laser lift-off process and the GaN layer was thinned to a thickness of 500–1,000 nm. Planar LEDs were left smooth, and patterning and dry etching were used to form the photonic-crystal layer in the n-GaN for the photonic crystal LEDs. Various lattice constants (200–1,000 nm), photonic crystal types (triangular, honeycomb, Archimedean A7 and A13) and depths (100–300 nm) were investigated, with a filling factor of ~0.3. The lattice constants started at the onset of diffraction to air and spanned several Bragg orders. The various lattice types were used to explore the issue of in-plane variation of the extraction and omnidirectional extraction[27]. The thickness of the film was chosen to ensure good overlap of the modes with the photonic crystal. The depth and filling factor of the photonic crystal were taken in a reasonable range as suggested in ref. 19.

A cross-section of the device is shown in Fig. 2a. Figure 2b shows a top view of a lit photonic-crystal LED with an injection current of 20 mA. Current crowding due to thin current spreading layers was not observed, and the LED was lit uniformly apart from variations related to the material, as seen on the cross-sections of the light emission profile (Fig. 2d). The n-contact was patterned into a grid, and the total LED area was ~200 × 200 μm^2. LEDs with various photonic crystals are shown bordering the lit die. Figure 2c shows a top-view atomic force microscope image of the photonic-crystal layer, demonstrating the high fidelity of the fabricated photonic-crystal structures.

Angular characterization and derivation of band structure. Radiation patterns were taken by measuring the spectrum with a fibre at various positions using a rotating arm above the device under test. Power measurements into $\pm 45^\circ$ were taken using a calibrated silicon detector located above the LED, which emitted directly into air at a fixed distance from the detector. Radiation patterns were used to calculate the total power emitted. The accuracy of the power measurement was verified by tests using well-calibrated reference LEDs.

The band structures of Fig. 4 were obtained as follows. By accurately modelling the emission pattern of the planar LED, using the method in ref. 28, we derived the thickness of the GaN layer and the intrinsic emission lineshape of the InGaN quantum wells, together with the theoretical extraction efficiency of the planar LED. The derived lineshape was then used to properly normalize the patterns shown in Fig. 3, removing the convolution by the lineshape. These measurements were then recast in terms of photonic band structure, as discussed in ref. 22. Angles were converted to wavevectors according to equation (4) (x-axis), and wavelengths to reduced frequencies a/λ (y-axis). We note that using the proper (experimentally derived) lineshape is important for a proper comparison to calculations.

Calculations. To model the optical properties of photonic-crystal LEDs, an S-matrix model with an embedded dipole source was used[24,25]. This method enabled a direct calculation of the emission pattern of a structure, and also yielded its extraction efficiency. The emission pattern was calculated assuming in-plane dipole emission for the InGaN quantum wells[29]. The convergence rate of the algorithm was enhanced by using the method in ref. 30, yielding a high calculation speed. The accuracy of the calculation was checked and agreed with finite-difference time-domain calculations on several test structures. The calculation of light extraction efficiency used realistic values for absorption in the active region and in the metal reflectors. To fit the visual aspect of the far-field pattern of Fig. 5, some damping was introduced to reproduce disorder in the structure. This was obtained by slightly increasing absorption losses to match the modes' width.

Received 17 November 2008; accepted 22 January 2009; published online 22 February 2009

References

1. Holonyak, Jr, N. Is the light emitting diode (LED) an ultimate lamp? *Am. J. Phys.* **68,** 864–866 (2000).
2. Gardner, N. F. *et al.* Blue-emitting InGaN–GaN double-heterostructure light-emitting diodes reaching maximum quantum efficiency above 200 A cm^{-2}. *Appl. Phys. Lett.* **91,** 243506 (2007).
3. Nakamura, S. Mukai, T. & Senoh, M. Candela-class high-brightness InGaN/AlGaN double-heterostructure blue-light-emitting diodes. *Appl. Phys. Lett.* **64,** 1687–1689 (1994).
4. Wierer, J. J. *et al.* High-power AlGaInN flip-chip light-emitting diodes. *Appl. Phys. Lett.* **78,** 3379–3381 (2001).
5. Haerle, V. *et al.* High brightness LEDs for general lighting applications using the new ThinGaN^{TM}-technology. *Phys. Stat. Sol* (a) **201,** 2736–2739 (2004).
6. Shchekin, O. B. *et al.* High performance thin-film flip-chip InGaN–GaN light-emitting diodes. *Appl. Phys. Lett.* **89,** 071109 (2006).
7. Krames, M. R. *et al.* Status and future of high-power light-emitting diodes for solid-state lighting, *J. Display Tech.* **3,** 160–175 (2007).
8. Yablonovitch, E. Inhibited spontaneous emission in solid-state physics and electronics. *Phys. Rev. Lett.* **58,** 2059–2062 (1987).
9. Fan, S., Villeneuve, P. R., Joannopoulos, J. D. & Schubert, E. F. High extraction efficiency of spontaneous emission from slabs of photonic crystals. *Phys. Rev. Lett.* **78,** 3294–3297 (1997).
10. Fujta, M., Takahashi, S., Tanaka, Y., Asano, T. & Noda, S. Simultaneous inhibition and redistribution of spontaneous light emission in photonic crystals. *Science* **308,** 1296–1298 (2005).
11. Purcell, E. M. Spontaneous emission probabilities at radio frequencies. *Phys. Rev.* **69,** 681 (1946).
12. Boroditsky, M. *et al.* Surface recombination measurements on III–V candidate materials for nanostructure light-emitting diodes. *J. Appl. Phys.* **87,** 3497–3504 (2000).
13. Choi, Y.-S. *et al.* GaN blue photonic crystal membrane nanocavities. *Appl. Phys. Lett.* **87,** 243101 (2005).
14. Rattier, M. *et al.* Omnidirectional and compact guided light extraction from Archimedean photonic lattices. *Appl. Phys. Lett.* **83,** 1283 (2003).
15. Oder, T. N., Kim, K. H., Lin, J. Y. & Jiang, H. X. III-nitride blue and ultraviolet photonic crystal light emitting diodes. *Appl. Phys. Lett.* **83,** 1231–1233 (2003).
16. Wierer, J. J. *et al.* InGaN/GaN quantum-well heterostructure light-emitting diodes employing photonic crystal structures. *Appl. Phys. Lett.* **84,** 3885–3887 (2004).
17. Orita, K. *et al.* High-extraction-efficiency blue light-emitting diode using extended-pitch photonic crystal. *Jpn J. Appl. Phys.* **43,** 5809–5813 (2004).
18. David, A. *et al.* Photonic crystal laser lift-off GaN light-emitting diodes. *Appl. Phys. Lett.* **88,** 133514 (2006).
19. David, A., Benisty, H. & Weisbuch, C. Optimization of light-diffracting photonic-crystals for high extraction efficiency LEDs. *J. Display Tech.* **3,** 133–148 (2007).
20. Benisty, H., De Neve, H. & Weisbuch, C. Impact of planar microcavity effects on light extraction—Part I: Basic concepts and analytical trends. *IEEE J. Quantum Electron.* **34,** 1612–1631 (1998).
21. Benisty, H., De Neve, H. & Weisbuch, C. Impact of planar microcavity effects on light extraction—Part II: selected exact simulations and role of photon recycling. *IEEE J. Quantum Electron.* **34,** 1632–1643 (1998).
22. David, A. *et al.* Photonic bands in two-dimensionally patterned multimode GaN waveguides for light extraction. *Appl. Phys. Lett.* **87,** 101107 (2004).
23. David, A. *et al.* Photonic-crystal GaN light-emitting diodes with tailored guided modes distribution. *Appl. Phys. Lett.* **88,** 061124 (2006).

24. Whittaker, D. M. & Culshaw, I. S. Scattering-matrix treatment of patterned multilayer photonic structures. *Phys. Rev. B* **60,** 2610–2618 (1999).
25. Delbeke, D., Bienstman, P., Bockstaele, R. & Baets, R. Rigorous electromagnetic analysis of dipole emission in periodically corrugated layers: the grating-assisted resonant-cavity light-emitting diode. *J. Opt. Soc. Am. A* **19,** 871–880 (2002).
26. David, A., Benisty, H. & Weisbuch, C. Spontaneous emission in GaN/InGaN photonic crystal nanopillars. *Opt. Express* **15,** 17991–18004 (2007).
27. David, A. *et al.* GaN light-emitting diodes with Archimedean lattice photonic crystals. *Appl. Phys. Lett.* **88,** 073510 (2006).
28. Ochoa, D. *et al.* Device simultaneous determination of the source and cavity parameters of a microcavity light-emitting diode. *J. Appl. Phys.* **85,** 2994–2996 (1999).
29. Schubert, M. F., Chhajed, S., Kim, J. K. & Schubert, E. F. Polarization of light emission by 460 nm GaInN/GaN light-emitting diodes grown on (0001) oriented sapphire substrates. *Appl. Phys. Lett.* **91,** 051117 (2007).
30. David, A., Benisty, H. & Weisbuch, C. Fast factorization rule and plane-wave expansion method for two-dimensional photonic crystals with arbitrary hole-shape. *Phys. Rev. B* **73,** 075107 (2006).

Acknowledgements

The authors would like to acknowledge support from several people, including M. Verschuuren of Philips Research, and T. Nguyen, K. Than and M. R. Krames of Philips Lumileds.

Additional information

Supplementary Information accompanies this paper at www.nature.com/naturephotonics. Reprints and permission information is available online at http://npg.nature.com/reprintsandpermissions/. Correspondence and requests for materials should be addressed to A.D.

Digital spatial light modulators

Spatial control of the phase and amplitude of a laser beam is useful for applications ranging from imaging and holography to interferometry and optical tweezers, reports **Neil Savage**.

Digital spatial light modulators (SLMs) provide fine-grained control of light, allowing the creation of two-dimensional light patterns with user-controllable characteristics. The devices, which have a myriad of uses in photonics, consist of an array of pixels, each of which can individually control the phase or amplitude of light passing through it or reflecting off it. In imaging, SLMs can be used to flatten out a wavefront, correcting for aberrations. They can also break a laser beam down into individually addressable spots, so that each spot is concentrated at a different point in a three-dimensional space. In telecommunications they can encode signals, increasing a light beam's data bandwidth. They can even create images of scenes in infrared light, allowing defence contractors to test the infrared targeting systems on their missiles.

"Some of the applications are fascinating," says Ross Nakatsuji, sales group leader at Cambridge Research and Instrumentation, a leading supplier of SLMs based in the United States. He sees increasing use of SLMs in biomedical applications, whether it's allowing more precise cutting in laser surgery, or using optical tweezers to separate cells in a Petri dish. Researchers wishing to sort cells can place an array of focused spots (generated by an SLM) on a single cell and use them as grappling hooks to move the cell around. The same ability is useful for people carrying out nano-assembly, moving beads or carbon nanotubes into place.

Like so many other photonics components, SLMs have evolved from complex set-ups that required an expert to use them to plug-and-play items that all sorts of researchers can use.

Steve Serati, CEO of Boulder Nonlinear Systems, says that he sees increasing use of SLMs for optical pulse shaping. People with wideband sources are using SLMs to modulate laser pulses to give them the characteristics they need for a particular application. For instance, coherent anti-Stokes Raman spectroscopy is used for the study of cells. It requires three laser beams — a pump beam, a probe beam and a Stokes beam — all of which must be aligned so that they interact correctly. "By using pulse shaping you can create the type of modulation you need with a single pulse [from a single laser]," Serati says. Pulse shaping can also be used to generate point-source X-rays for high-resolution X-ray imaging. Serati says that efforts are now focused on increasing the spectral range of operation of SLMs, particularly in the infrared. Manufacturers are also always working on ways to improve efficiency, modulation depth and phase stability. "It's a pretty interesting technology, with a lot of versatility," he says.

MEADOWLARK OPTICS

As for future development, Nakatsuji says that there is demand for SLMs with higher pixel counts and smaller devices that can be easily integrated with other equipment.

PRODUCT ROUND-UP

The ShapeShifter Linear Array spatial light modulator from **Meadowlark Optics** (Frederick, Colorado, USA) has a linear pixel array geometry and offers computer control of the temporal profile of femtosecond light pulses, for applications such as Hadamard spectroscopy, optical data storage and wavefront compensation. It comes in a phase version that provides at least one-wave optical path difference, and an amplitude version that provides at least half-wave. Both have 98-μm-wide pixels. The company's Hex SLM is a two-dimensional device designed for adaptive optics applications, such as high-resolution imaging through a medium that induces optical aberrations. It has an array of variable retarders acting as a real-time, programmable phase mask for wavefront correction of a linear polarized source. It removes aberration by introducing the opposite phase shift. The Hex also comes in both an amplitude and a phase version, with 1,000-μm-wide pixels. Versions are available to handle wavelengths centred from 450 to 1,800 nm. The devices use nematic liquid crystal retarders on an optical-quality synthetic fused silica substrate. They have full frame update rates from 10 ms to 50 days. Variation in retardance is <2% root-mean-squared over a clear aperture. Distortion of the transmitted wavefront is $<\lambda/4$ at 632.8 nm and beam deviation is <2 arcmin. Transmittance without polarizers is >90% and reflectance is <0.5% per surface at normal incidence. Operating temperature range is from 10 °C to 45 °C. The optical head measures 179 mm × 75 mm × 19 mm and control is by Windows operating systems through a USB port.
www.meadowlark.com

The X10468 series liquid-crystal-on-silicon SLM from **Hamamatsu Photonics** (Hamamatsu City, Japan) is a reflective type of pure phase SLM. It is designed for highly efficient use of light, whether measured in terms of reflectivity, aperture ratio or diffraction noise. The standard digital video interface of a PC controls the SLM, and the controller can efficiently compensate for distortions in the chip, such as wavefront distortion and nonlinear response of the liquid crystals. Applications include wavefront correction, pulse shaping, beam forming and steering, laser processing, optical manipulation and optical testing. The liquid crystals change only the phase of the light, without any change in intensity. The X10468 series comes in seven standard types. The -01, -07 and -08 models have no dielectric mirror but have higher diffraction efficiency, but low light utilization efficiency (~72%) and cover a wide wavelength range.

HAMAMATSU PHOTONICS

In contrast, models -02, -03, -04 and -05 have a dielectric mirror for a specified wavelength range, and a light utilization efficiency of about 90%. Reflection loss causes interference noise between 700 and 900 nm in model -07 and between 1,150 and 1,400 nm in model -08. Ultraviolet light causes damage at wavelengths below 400 nm in the -05 model. Between the various models, spectral coverage is available from 355 to 1,550 nm with phase modulation of >2π radians. Diffraction loss is <5%. The SLMs have SVGA resolution of 800 × 600 pixels. They offer a frame rate of 60 Hz, with 256 eight-bit input levels. The effective area measures 16 × 12 mm, with a fill-factor of 95%. Maximum spatial resolution is 25 line pairs per millimetre. Typical rise time ranges from 10 to 30 ms, depending on model and wavelength, with fall times from 30 to 140 ms. Input voltage is from 100 to 230 V.
www.hamamatsu.com

The Model 12,288 linear series spatial light modulator from **Boulder Nonlinear Systems** (Lafayette, Colorado, USA) operates in reflection and is based on liquid-crystal-on-silicon (LCOS) technology. It provides high-speed phase or amplitude modulation without the need for any mechanical motion. The linear array

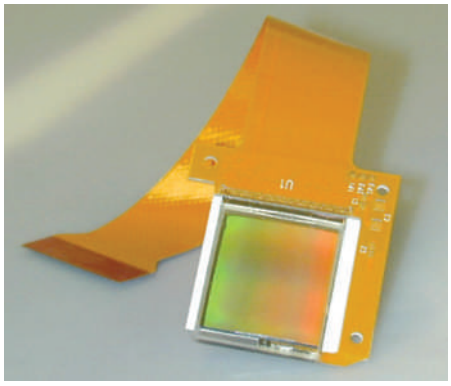

BOULDER NONLINEAR SYSTEMS

features 12,288 columns each containing one pixel, with a pixel pitch of 1.6 μm and a gap between pixels of 0.6 μm. Each SLM system includes an SLM optical head with two-axis graduated control and adjustment, with total travel of ±3°; digital-to-analogue converter drive electronics and all necessary cabling; a memory board that mates with a computer's standard PCI slot; a user manual; and a CD containing application-specific software. The pixel array measures 19.66 mm × 19.66 mm, and the device can handle wavelengths from 635 to 1,550 nm. Zero-order diffraction efficiency is rated as 80–95%. The system has an external window with a broadband antireflection coating providing an average reflection of < 1% from 450 to 865 nm or 850 to 1,650 nm. Custom antireflection coatings are also available, including a V-type for optimum optical efficiency at a single laser wavelength. The SLM has a fill factor of 100% and modulates by controlling the index of refraction in the liquid crystals. The steering angle is ±4° to ±7°. Double-pass phase stroke is typically 2π at a user-specified laser line, and a minimum of 50–100 linear phase levels are resolvable. Distortion of the reflected wavefront is 0.1λ to λ (root-mean-squared) at nominal wavelength. Response time is 5–30 ms and switching frequency is 30–200 Hz, although both are dependent on phase stroke, temperature and wavelength.
www.bnonlinear.com

The DLP Discovery 4000 kit from **Texas Instruments** (Dallas, Texas, USA) offers high-resolution two-dimensional spatial light modulators based on digital micromirror arrays that are at the heart of digital laser projection technology. Although liquid-crystal-based devices offer unprecedented control of amplitude and phase, they are typically limited to refresh rates of the order of 100 Hz. In contrast, micromirror devices are capable of at least 100 times faster switching. Another key feature is the broadband operation from the ultraviolet through to the infrared.

Five micromirror array options are offered with dimensions ranging from 0.55 inches up to 0.95 inches and resolutions up to 1,920 × 1,080 pixels, that is, with around two million mirrors per array and a mirror pitch of 10.8 μm. Each mirror can be individually deflected up to ±12° about a hinged diagonal axis. High-speed operation of all of the micromirrors is made possible by a wide-bandwidth interface capable of up to 51.2 gigabits per second data transfer. The 0.55-inch 1,024 × 768 array is capable of 32,550 patterns per second, and the 0.95-inch 1,920 × 1,080 array can produce 24,690 patterns per second.

The kits includes a digital controller board with a USB 2.0 interface, the Xilinx Virtex 5 field programmable gate array, an Avnet EXP bus expander and a 200-pin SODIMM DRAM expansion port. Flex cable connections to remote digital micromirror boards are said to allow for easy optical and mechanical mounting. Interface and logic supply voltages are 3.3 V, and operating case temperatures from 25° to 45° are recommended.
www.ti.com

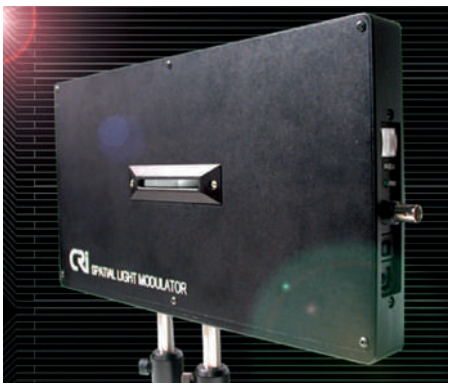

CAMBRIDGE RESEARCH AND INSTRUMENTATION

The SLM-128 and SLM-640 spatial light modulators from **Cambridge Research and Instrumentation** (Woburn, Massachusetts, USA) are based on bonded optical masks that can provide simultaneous phase and amplitude control in a single device. The liquid crystal linear-array devices come in both single- and dual-mask configurations. Depending on the orientation of the extraordinary axis of the liquid crystal and the placement of the linear polarizers, in front of or behind the crystal (or both), a single-mask SLM can modulate either a beam's phase or its amplitude. In dual-mask models, a pair of liquid crystal masks are bonded together, with an orientation orthogonal to one another and at 45° to the polarization of incident light, which allows the independent adjustment of both phase and amplitude. Removing the polarizers and driving both masks with the same pattern allows the

SLM to be used as a pure phase modulator for arbitrarily polarized light. An optional surface-coated mirror allows the beam to pass through the system twice, doubling the optical modulation and allowing faster response when changing drive patterns. The SLMs come with either 128 or 640 pixels per mask, with a height of 5,000 μm, a pitch of 100 ± 0.005 μm, and a gap between pixels of 2 μm. They are optimized for either the 488–900-nm range or the 900–1,620-nm range. For the shorter wavelengths, they provide >88% transmission with one mask and >85% with two. In the longer wavelengths, they provide >92% transmission with one mask and >90% with two. The pulse damage threshold of the device is 100 μJ cm^{-2} at 490 nm for 50-fs pulses at a repetition rate of 1 kHz. For similar pulses at 890 nm, the damage threshold is 200 μJ cm^{-2}. Maximum modulation is 3π radians on a single pass at the longest wavelength in the operating range, and greater at shorter wavelengths. Modulation is doubled when the SLM is used in reflection. The device is controlled by means of a USB interface or a 5 V/3.3 V logic trigger.
www.cri-inc.com


HOLOEYE

The PLUTO phase-only spatial light modulator kit from **HOLOEYE Photonics AG** (Berlin, Germany) is based on a reflective liquid-crystal-on-silicon microdisplay with an HDTV resolution of 1,920 × 1,080 pixels. The device's electrically controlled birefringence display mode causes the phase panels to provide a pure phase shift of up to 2π for wavelengths up to 1,550 nm. The SLM is aimed at phase-shifting applications including wavefront correction, optical tweezers, optical metrology, interferometry, lithography and holography. The platform controls the active matrix, reflective mode, phase-only liquid crystal displays, which are optimized for three wavelength ranges: 420–850 nm, 850–1,100 nm, and common telecommunication ranges up to 1,550 nm. A standard digital visual interface signal from a PC's graphics card addresses the signal. The company says that the plug-and-play system guarantees quick start-up and easy use. Windows-based software allows users to configure the modulator for different applications and wavelengths by means of an RS-232 interface. The device provides 256 eight-bit grey levels and has an active area of 15.36 mm × 8.64 mm with a fill-factor of 87%. Maximum image frame rate is 60 Hz and maximum illumination is <2 W cm^{-2}. Zero-order intensity is 60%. Operating temperature range is 10–70 °C. An absorption filter controls ultraviolet irradiation.
www.holoeye.com

NEIL SAVAGE is a freelance science and technology journalist based in Lowell, Massachusetts, USA.

A clever twist

It has now been shown that twisting the orientation of layers in a metamaterial provides a new way of tailoring their electromagnetic properties. *Nature Photonics* spoke to Harald Giessen and Na Liu from the University of Stuttgart about the idea.

What is a metamaterial and why are they interesting?

A metamaterial is an artificially engineered material made from an array of unit cells that are carefully designed to produce a desirable electromagnetic response. A common design of unit cell is the so-called split ring resonator (SRR), a tiny metal ring-shaped structure featuring a miniature gap. Changing the size, geometry and composition of the resonator determines the electromagnetic properties of the metamaterial and its wavelength of operation. Such metamaterials are being investigated for a wide variety of applications ranging from the development of materials with a negative refractive index to those that can perform cloaking or act as a perfect lens.

How did you get the idea of making twisted metamaterials?

Initially, we were studying a four-layer stacked SRR structure. We found that at normal incidence, the electric coupling between neighbouring layers dominates and determines the optical properties of the structure. Later, we came up with a design called "metaDNA", which consists of multiple layers of 90° twisted SRRs. In this case, the magnetic coupling has a key role. This made us wonder about the roles of electric and magnetic interactions in stacked SRRs with different geometries. In order to solve this riddle, we simplified the problem to stacked SRR dimers with twist angles of 0°, 90° and 180°. Subsequently, we were able to understand the electric and magnetic coupling in these three structures by utilizing the method of plasmon hybridization from Peter Nordlander, a well-known chemist at Rice University, USA. One day, Stefan Linden, an expert in metamaterials from Karlsruhe, visited our lab, looked at our structures and suggested, "Why not take a further step and twist the structures from 0° to 180°?". We followed his suggestion and began new studies. In the end, we could not only logically understand but also analytically describe the evolution of electric and magnetic interactions with

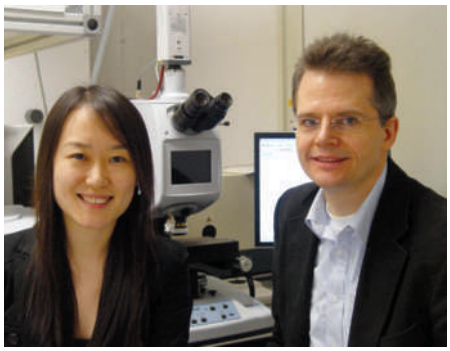

HARALD GIESSEN

Na Liu and Harald Giessen from the University of Stuttgart in their laboratory.

twist angle, using the Lagrangian model of our collaborator Hui Liu [one of the co-authors of the paper on page 157 of this issue] from Nanjing University.

Why did you decide to call your structures "stereometamaterials"?

The exact word "stereometamaterials" was generated during a discussion over the phone between Na Liu and Hui Liu. In fact, we are both admirers of Peter Nordlander and his insight into plasmonics using the hybridization method from chemistry. We suspected that as the resonant behaviour of stacked SRRs with specific angles of orientation can be understood by plasmon hybridization, there might already be some established system or model in chemistry that was analogous to our twisted metamaterial system. Finally, we found the term stereochemistry, which is a subfield of chemistry, which studies how the spatial arrangement of atoms within molecules determines the properties of chemical substances. As a result, we decided to call our structures "stereometamaterials".

What kind of applications could such stereometamaterials have?

One of the most obvious applications of stereometamaterials is optical polarization control. Because the polarization properties of adjacent metamaterial layers can be different, by introducing appropriate phase shifts between these layers, the polarization of the transmitted wave is highly tunable. It would also be very interesting to study the chiral effects of twisted structures, especially left- and right-twisted ones, namely enantiomers. As predicted by Sir John Pendry, the strong chirality can allow the realization of a negative refractive index without requiring simultaneous negative permittivity and negative permeability. Negative refraction may result from the cross-coupling of the electric and magnetic response. With proper design of stereometamaterials, the electric and magnetic dipoles can have parallel components, giving rise to negative refraction for circularly polarized light. You could also imagine having polarization rotation devices made from a material that is a few hundred nanometres thick — two or three layers that are custom-designed to have great efficiency. Sensing is also a possibility as these structures can show electromagnetically induced transparency and thus very narrow resonances which can be used for sensing or generating slow light.

What are your plans for future work in this area?

Future research will include studies on how to make use of higher-order electric multipolar and magnetic interactions, which can be nearly as large in these systems as the electric dipolar interaction. Also, the influence of the structural geometry on the material's optical properties, and the distance dependence of stereometamaterial coupling, are intriguing. More analogies between artificial metamaterial molecules and real molecules in chemistry might be discovered in the future. Additionally, these metamaterial molecules, which can be realized according to a designer's plan, may be able to emulate liquid crystals, chiral proteins and drug enzymes, leading to useful applications in biophotonics.

INTERVIEW BY OLIVER GRAYDON

Giessen and co-workers have a paper on the topic of stereometamaterials on page 157 of this issue.